Development of a Fibre Optic Sensor for Methane Gas

by

Jude Sweeney

A thesis presented to

Dublin City University

For the Degree of M.Sc

February 1994

Supervised by

Dr. Brian MacCraith

School of Physical Sciences

Dublin City University

Ireland

I hereby certify that this material, which I now submit for assessment on the programme of study leading to the award of M.Sc is entirely my own work and has not been taken from the work of others save and to the extent that such work has been cited and acknowledged within the text of my work.

Signed: 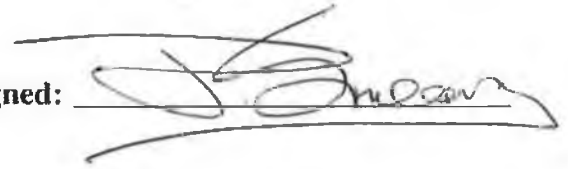 **Date:** 20-FEB-1994.

DEDICATION

I dedicate this work to my family and friends.

ACKNOWLEDGEMENTS

I have spent over six years in the Physics Department of DCU and I have enjoyed, well... almost every minute of it. A big thanks to the departments staff for all their help over these years.

To Brian Mac Craith I say a big thank you. Even though I know you are a busy man, you still had time for my work and I appreciate that.

Thank you, all my friends, for your support, encouragement and laughter. You all mean a lot to me.

Thank you, my family, for everything.

TABLE OF CONTENTS

ABSTRACT

A fibre optic sensor for methane gas using the "differential absorption" referencing technique has been designed and constructed. Infra red light in the 1.66μm spectral region is absorbed by methane and this is the operating principle of the sensor. The system employs a novel LED, manufactured by GEC Marconi Ltd., as an infra red light source. The LED couples more power into single mode fibre than any other device of its type which is commercially available. The light is transmitted to a gas cell via single mode fibres and a fibre optic coupler, where some of it is absorbed according to the concentration of methane present. Two optical interference filters with transmissions at absorbing and non-absorbing spectral regions, respectively, are used in dual wavelength referencing mode to remove any interferences from non gas dependent parameters (e.g. dust in the cell). A calibration curve for the sensor is determined by plotting the values of the attenuated light signals against the corresponding concentrations of methane in the gas cell.

A full characterisation of each component of the system was undertaken and the systems overall performance determined. The system has a limit of detection of 0.077% CH_4. This is a factor of 18 below the specification requirement for the project, which is 1.25% CH_4 in air (i.e. 25% of the Lower Explosive Limit). The system has a resolution of 0.025% CH_4 and shows both good repeatability and reproducibility. The main problem associated with the system is the critical temperature dependence of the optical interference filters, whose transmissions vary with temperature changes of 0.1°C and therefore affect the system stability.

Chapter 1

Introduction

1.1 Optical Fibre Sensors

Fibre optic technology is now firmly established as the basis of long distance, high data transmission telecommunication systems. Over the past twenty years, in parallel with the development of this technology, considerable research into optical fibres as sensing devices has been carried out. Optical fibre sensors for both physical and chemical parameters have already been demonstrated and research activity in this area continues to develop. Although much of this research is still in its early stages of development, it is expected that at least some of these sensors will become commercially viable in the near future.

An optical fibre sensor may be defined as a device in which a guided optical signal is modulated in response to a measurand, such that the required measurand information may be recovered from the modulated signal. This may mean modulation in the intensity, phase, frequency, colour, polarisation or any combination of these parameters, of the guided light.

Optical fibre sensors are classified as *intrinsic* or *extrinsic*. In intrinsic sensors, the optical fibre is itself the sensing element. The fibre is often modified in some form to enhance the interaction with the measurand. An example of this is the use of a magnetostrictive coating on the fibre to sense magnetic fields. Extrinsic sensors differ in that the optical fibre is used purely as a medium to transport both the unmodulated and the modulated light to and from the sensing area. The modulation of the light parameter(s) by the measurand occurs externally to, and is independent of the fibre. An example of this is the use of a deformable mirror for pressure sensing. The amount of light reflected from the mirror back into an adjacent optical fibre coupler varies according to the pressure on the mirror.

1.2 Fibre Optic Chemical Sensors

The detection of chemical parameters in industrial processes and in environmental control is of greater importance as stricter laws are being placed on safety and pollution monitoring. In recent years fibre optic sensors have been developed not only in these areas but also for biomedical purposes. Sensors for parameters

including pH [1,2], gases [3,4], antibodies [5] and metallic ions [6] have been developed successfully.

Optical fibre based chemical sensors offer many advantages over the conventional sensing techniques of potentiometric and amperometric electro-chemical devices. They are intrinsically safe because they are thermally cold and electrically passive. No power source is needed at the sensing head. They are immune to electromagnetic interference, are chemically inert and do not suffer from "poisoning" (i.e. the irreversible degradation of other sensors such as catalytic type sensors).

Intrinsic and extrinsic optical fibre chemical sensing techniques fall into two categories, namely *direct spectroscopic* and *reagent-mediated* sensing. In direct spectroscopic sensing, the fibre optic light signal interacts directly with the analyte if the interrogating wavelength coincides with an absorption band of the analyte. In reagent-mediated sensing an intermediate reagent, which responds optically (e.g. by absorption or fluorescence change) to the analyte, is attached to the optical fibre. Determination of the analyte concentration is based on absorption, fluorescence or Raman spectroscopic methods in both categories.

As already described, modulation of the light in extrinsic chemical sensors is independent of the fibre. Most intrinsic chemical sensors rely on the "evanescent wave" (EW) technique. In this case, the cladding is removed from part of the fibre thereby exposing the evanescent field either directly to the analyte or to an intermediate reagent depending on the sensing technique used. The analyte concentration is then determined according to the degree of absorption or fluorescence that subsequently occurs.

1.3 Extrinsic Fibre Optic Sensing of Methane Gas

Fibre optic sensing techniques are particularly suited to the detection of gases and over the last twenty years research in this field has surged. Experimental gas sensors employing the various sensing techniques outlined in the previous section have already been successfully developed [3,4,7,8,9].

One of the most important areas of research in this field has been the development of fibre optic methane gas sensors. The motivation for this has been the obvious need for sensors that can remotely detect methane safely and accurately,

especially in hazardous or explosive environments such as coal mines and landfill sites. Methane (CH_4) is a highly flammable gas if its concentration is between 5% and 15% by volume in air. These two percentage limits are defined as the Lower Explosion Limit (LEL) and the Upper Explosion Limit (UEL), respectively. Above the UEL, there is not enough oxygen to support combustion. Industrial standards require sensors to be capable of sensing 25% LEL (i.e. 1.25% CH_4 in air) accurately [10].

Fibre optic methane sensing has all the advantages of fibre optic sensors as outlined in the previous section with the added possibility of system multiplexing (i.e. remote detection at many different points at the same time using a single control unit). Only direct spectroscopic methane sensors, both evanescent wave and extrinsic absorption based, have been developed thus far. Although the research into the evanescent wave based sensors is increasing [7,11], the greatest success has been achieved with extrinsic absorption techniques. Research activity in this field has been reported since 1983, when Chan *et al.* first described a system with a limit of detection of 2000ppm, based on absorption at the $\nu_2+2\nu_3$ combination band of methane at a wavelength of 1.33μm, over a 2km fibre length [3]. Subsequent work at this wavelength was reported by the same authors in 1987 when the system was used to remotely sense methane in city gas. An improved limit of detection of 1300ppm was reported over 2km [12,13]. Other groups have also developed systems at this wavelength [14,15].

In 1983, Hordvik *et al.* first reported a remote fibre optic methane sensing system operating at the $2\nu_3$ overtone of methane at 1.66μm. The limit of detection of this system measured over a 600m length of optical fibre was less than 5000ppm of methane in nitrogen [16]. Working at this wavelength is attractive as the $2\nu_3$ overtone absorption is approximately twice as strong as the $\nu_2+2\nu_3$ combination band at 1.33μm and is also transmitted well by silica fibre. Other research groups, including Chan *et al.* [17], Stueflotten *et al.* [18], Zientkiewicz [19] and most recently Dubaniewicz *et al.* [20], have demonstrated similar systems operating at 1.66μm. Dubaniewicz *et al.* report a limit of detection of 2000ppm over a 2km length of fibre.

All of the systems discussed thus far employ a "differential absorption" referencing technique for sensing methane, whereby the signals corresponding to an

absorbing and a non-absorbing (or reference) wavelength are measured alternately and ratioed. Because effects which are not dependent on the gas concentration (e.g. dust in the gas cell or source power fluctuation) are virtually independent of wavelength, taking a ratio of the two signals eliminates errors that may arise in concentration determination. The systems use interference filters or a monochromator to select the appropriate absorption and reference wavelengths. Other research work using very different techniques has also been successful. Plessey Research, Caswell, U.K. have developed a scanning comb filter (essentially a Fabry-Perot etalon), the spacing of which is matched to the set of rotational absorption lines in the R branch of the $2\nu_3$ overtone of methane. This system is highly gas selective and can sense 2600ppm of methane in air [21]. Dakin and Edwards at the University of Southampton, U.K., have also developed a highly selective fibre optic methane sensor, based on infra red absorption at the $2\nu_3$ overtone at 1.66μm [22]. The sensor incorporates correlation spectroscopy using the "pressure modulation" technique (first described by Goody [23]) to selectively sense methane. Experimental results using ethane as the likely contaminant gas with the most similar absorption to methane, have shown excellent selectivity. A limit of detection of 50ppm methane has been reported with this system .

Although some systems have been tested successfully in field situations (e.g. city gas in Sendai, Japan [12,13]; the TCP2 oil-platform in the Frigg oil-field, North Sea [18]; Teralba coal colliery, Australia [24]), development of commercial devices has been slow. The principal reason for this is that laboratory based systems have not yet achieved the cost and performance criteria required for underground methanometers. Although current pellistor technology works adequately, its principal shortcoming is performance degradation. Consequently, pellistor based systems require constant maintenance (e.g. recalibration), making this technology relatively costly. However, industry will only change over to fibre optic based sensors, if greater performance can be achieved over pellistors at a lower cost and most importantly with longer maintenance intervals. A comprehensive study of commercial and prototype optical methane sensors was undertaken under laboratory conditions by Willett, British Coal Corporation, U.K. in 1990 [25]. Willett recently reports that none of the systems investigated in the survey met the cost and performance criteria

laid down for underground methanometers and, in many cases, this reflected the fact that they had been designed as alarms to detect significant rapid increases in methane concentrations rather than as long term quantitive measuring devices. The report concluded that although there have been advances since 1990 in the development of fibre optic methane sensors, fully operational, cost effective and high performance sensors for mining have not yet been realised. The commercial systems that are presently available are fibre optic absorption spectrometers (e.g. Oriel Scientific, U.S.A.; Guided Wave International, Sweden; Photonics Society, France) [26,27].

1.4 Project Objectives

All the extrinsic methane sensing systems described in the preceding paragraphs can detect 25% LEL, which is the basic industrial requirement. However, most of these systems use bulk optics to some extent, particularly when focusing source light into fibre, when collimating the gas cell beam and, in some cases, when collimating light signals transmitted through interference filters. As a result, these systems are not rugged enough for field operation. Secondly, all of the systems discussed employ multimode silica fibre which is susceptible to "modal noise" problems (see section 4.2.1).

A well engineered demonstrator sensing system addressing both the cost and performance criteria required by industry, as outlined in section 1.3, was designed, constructed and characterised. For the work reported here, the system is ruggedised for harsh sensing environments, avoiding bulk optics almost totally. This is achieved using optical fibre fusion splicing technology together with mechanical fibre connectors and fiberised GRIN lenses for beam collimation purposes. The system is designed such that a single fibre is used at the sensing head to both transmit and collect unmodulated and modulated light, respectively. This eliminates the added difficulties associated with having a second fibre at the sensing head, as well as minimising costs. Methane can be sensed at the 3.4μm fundamental absorption band (where the strongest absorption occurs) using zirconium based fluoride fibres. However, these fibres have a high transmission loss and are susceptible to water contamination. Consequently, the system described in this work employs relatively low cost, standard telecommunication, single mode, silica optical fibre. This fibre

transmits light at 1.66μm (i.e. the $2\nu_3$ absorption overtone) with a low transmission loss of approximately 0.2 dB/km. Modal noise problems do not occur with single mode fibres. Other standard telecommunication components are also utilised in this system such as a fibre optic coupler and an InGaAs detector. The use of the fibre optic coupler introduces the possibility of developing multiplexing techniques for simultaneous multi-point sensing. The system also capitalises on a novel, high powered LED source designed specifically for methane sensing at 1.66μm. Although the cost of this device was appreciable, similar, potentially cheaper devices are currently under development in the National Microelectronics Research Centre, Cork.

The design, construction and performance evaluation of the dedicated system is reported here. Chapter 2 gives an overview of the spectroscopy of hydrocarbons with particular emphasis placed on methane. The experimental system and its development is described in chapters 3 and 4, respectively. Chapter 5 details the results obtained with the system and evaluates the system performance. Finally, chapter 6 discusses possible future work to further develop the system.

Chapter 2

Structure & Spectroscopy of Hydrocarbon Molecules

2.1 Introduction

This chapter outlines the structure and spectroscopy of hydrocarbon molecules. In particular, methane is treated in some detail as this is the gas under investigation. The chapter first treats the classification of molecular energy levels and then outlines the fundamentals of molecular symmetry, modes of vibration and transition intensities. It ends with a section on rotational features of vibration spectra.

Spectral transitions are defined either by wavelength (nm), or wavenumbers (cm^{-1}). The latter is equal to the reciprocal of the wavelength.

Methane (CH_4) is a highly symmetric, non linear, tetrahedral shaped, polyatomic molecule. It consists of a centre atom of carbon bonded to four atoms of hydrogen. The angle between any two bonds is 109.6° and the bond length between the carbon atom and each of the hydrogen atoms is 1.094Å [28] as shown in Fig 2.1.

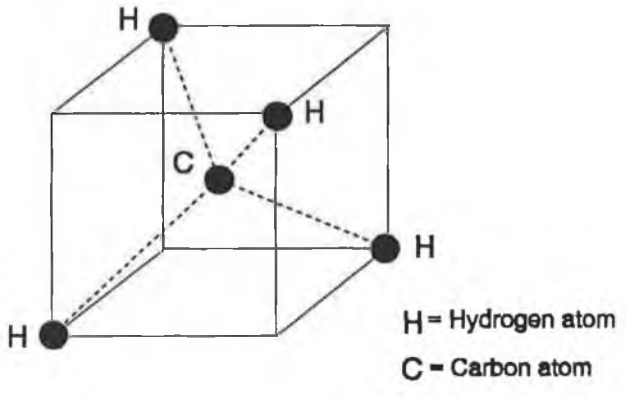

Fig 2.1 Methane Molecule

2.2 Molecular Energy Levels

The energy of any molecule is quantised. Only certain discrete energy levels are allowed. This energy is not governed wholly by its electronic configuration, as is the case with singular atoms. Nuclear motion of the molecule gives rise to two

other forms of energy levels. These are *vibrational* energy levels and *rotational* energy levels. A molecule does not have a constant bond length but undergoes regular vibration. The vibrational energy is quantised so that only discrete frequencies are allowed. These frequencies depend on the masses of the atoms of the molecule and the bond strengths. Secondly, the molecule also rotates. The rotational energies are also quantised.

Therefore,

$$E_{TOTAL} = E_{ELECTRONIC} + E_{VIBRATIONAL} + E_{ROTATIONAL}$$

where E is energy [29].

The energy associated with each transition type varies greatly. Electronic transitions (i.e. between two electronic energy levels) are of the order of a few eV, vibrational level transitions are approximately 0.1eV and rotational levels are approximately 0.001eV [28] as shown in Fig 2.2.

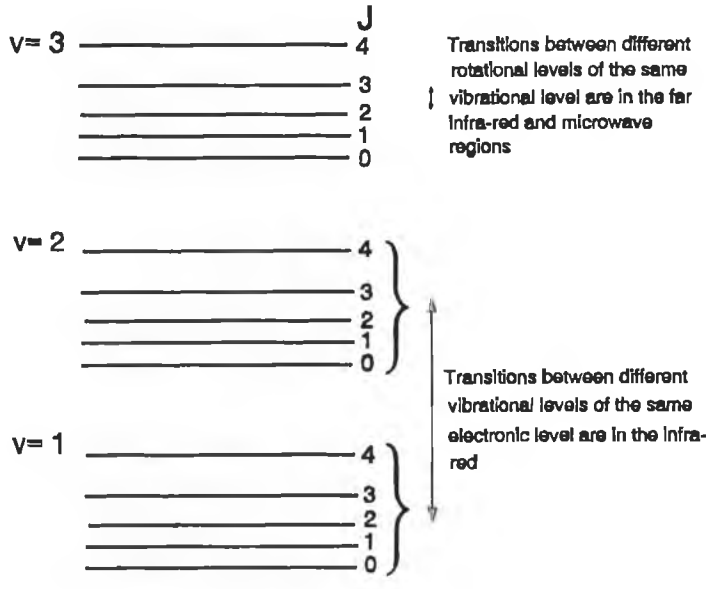

Fig 2.2 Transition Levels

These energies associated with electronic, vibrational and rotational transitions correspond to the visible/ultra-violet, the infra-red and the far infra-red/micro-wave

regions of the electromagnetic spectrum, respectively. Therefore, for visible light absorption there will be electronic energy transitions with associated vibrational and rotational energy transitions. If infra-red radiation is absorbed then there will not be sufficient energy absorbed for electronic transitions and only vibrational and rotational transitions will occur [29].

2.3 Molecular Symmetry

The different forms of symmetry found in molecules are called *symmetry elements*. Molecules with the same degrees of symmetry are classed under a group in the thirty two *crystallographic point groups*. This is a molecular symmetry classification table. This arises from the fact that there are only thirty two possible ways of combining symmetry elements. There are two notations used describing each of these crystallographic groups. One is the Herman-Manguin and the other is the Schöenflies.

The methane molecule possesses many symmetry elements but it is not a linear polyatomic molecule. Methane has six mirror planes (i.e. one half of the molecule is the mirror image of the other). It also has three fourfold inversion axes (this involves the rotation of each atom through ninety degrees and then inversion through the centre of the molecule). Finally it also has four threefold inversion axes. Its crystallographic point group is T_d in Schöenflies notation and 43 in Herman-Manguin notation [29].

2.4 Modes of Vibration

Molecules vibrate upon collision with other like molecules. The number of ways that each molecule can vibrate is referred to as the number of *modes of vibration*. In any one "normal" or "fundamental" mode all the nuclei vibrate in phase with the same frequency. Each of the N atoms in a non-linear polyatomic molecule has three degrees of freedom corresponding to motion along the three Cartesian co-ordinates. The whole molecule has therefore 3N degrees of freedom. However, three of these correspond to translation of the molecule along the three axes. Three others correspond to an overall rotation of the molecule about the three axes. This leaves 3N-6 normal modes of vibration [29].

Methane has five atoms and therefore should have nine normal modes of vibration. However, due to the high symmetry of the molecule some modes have the same energy resulting in only four discrete "normal" or "fundamental" vibrational modes. These are [30],

ν_1 - A symmetric C-H stretch at 3657cm^{-1} or wavelength 2.734μm

ν_2 - A doubly degenerate stretch at 1533cm^{-1} or 6.523μm

ν_3 - A triply degenerate asymmetric C-H stretch at 3019cm^{-1} or 3.312μm

ν_4 - A triply degenerate asymmetric H-C-H bend with at 1311cm^{-1} or 7.628μm

2.4.1 Vibrational Energy Level Transitions

Each fundamental mode of vibration in a molecule has associated vibration levels of increasing energy in which transitions may also occur.

Fig 2.3 is a potential energy curve of a diatomic molecule which has only one fundamental mode of vibration. This curve and the following analysis give a good representation of vibrational energy level systems for polyatomic molecules. Methane has not just one *stretching* mode as depicted in this curve but has three different *stretching* modes and a *bending* mode also [28]. The potential curve of each of these four fundamental modes is very different.

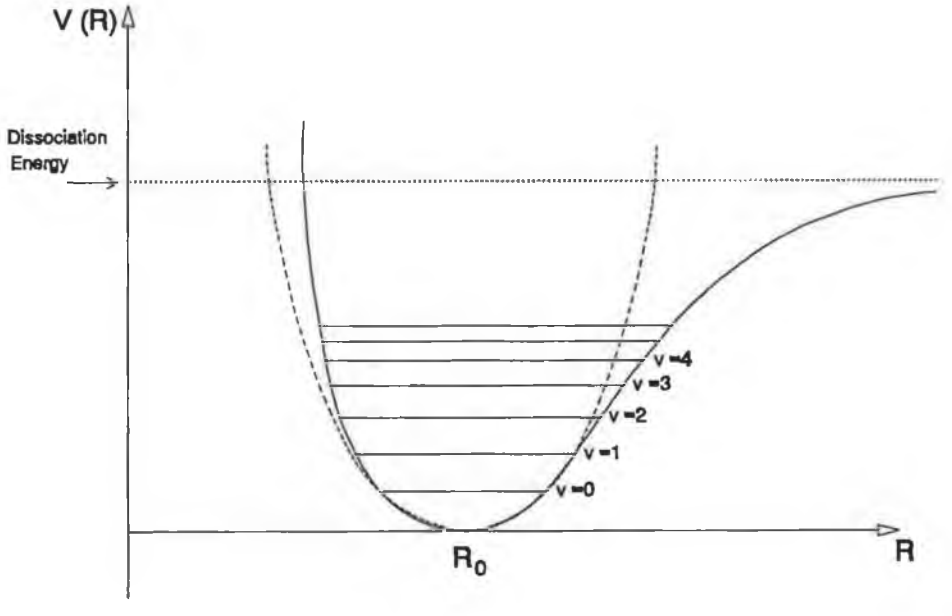

Fig 2.3 Diatomic Molecule Potential Energy Curve

The *stretching* mode depicted in Fig 2.3 for the linear diatomic molecule shows one atom vibrating about the equilibrium distance R_e while the other remains stationary at R=0. The quantised vibrational energy levels associated with this particular fundamental frequency of vibration are given as v=0,1,2,3.. . Therefore, if a photon of infra-red radiation equal in energy to the energy difference between any two levels interacts with the molecule, it will be absorbed [29]. This results in a vibrational energy level transition. If one such transition to a higher energy level occurs due to absorption then it can be seen from the curve that the vibrating atom vibrates over longer distances around R_e.

At low vibrational energy levels, v=1,2,3,4 the vibration of the diatomic molecule is harmonic and is described by Hooke's Law. In this case the restoring force F is proportional to the displacement x as,

$\mathbf{F = -kx}$ where k is the force constant.

Equivalently, on the potential energy curve in Fig 2.3,

$\mathbf{V(R) = \frac{1}{2} k R^2}$ where V(R) = Potential energy at position R

The lower part of the curve is parabolic in shape as indicated by the dashed curve in Fig 2.3. The energy associated with each vibrational energy level E_v is,

$$E_v = (v+\frac{1}{2})h\nu_0 \qquad Eqn\ 2.1$$

where v=0,1,2..etc, h = Planck's constant and ν_0 = Fundamental vibration frequency. When at v=0 (i.e. when no quantum of vibrational energy is present), the molecule still vibrates at its fundamental mode of vibration with $E=\frac{1}{2}h\nu_0$.

The selection rule governing transitions between the lower energy levels in the curve (v=0,1,2) is,

$$\Delta v = \pm 1$$

This rule applies only for a molecule undergoing strictly harmonic oscillation.

However, at higher vibration energy levels (i.e. towards the dissociation limit shown in Fig 2.3) the motion is anharmonic. This is due to the compression of the molecule being more difficult than extension. Therefore Eqn 2.1 changes to,

$$E_v = (v+\frac{1}{2})h\nu_0 - (v+\frac{1}{2})^2 \chi\, h\nu_0$$

where χ is an anharmonicity constant.

The selection rule changes accordingly to,

$$\Delta v = \pm 1, \pm 2, \pm 3 \text{ etc..}$$

Polyatomic molecules possess more than one fundamental mode of vibration. Equation 2.1 for the energy of one vibrational energy level v_k of a particular fundamental mode of vibration ν_k therefore becomes,

$$E_{v_k} = \left(v_k+\frac{1}{2}\right)h\nu_k \qquad Eqn\ 2.2$$

where, v_k = 0,1,2...etc.[31]

For non-linear, polyatomic molecules the anharmonicity which exists relaxes the selection rule $\Delta v = \pm 1$ for lower energy levels to $\Delta v = \pm 1, \pm 2$ etc.. . The transition from the ground vibrational state (v=0) to the first vibrational energy level (v=1) is called the *fundamental transition*. Transitions from the ground vibrational state to higher vibrational energy levels (v=2,3...) are called *overtones*. *Combinations* occur when the quantum numbers of two vibrations change simultaneously. In this case, coupling between particular modes of vibration occurs, resulting in a transition at a well defined frequency. The combinations that can occur are strictly governed by the symmetry of the molecule.

Most importantly, no spectroscopic transitions are possible unless the vibrational transition is accompanied by a change in the molecular dipole moment. Furthermore, the frequency of a photon of radiation absorbed by the molecule which results in a transition from one vibrational energy level to a consecutive level is equal to the vibration frequency of the corresponding fundamental mode of vibration [31].

2.5 Transition Intensities

For most molecules at room temperature only the lowest vibrational energy levels, specifically the ground vibrational state (v=0), will be occupied. This, together with the relaxed selection rules on polyatomic molecules results in most vibrational energy level transitions being *fundamental transitions*, *overtones* or *combinations* as opposed to being transitions between consecutive higher energy levels. The intensity of transitions vary considerably (i.e. *overtone* transitions are much weaker than *fundamental* transitions). This is due to the different probabilities of transitions occurring between particular vibrational levels. The probability of a transition occurring from one vibrational energy level to another for the single normal mode of vibration of a diatomic molecule is proportional to the square of the integral,

$$M_z = \left(\frac{d\mu_z}{dQ}\right)_0 \int \psi_{v'}(Q)^* \, Q \, \psi_{v''}(Q) \, dQ \qquad Eqn\ 2.3$$

where, M_z is called the *transition moment* and z is the axis of the vibration [31].

$\left(\frac{d\mu_z}{dQ}\right)_0$ is a linear term giving the electric dipole moment change per unit displacement of the vibrating nuclei from their mean positions.
μ_z is the electric dipole moment of the molecule and Q is the *normal co-ordinate* which is directly related to the displacement of the atomic nuclei of the molecule when vibrating at its fundamental frequency.

$\psi_{v'}(Q)^*$ is the complex conjugate of the wavefunction for a particular vibrational energy level v' of the fundamental mode of vibration.

$\psi_{v''}(Q)$ is the wavefunction for a different vibrational energy level v'' of the fundamental mode of vibration [31].

If either $\left(\frac{d\mu_z}{dQ}\right)_0$ or $\int \psi_{v'}(Q)^* Q \, \psi_{v''}(Q) \, dQ$ is zero then no transition can occur. For polyatomic molecules the dipole moment μ and the transition moment M are vectors with components μ_x, μ_y, μ_z and M_x, M_y and M_z on the x, y and z cartesian axes. This added complexity to the above analysis of the diatomic molecule yields the

selection rule that only fundamental transitions should appear in infra red spectra. Fundamental transitions not associated with a change in the molecules electric dipole moment (i.e. $\left(\frac{d\mu_z}{dQ}\right)_0 = 0$) are forbidden to occur by the absorption of radiation.

Anharmonicity, as mentioned earlier, relaxes this selection rule somewhat resulting in *overtones* and *combinations*. In these cases the assumption used in the above analysis that $\left(\frac{d\mu_z}{dQ}\right)_0$ is linear is not fully correct. Secondly, the higher vibrational levels (v_k=2,3..etc) are not exact multiples of the frequency of the *fundamental transition* (i.e. $E_{v_k} \neq \left(v_k + \frac{1}{2}\right)h\nu_k$). Therefore the equation for the transition moment M_z varies from that above and consequently the "fundamental transition only" selection rule above does not rigorously hold [31].

The transitions and corresponding intensities for methane are shown in Table 2.1.

2.6 Rotational Features on Vibration Spectra

Pure rotational energy level transitions occur at micro-wave frequencies. No such transitions occur for molecules which have a centre of symmetry or, as with methane, have a tetrahedral symmetry (i.e. molecules with no permanent electric dipole moment) [31]. However, rotational transitions can accompany vibrational transitions. This occurs because the moment of inertia, and so the rotation energy of the molecule, is dependent on the bond length. These rotational transitions are between rotational energy levels of different vibrational energy levels as opposed to one vibrational energy level. Consequently, they are observed in the infra-red spectral region.

Rotational energy levels are quantised. The rotation of a molecule has three degrees of freedom. The total energy of rotation is,[31]

$$E_R = \frac{P_a^2}{2I_a} + \frac{P_b^2}{2I_b} + \frac{P_c^2}{2I_c} \qquad Eqn\ 2.4$$

where P_a, P_b and P_c are the components of the total angular momentum P along the principal axes a, b and c. I_a, I_b and I_c are the moments of inertia for each of these axes. The total angular momentum is given by,

$$P^2 = P_a^2 + P_b^2 + P_c^2 \qquad Eqn\ 2.5$$

There are four simplified separate classes for molecules of different symmetry. The highest symmetry is that of *spherical top* molecules where the principal axes a, b and c are of equal length and therefore $I_a=I_b=I_c$ [32]. Methane belongs to this class and using

Mode	Wavenumber (cm^{-1})	Wavelength (μm)	No. of lines	Total Line Intensity ($cm^{-2}atm^{-1}$) @ 296K
ν_1	3657	2.734	⊗	⊗
ν_2	1533	6.523	810	1.5
ν_3	3019	3.312	1,903	291
ν_4	1311	7.628	1,420	135.7
$2\nu_4$	2612	3.828	1,266	1.5
$\nu_2+\nu_4$	2830	3.534	2,300	10.1
$\nu_2+2\nu_4$	4123	2.425		0.16
$\nu_1+\nu_4$	4223	2.368	151	5.7
$\nu_3+\nu_4$	4340	2.304	958	11.0
$\nu_2+\nu_3$	4540	2.203	388	1.7
$\nu_3+2\nu_4$	5585	1.791		
$\nu_1+\nu_2+\nu_4$	5775	1.732		
$\nu_2+\nu_3+\nu_4$	5861	1.706		
$2\nu_3$	6005	1.666	142	1.4
$\nu_2+2\nu_3$	7514	1.331		0.3
$2\nu_1+2\nu_4$	8421	1.187		

⊗ This mode does not absorb infrared radiation because of its symmetry.

Table 2.1 Methane Overtones and their corresponding intensities

Eqn 2.4 with Eqn 2.5 above yields the total rotational energy for a spherical top molecule,

$$E_R = \frac{P^2}{2I} \qquad Eqn\ 2.6$$

The other three classes of molecules are *linear* (where I_a=0 and I_b=I_c), *symmetric top* (where two inertias are equal but different from the third e.g $I_a = I_b \neq I_c$) and *asymmetric top* (where $I_a \neq I_b \neq I_c$) [32]. The number of rules governing the quantisation of rotational energy levels differ for these different classes of molecules. *Spherical top* and *linear* molecules have just one as follows,

$$P = \sqrt{J(J+1)}\ \frac{h}{2\pi} \qquad J = 0, 1, 2 \ldots$$

Using this rule and Eqn 2.6 for spherical top molecules from above we get,

$$E_R = J(J+1)\frac{h^2}{8\pi^2 I} \qquad Eqn2.7 \qquad \text{or} \qquad \frac{E_R}{h} = J(J+1)B \qquad Eqn\ 2.8$$

where B is called the *rotational constant*.

Selection rules for transitions between rotational energy levels of different vibrational energy levels also vary according to the class of molecule. Again *spherical top* type molecules have just one rule,[33]

$$\Delta J = 0, \pm 1$$

Using Eqn 2.2 and summing over all the vibrational levels (v_k=0,1,2..) of all the different normal modes of vibration ν_k yields the total vibrational energy of the molecule,

$$E_v = \sum_k \left(v_k + \frac{1}{2}\right) h\nu_k \qquad Eqn\ 2.9$$

Adding Eqn 2.8 and Eqn 2.9 yields the total energy $E_{v,R}$ where,

$$E_{v,R} = \sum_k \left(v_k + \frac{1}{2}\right) h\nu_k + BhJ(J+1)$$

where v_k=0,1,2..etc. for each fundamental mode ν_k [31].

Thus the energy of the transition lines observed in a resulting absorption band are,

$$h\nu = \Delta E = h\nu_k + B'J'(J'+1) - B''J''(J''+1)$$

where B′ and J′ refer to the upper vibrational energy level, and B″ and J″ to the lower. Three sets of absorption lines occur due to transitions. These are the P branch (ΔJ=-1), the Q branch (ΔJ=0) and R branch (ΔJ=1). These branches are characterised as follows,[32]

$$h\nu_P = h\nu_k + (B'-B'')J^2 - (B'+B'')J$$

$$h\nu_Q = h\nu_k + (B'-B'')J^2 - (B'-B'')J$$

$$h\nu_R = h\nu_k + 2B' + (B'-B'')J^2 + (3B'-B'')J$$

The magnitude of the rotational constant B varies for each vibrational energy level. This is due to coupling between the vibrations and rotations. As a result the rotational energy levels are shifted. The consequence of this is that the spacings between the component lines of the spectrum for both the P and R transition branches are not equal [34]. Also, the Q branch, which is the most intense (because ΔJ=0 results in many transitions of nearly equal energy $h\nu_k$), is a set of closely spaced transition lines [31]. Fig 2.4 is an absorption spectrum for methane at the $2\nu_3$ overtone in the 1.66μm spectral region, showing the Q, P and R branches. This spectrum was taken using a Bomem DA8 fourier transform, infra-red spectrometer (FTIR), with a liquid nitrogen cooled Indium Antimonide (InSb) detector. The gas cell length was 10cm and the concentration was 100% methane. The resolution is 1 cm^{-1}. All spectra reported in this work were recorded at atmospheric pressure.

2.7 Linewidth Broadening

Spectral lines are not infinitely sharp as the above theory of absorption implies. The three main causes for broadening of spectral lines are,

a)Collisions : If a molecule which is emitting photons collides with another molecule, then the wave train associated with each photon is altered and is

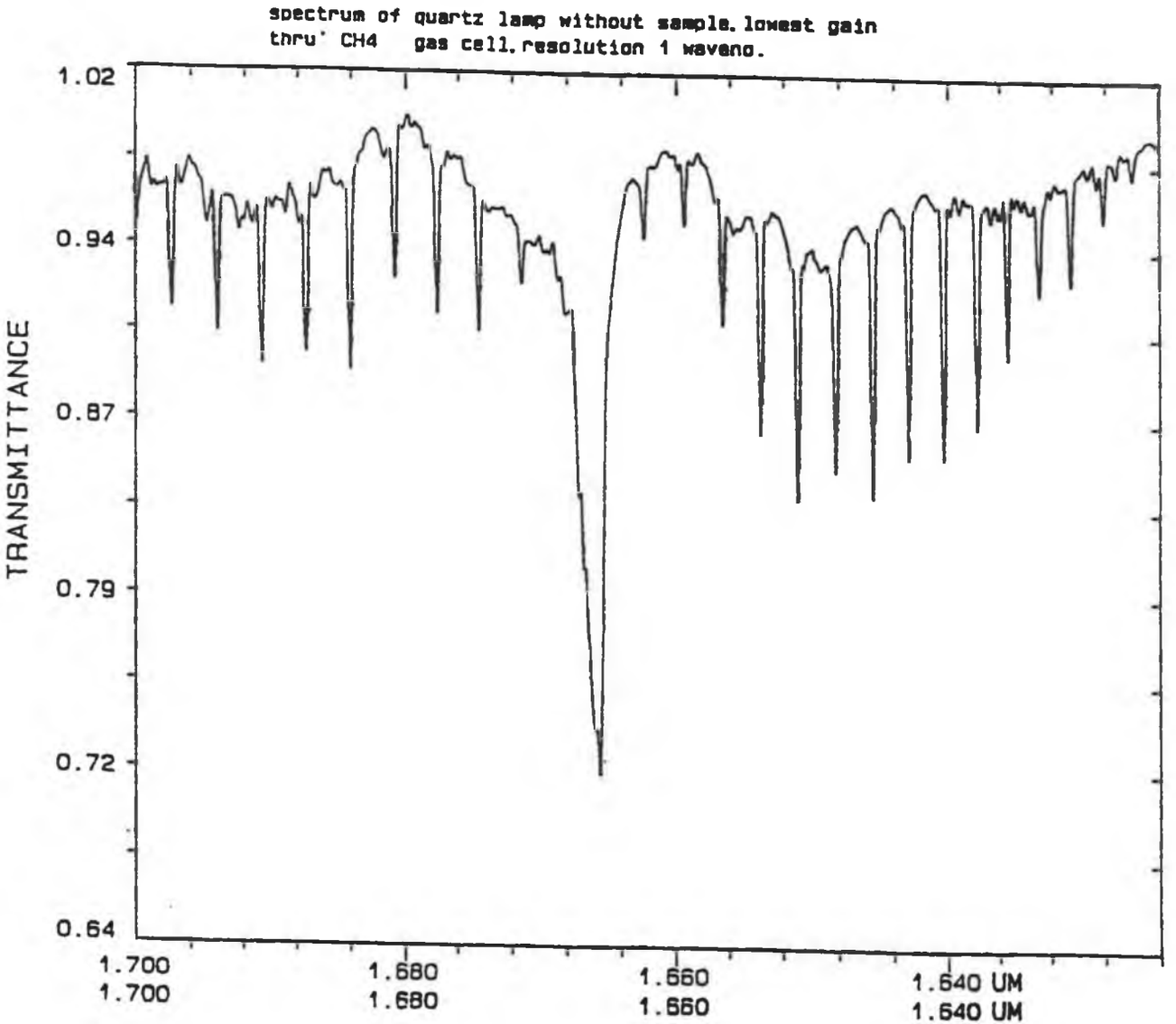

Fig 2.4 Spectrum of $2\nu_3$ overtone of methane using Bomen DA8 FTIR

effectively shortened. Fourier analysis shows that this is equivalent to spectral line broadening. If the gas pressure is increased then broadening also increases, as more molecular collisions occur.

b)Doppler Broadening: If a molecule, vibrating at a frequency ν_{vib}, and an observer are in relative motion, where v_x is the component of the velocity of the molecule along the direction of observation, then the observed frequency ν_{obs} of the molecule is given by,

$$\nu_{obs} = \nu_{vib} \left(1 \pm \frac{v_x}{c}\right)$$ where c is the speed of light.

The ± sign refers to the direction of the molecule; + if both molecule and observer are approaching one another, - if they are receding from one another. As the gas molecules have random motion then a range of frequencies are observed where ν_{obs} is either greater or less than ν_{vib}. The observed lineshape is therefore broadened.

c)Natural (Heisenberg) : According to Heisenberg's uncertainty principle, the energy of a state is only precisely defined if its lifetime is infinite. The lifetimes of excited states are finite and depend on the Einstein *A* coefficient of spontaneous emission. This represents the irreducible minimum linewidth of any spectroscopic transition [32].

Chapter 3

Experimental System

3.1 Introduction

This chapter describes the design of the experimental methane gas sensing system. The Beer-Lambert Law is discussed in section 3.2, and an expression for gas absorption is calculated for the two filter, "differential absorption" system. Section 3.3 describes the individual optical components in the system including an introduction to the novel LED source, the fibre optic coupler, the fiberised collimating lenses and the retroreflector. The interference filters are then treated in some detail. Section 3.4 describes the systems electronic components and circuitry and an analysis of the detector/pre-amplifier noise is undertaken. Finally, the data detection and processing techniques are outlined in section 3.5. This includes an overview of the software method used to calculate standard errors on the detected signals.

The fibre optic remote sensing system for methane gas shown in Fig 3.1 was designed and constructed. Infra-red light in the 1.6μm spectral region is coupled from a novel edge-emitting LED source into an optical fibre and conveyed to port 1 of a 3dB fibre optic coupler. Half of the signal is coupled into port 2, and the remainder into port 3. Port 3 is mechanically connected to a single-mode fibre pigtail using an FC type fibre connector. The light emitting from this fibre is collimated by a lens of focal length 60mm. The collimated beam propagates through a 70 centimetre long gas cell and is absorbed according to the Beer Lambert law (see section 3.2). When incident on the retroreflector, the attenuated beam is reflected back along the same path through the gas cell to the lens, thereby increasing the absorption path length to 1.4 metres. The net attenuated beam is then focused by the lens back into port 3 of the coupler via the single-mode fibre pigtail where the signal is again divided by the coupler - 50% into port 1 and 50% into port 4. The signal in port 4 is used for the data collection process which is now outlined.

A fiberised collimating graded index (GRIN) lens, fusion spliced to the distal end of the port 4 fibre, collimates the signal beam which then passes through a modified chopper wheel system holding two optical interference filters. One filter

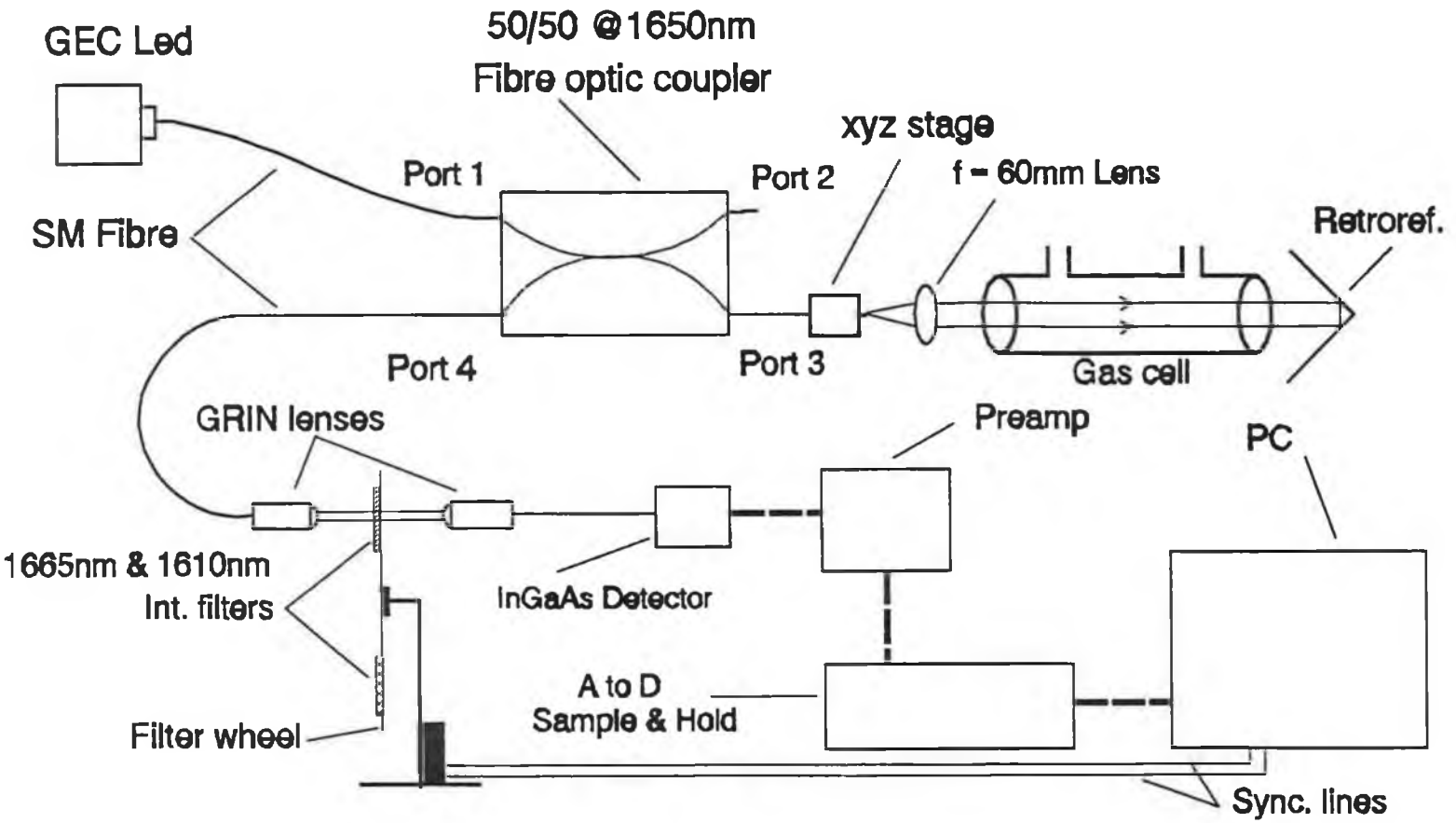

Fig 3.1 Experimental System Block Diagram

transmits only light at the gas absorbing wavelength and the other transmits at an adjacent, non-absorbing (or reference) wavelength. A second fibre, terminated with a GRIN lens and fusion spliced to a pigtailed detector, alternately collects the signals at both wavelengths. The speed of collection is determined by the filter wheel rotation speed. The detector is followed by a current sensitive pre-amplifier with a gain of up to 10^9 volts per ampere. Synchronous detection of signals and analogue to digital conversion follow and the associated software then processes the data to yield absorption figures as a function of concentration.

3.2 The Beer-Lambert Law

In this system, collimated infra-red light gets absorbed by methane gas according to the Beer-Lambert Law which states that,

$$I_\lambda = I_{o\lambda} \exp(-\alpha_\lambda bc) \qquad \text{..... Eqn 3.1}$$

where in the context of the work under investigation, I_λ is the intensity of the infra-red light of wavelength λ after propagating through a distance b (in metres), of gas of concentration c (measured as a fraction of the total gas volume). $I_{0\lambda}$ is the intensity of the infra-red light signal at the wavelength λ after propagating through the distance b when c=0 (i.e. no absorbing gas present). α (in m^{-1}) is called the absorption coefficient, which quantifies the degree of absorption of light by methane at a particular wavelength.

The two interference filters used in the system transmit at 1665nm and at 1610nm corresponding to "on" and "off" absorption wavelengths, respectively. The value for I_λ in each case is given by

$$I_{\lambda on} = I_{0\,\lambda on} \exp(-\alpha_{on} bc) \qquad \text{..... Eqn 3.2}$$

$$I_{\lambda off} = I_{0\,\lambda off} \exp(-\alpha_{off} bc) \qquad \text{..... Eqn 3.3}$$

Dividing Eqn 3.2 by Eqn 3.3 yields,

$$\frac{I_{\lambda on}}{I_{\lambda off}} = \frac{I_{0\ \lambda on}}{I_{0\ \lambda off}} \exp\ [-bc(\alpha_{on}-\alpha_{off}] \qquad \text{..... Eqn 3.4}$$

Finally,

$$-\ln\left(\frac{I_{\lambda on}}{I_{\lambda off}} \cdot \frac{I_{0\ \lambda off}}{I_{0\ \lambda on}}\right) = bc[\alpha_{on}-\alpha_{off}]$$

or,

$$\ln\left(\frac{I_{0\ \lambda on}}{I_{0\ \lambda off}} \cdot \frac{I_{\lambda off}}{I_{\lambda on}}\right) = bc[\alpha_{on}-\alpha_{off}] \qquad \text{..... Eqn 3.5}$$

On examination of Eqn 3.5, it can be seen that the function $\ln\left(\frac{I_{\lambda off}}{I_{\lambda on}}\right)$ need only be calculated for various concentrations c of gas, to obtain a calibration curve for the system, as the value $\frac{I_{0\ \lambda on}}{I_{0\ \lambda off}}$ is a constant.

However, plotting $\ln\left(\frac{I_{0\ \lambda on}}{I_{0\ \lambda off}} \cdot \frac{I_{\lambda off}}{I_{\lambda on}}\right)$ versus c yields a straight line whose slope is given by,

$$slope = b[\alpha_{on}-\alpha_{off}] \qquad \text{..... Eqn 3.6}$$

This plot not only supplies a calibration curve for the system but also gives a value for the differential absorption coefficient $\alpha_{on}-\alpha_{off}$.

3.3 Optical Components

This section describes the various optical components used in the system and begins with an introduction to the novel LED source used. The fibre optic coupler is described together with coupler terminology. The construction and operation of the interference filters is discussed. The optics at the gas cell are also described.

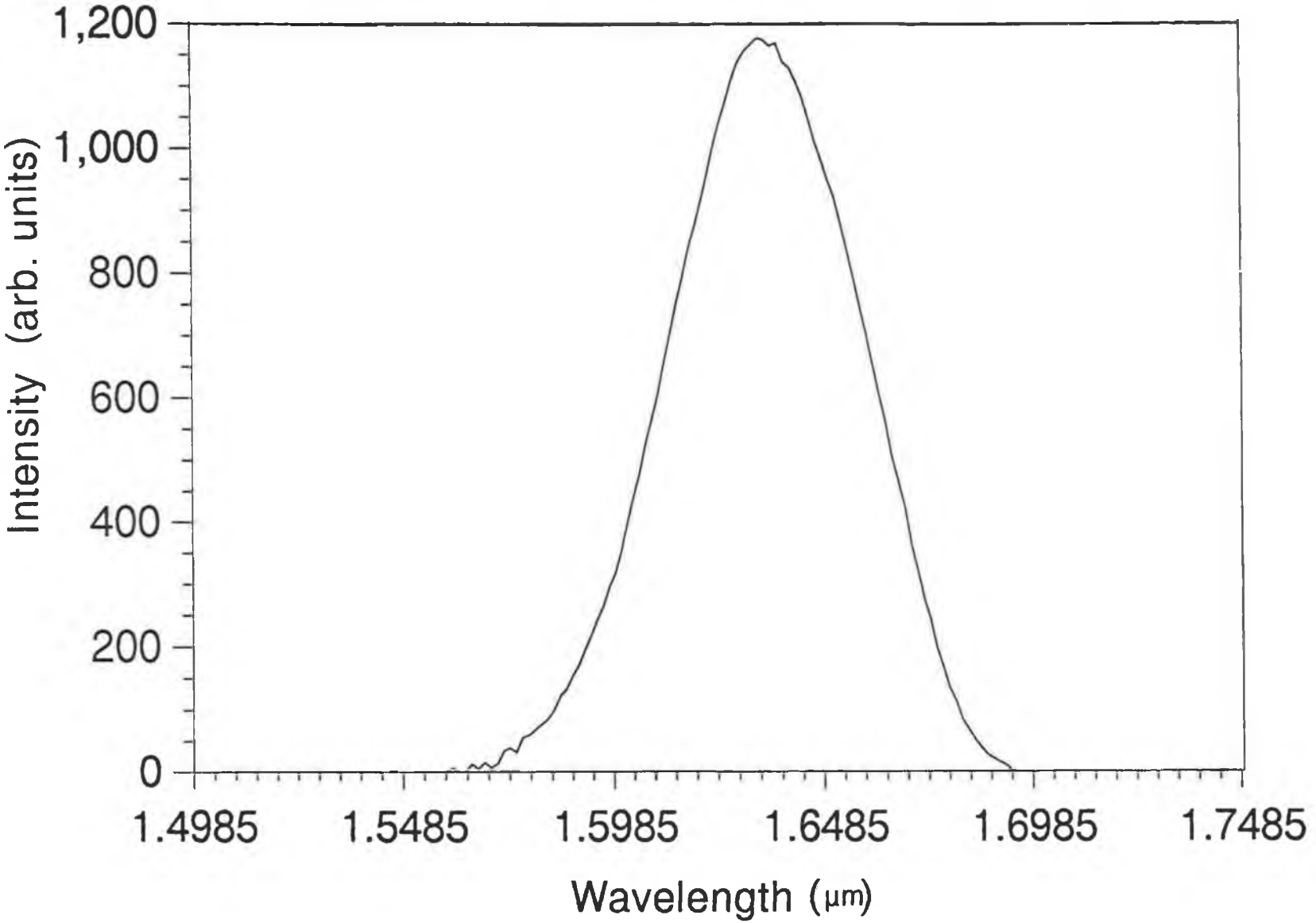

Fig 3.2 LED Spectrum at 100mA Drive Current

3.3.1 LED Source

The novel LED source used is manufactured by GEC-MARCONI Materials Technology Ltd., Caswell, U.K. The device is pigtailed to single-mode silica fibre (9μm/125μm). It has a peak wavelength of 1.6335μm with a full width at half maximum of 53nm and couples approximately 50μW of power when operated at a driving current of 100mA. This emission spectrum, shown in Fig 3.2, overlaps the $2\nu_3$ overtone absorption band of methane.

The LED is effectively a laser diode with a proton implanted region at one end of the active region, which acts to reduce reflection considerably at this point. It therefore prevents feedback within the cavity and as a result, the lasing threshold is high. The LED is fabricated through a two stage Metal Organic Vapour Epitaxy (MOVPE) process. It consists of a wafer with a 0.15μm active GaInAs region clad with InP which is then overgrown with P-type InP and GaInAs layers to provide current confinement and optical guiding. A section through the LED's active region is shown in Fig 3.3. There is an anti-reflection coating of Al_2O_3 on the chip's emission area which increases output power by reducing the magnitude of the wasteful backward travelling wave within the active region. A thermistor is also incorporated for chip temperature monitoring [35]. A more detailed characterisation of the LED source is described in section 4.2.2.

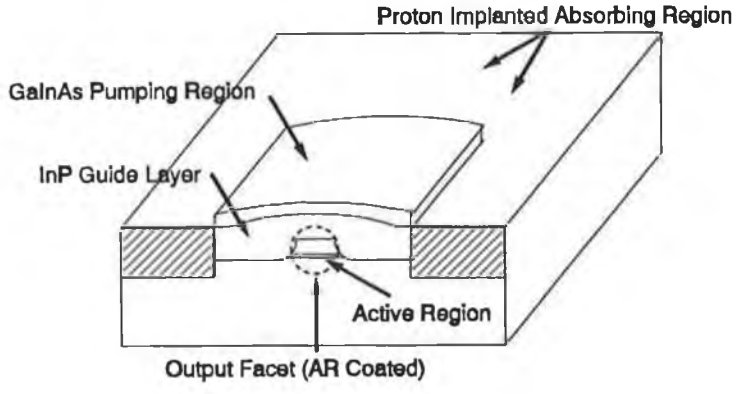

Fig 3.3 Section through LED active region

3.3.2 Fibre Optic Coupler

A single-mode, 2x2, fused directional fibre optic coupler was manufactured

for the system by Aster (Ireland). The coupler splits an input signal in the 1650nm spectral region into two output ports with approximately 50% of the signal into each. A schematic diagram is shown in Fig 3.4. The coupler was boxed and ruggedised using jacketed fibres. This type of coupler is based on evanescent wave coupling between two fibres. The strength of the coupling is determined by the separation of the fibre cores, the extent to which the evanescent field spreads into the cladding and the length of the coupling region. The couplers are manufactured by twisting two fibres around one another and heating them in an arc or a flame. The fibres are fused and tapered while the transmitted powers at the output ports (Port 2 and Port 3 in Fig 3.4) are monitored continuously. When the appropriate ratio is measured the tapering is stopped. These couplers are called "directional" because power is coupled mostly in the forward direction (i.e. to Port 2 and Port 3 as opposed to Port 4) [36].

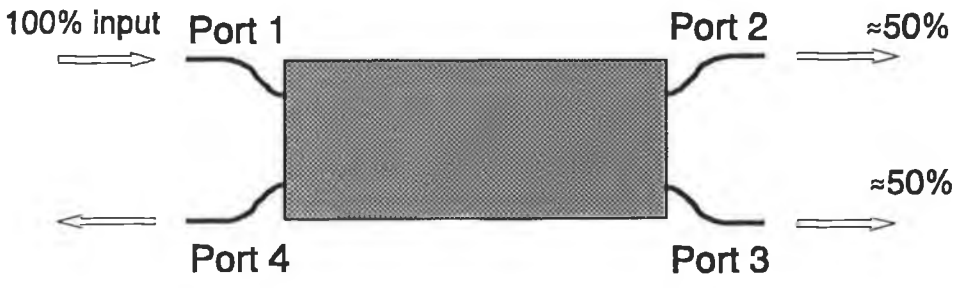

Fig 3.4 2*2 3dB Directional Coupler

The performance parameters for a coupler are as follows:

Directivity : The coupler is designed to couple the input light in Port 1 equally between Port 2 and Port 3 at a particular wavelength. However, a small proportion of this light is coupled into the Port 4 input. This process is called "backscatter". The directivity is a measure of this backscatter and is given by

$$Directivity_{PORT1} = -10 \log \left[\frac{P_4}{P_1} \right] \quad (in\ dB)$$

where P_1 and P_4 are the powers at Port 1 and Port 4 respectively.

The output ports, Port 2 and Port 3 are immersed in index matching fluid to prevent back reflections interfering with the measurement.

Passband : This is the wavelength range around a centre wavelength over which the coupler performance is specified. Coupling between output ports is wavelength dependent and so wavelength is always specified with the coupler.

Coupling Ratio (or Splitting Ratio) : This is a term used to describe the power splitting behaviour of the coupler (i.e. how the total output power is split between the output ports). The ratio is wavelength dependent and is usually given in percentage form.

$$Coupling\ Ratio - Port\ 2 = 100 \times \frac{P_2}{P_2+P_3} \quad (in\ \%)$$

$$- Port\ 3 = 100 \times \frac{P_3}{P_2+P_3} \quad (in\ \%)$$

where P_2 and P_3 are the powers at Port 2 and Port 3 respectively.

Excess Coupler Loss : This is the total power lost in the coupler and never recaptured at any of the output ports. It gives a figure of merit for the overall efficiency of the coupler.

$$Excess\ Loss = -10 \log \left[\frac{P_2+P_3}{P_1}\right] \quad (in\ dB)$$

Insertion Loss : This is the most important optical performance parameter for couplers. The insertion loss is the total loss for any light path from a specific input port, through the coupler to a specific output port. It includes any excess loss contributions incurred on that specific light path. It is wavelength dependent.

$$Insertion\ Loss - Port\ 2 = -10 \log \left[\frac{P_2}{P_1}\right] \quad (in\ dB)$$

$$- Port\ 3 = -10 \log \left[\frac{P_3}{P_1}\right] \quad (in\ dB)$$

Values for the coupling loss, insertion loss and excess loss of the coupler used in this work are shown in Table 3.1.

3.3.3 Fiberised Collimating Lenses

Two SELFOC® fibre collimators, manufactured by Nippon Sheet Glass Co., Tokyo, Japan, are used in the system. Each consists of a graded index (GRIN) lens directly connected to one end of a 1 metre length of single-mode fibre. The other end of one such fibre collimator is fusion spliced to the single-mode fibre of port 4 of the coupler. It collimates the infra-red beam before the beam passes through the interference filters. The far end of the second fibre collimator is fusion spliced to the multimode fibre of a pigtailed detector. This avoids the need for bulk optics at the detection end and ensures that most of the power in the fibre collimator will be

Wavelength (nm)	Insertion Loss (dB)		Coupling Ratio (%)	Excess Loss (dB)
	Port 2	Port 3	Port 3	
1600	3.16	3.16	49.95	0.15
1610	3.22	3.11	50.60	0.15
1620	3.28	3.06	51.26	0.16
1630	3.35	3.01	51.93	0.17
1640	3.41	2.98	52.48	0.18
1650	3.45	2.94	52.95	0.18
1660	3.50	2.92	53.34	0.19
1670	3.54	2.93	53.51	0.21
1680	3.57	2.99	53.35	0.26
1690	3.57	3.17	52.30	0.36
1700	3.63	3.54	50.52	0.58

Table 3.1 Coupler Specifications

detected. This collimator collects the signal transmitted through the filters and refocuses it into the fibre system.

Fibre collimators are designed so that there is no air gap between the fibre end and the GRIN lens, thereby avoiding transmission losses due to glass-air reflections. The GRIN lens is a cylindrical glass rod in which the refractive index varies radially, decreasing parabolically out from the central axis. This variation is described by,

$$n(r) = n_0\left(1 - \frac{ar^2}{2}\right) \qquad \text{..... Eqn 3.7}$$

where, n(r) is the refractive index as a function of lens radius.

n_0 is the refractive index on lens axis (r=0).

a is the *focusing parameter*. It describes the refractive index grading.

The output beam from a single-mode fibre end with spot size w_F is diffracted upon entering the GRIN lens and its planar wavefront changes shape as it progresses through the lens as can be seen in Fig 3.5. This is due to different portions of the wave propagating at slightly different speeds through the lens. The input beam is continuously refracted in such a way that the beam spot size w_L in the lens varies between a maximum $w_{L\,MAX}$, and a minimum where $w_{L\,MIN} = w_F$. The distance between the lens input point where the beam undergoes initial refraction and the point where this same refraction cycle is repeated is known as the *pitch* where,

$$p = \frac{2\pi}{\sqrt{a}}$$

At one quarter the pitch length, the beam spot size is $w_{r\,MAX}$. The wavefront is planar and diffracts very slowly. By designing GRIN lens lengths equal to ¼ pitch or an odd multiple of ¼ pitch the output beam is collimated. Because of the periodic nature of a GRIN lens it is possible to obtain collimated (¼p), inverted focus (½p), inverted collimated (¾p) and upright focus (p) depending on the length of the lens. GRIN

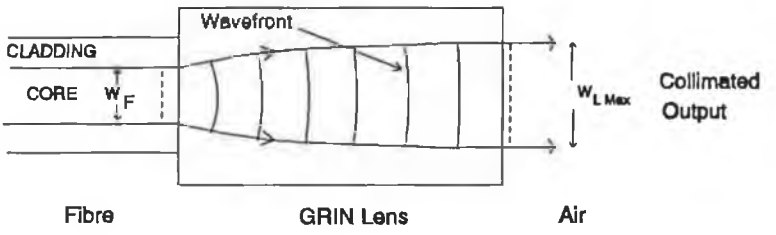

Fig 3.5 Progression of Wavefront through GRIN lens

lenses are wavelength dependent because of the focusing parameter "a" and the radially varying refractive index which are both wavelength dependent [36,37,38].

The fibre collimators used in the system here are single-mode, ¼ pitch at 1.56μm. This is the wavelength closest to the 1.66μm spectral region which is commercially available. The approximate coupling efficiency between both fibre collimators was measured to be 65% or equivalently a loss of 1.87dB. This falls within the given specification of <2dB for a 10mm separation.

3.3.4 Fusion Splicing

Fusion splices are permanent fibre to fibre connections which have the lowest losses of all fibre connection techniques. The system incorporates three fibre optic *fusion splices*. The first is between the pigtailed LED source and the single-mode fibre of port 1 of the coupler. The second is between a fibre collimator and the single-mode fibre of port 4 of the coupler and the third is between a second fibre collimator and a pigtailed detector. In the fusion splicing process a localised heating (typically 1730°C for silica fibres) is applied at the interface between two, pre-aligned fibre ends. This causes the fibre ends to soften and to fuse together. Single-mode fusion splices have a loss of typically less than 0.1 dB. This loss is primarily due to the slight distortion of the waveguide. Fusion splices restore the strength of the joint to approximately 70% of the original waveguide [38]. The fusion splicing was carried out at Aster (Ireland) in Limerick.

3.3.5 Optical Filters

The two optical interference filters used in the system were fabricated by Glen

Spectra Ltd., Middlesex, U.K. Each filter is 5mm thick and 25mm in diameter. The on-absorption filter at 1665nm has a bandwidth at half maximum (BWHM) of 2nm and has a peak transmission of 61%. This coincides with the peak absorption wavelength at the Q-branch of the $2\nu_3$ overtone of methane. The off-absorption reference filter at 1610nm has a BWHM of 5nm with a peak transmission of 60%. This wavelength coincides with a non-absorbing wavelength outside the $2\nu_3$ overtone spectral region. The construction of the 1665nm filter is shown in Fig 3.6. The second filter is similarly constructed. The actual filter component comprises two Fabry-Perot type cavities. Each cavity consists of a central dielectric *spacer layer* of high refractive index n_H whose "optical thickness" (i.e. $n_H \times d$, where d is the thickness of the spacer layer) equals one half the desired transmitted wavelength λ. Two quarter-wave stacks, placed on either side of the spacer layer, act as high efficiency reflectors.

The Fabry-Perot cavity operates by multiple beam interference created by reflected waves within the cavity as shown in Fig 3.7. The phase differences between the transmitted rays arise from a combination of optical path length differences and phase shifts occurring at the internal reflections.

The difference in optical path length between any two adjacent transmitted rays is given by,

$$\Lambda = 2n_H\, d\, Cos\, \theta_t$$

where, n_H is the high refractive index of the spacer layer

d is the thickness of the spacer layer

θ_t is the angle which the beam between the surfaces makes with the surface normal.

The phase difference between both rays is,

$$\delta = k_o \Lambda + \phi_A + \phi_B$$

where, k_o is the propagation constant ($= 2\pi/\lambda$) and

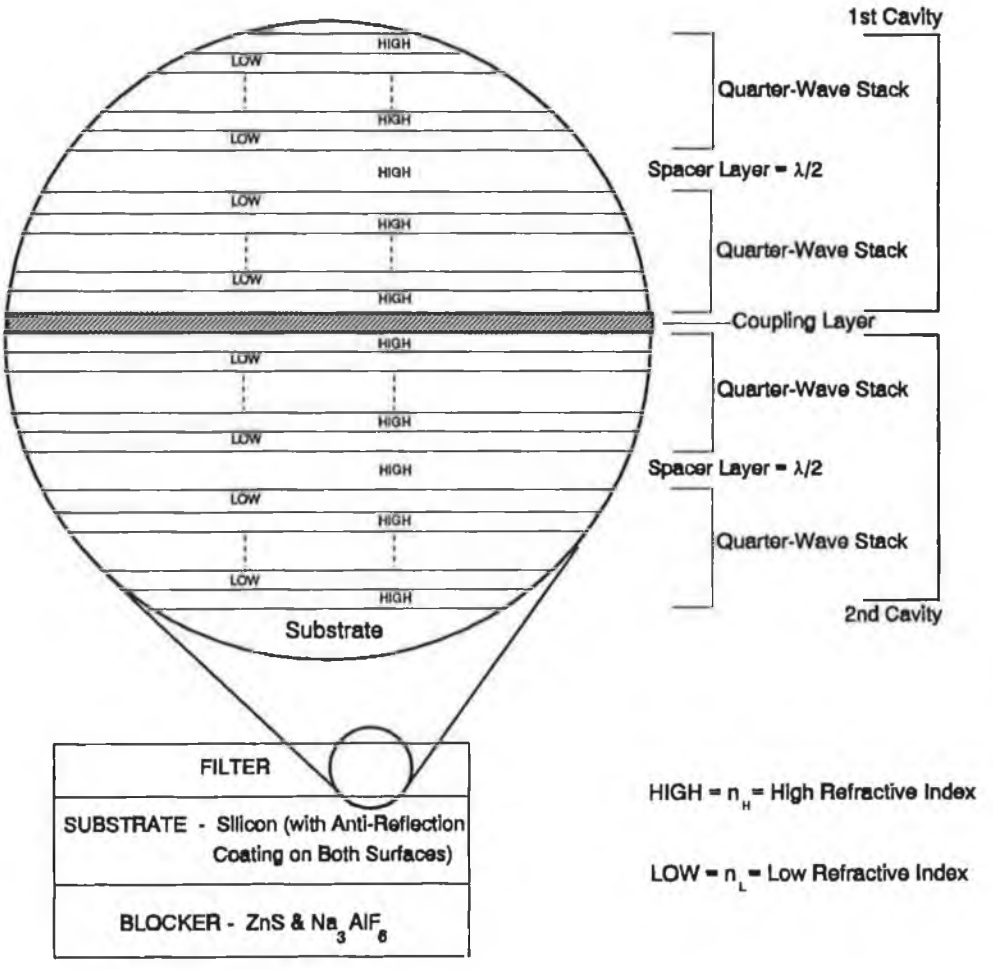

Fig 3.6 Interference Filter Construction

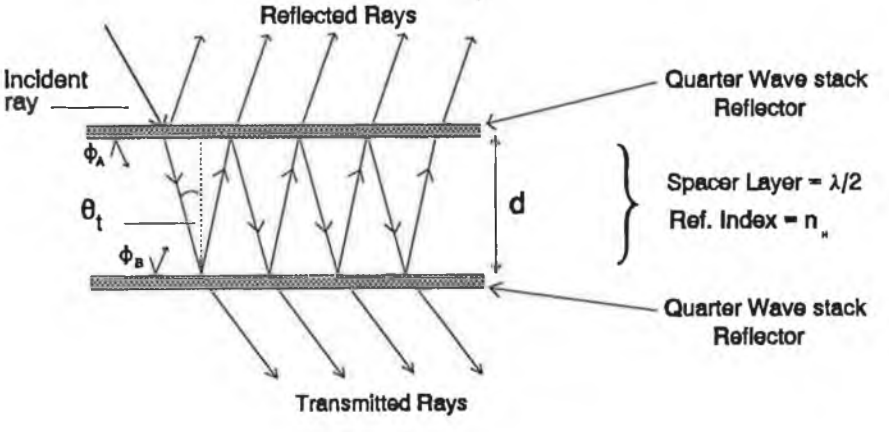

Fig 3.7 Operation of Fabry-Perot Cavity

ϕ_A, ϕ_B are respectively the phase shifts that occur on internal reflection at the interfaces between the spacer layer and the quarter-wave reflector stacks. These differ from 0 to π depending on the angle θ_i.

The irradiance of the transmitted beam (assuming there is no absorption of light in the dielectric media) is I_t where,

$$I_t = I_i \cdot \left(\frac{1}{1 + F \sin^2(\frac{\delta}{2})} \right) = I_i \cdot A(\theta) \quad \text{..... Eqn 3.8}$$

F is called the *coefficient of finesse* and is related to the reflectance R of each quarter -wave stack by

$$F = \frac{4R}{1-R^2} \quad \text{..... Eqn 3.9}$$

The reflectance R, is assumed to be equal for both stacks and has a value close to unity.

A(θ) is known as the Airy Function. It represents the transmitted flux density of the filter cavity. When the phase difference δ is equal to $2\pi m$, where m is any integer number, then A(θ) equals unity for all values of R. If R is close to unity the transmitted flux density is small except for very sharp transmission peaks centred about the points $\delta=2\pi m$ as shown in Fig 3.8.

The peak transmission at each of these peaks is $(I_t)_{max}$ and is given by,

$$(I_t)_{max} = I_i$$

The half maximum irradiance points are at $\delta=\delta_{max}\pm\delta_{½}$. At $\delta_{½}$, A(θ)=½ and using Eqn 3.7 it can be shown that the halfwidth $2\delta_{½}$ of the transmittance peak is,

$$\Delta\delta = 2\delta_{1/2} = \frac{4}{\sqrt{F}}$$

Because the phase difference δ (=$2m\pi$) is a function of λ then the transmitted peaks are at wavelengths given by,

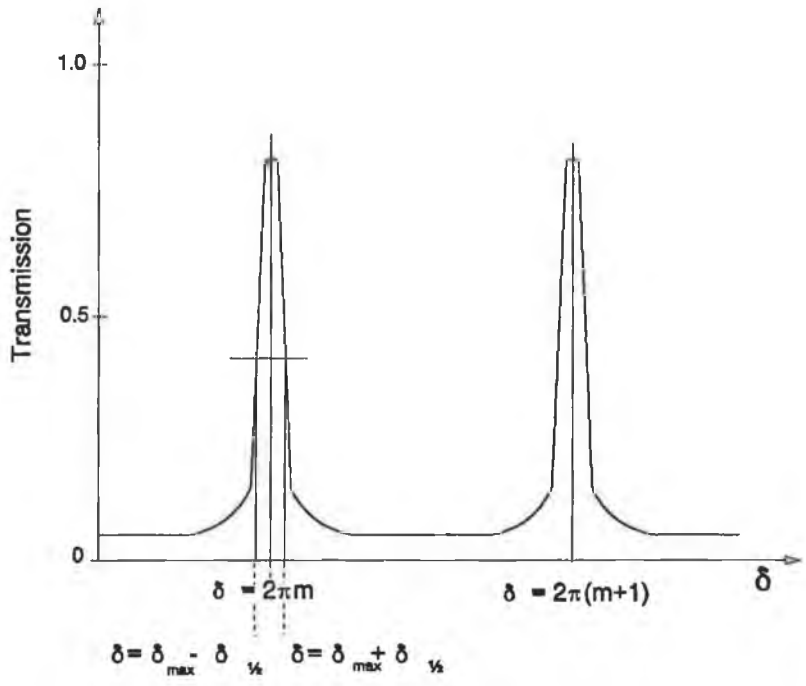

Fig 3.8 Fabry-Perot Transmission Peaks

$$m\lambda = 2d\, n_a \cos\theta_t + \frac{(\phi_A+\phi_B)\lambda}{2\pi} \quad \text{..... Eqn 3.10}$$

Assuming that the phase function due to the quarter-wave stacks is small compared with that due to the optical path length difference and that the spacer layer thickness d is equal to $\lambda/2$ then for normal incidence (i.e. $\theta_t=0$), the transmitted peaks are at λ, $\lambda/2$, $\lambda/3$ etc. for m=1,2,3 etc..

The fractional bandwidth at half maximum for the transmission peaks in terms of wavelength is,

$$\frac{\lambda}{\Delta\lambda} \equiv \frac{\delta_{max}}{\Delta\delta} = \frac{2m\pi}{4/\sqrt{F}} = \frac{m\pi\sqrt{F}}{2}$$

where $\Delta\lambda$ is the bandwidth of the transmission peak [39].

Quarter-wave Stack Reflectors

It has already been seen that the closer the reflectance value R is to unity in

the Fabry-Perot cavity, then the narrower the bandwidth of the transmission peaks. This is critical for narrowband-pass filters as in the case of the 1665nm filter whose bandwidth is 2nm. Two quarter-wave stacks form the high reflectors needed within the Fabry-Perot cavity. Fig 3.9 shows the basic operation of a quarter-wave stack.

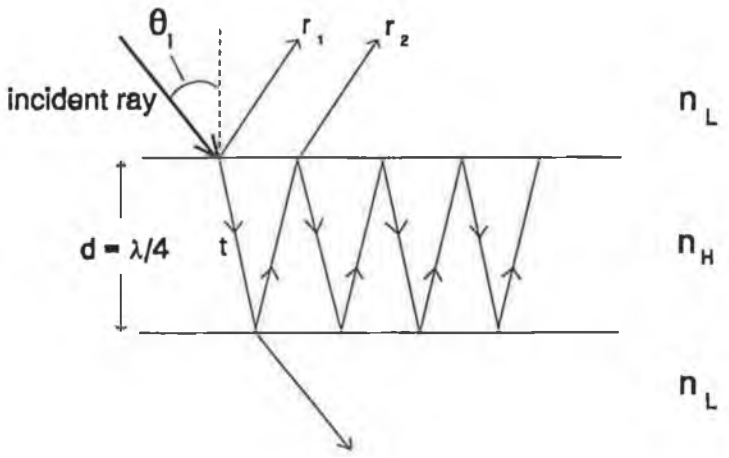

Fig 3.9 Operation of a Quarter-Wave Stack Reflector

When light from one medium is incident on a medium of greater refractive index (i.e. $n_L<n_H$), the reflected wave at the interface, r_1, undergoes a phase shift of π radians relative to the incident wave. If the transmitted beam t in the high index medium is then incident on a second interface with the low index medium the resulting reflected wave, r_2 does not undergo a phase change. Furthermore, no phase change occurs when r_2 is incident on the first interface. If the "optical thickness" of the high index medium is equal to a quarter of the incident wavelength (i.e. $d \times n_H = \lambda/4$) then the optical path length difference between r_1 and r_2 for normal incidence (i.e. $\theta_i=0$) is,

$$\Lambda = 2d\, n_H = \frac{\lambda}{2}$$

The phase change in r_2 relative to the incident created by the optical path length difference is given by

$$\delta = k.\Lambda = \frac{2\pi}{\lambda} \cdot \frac{\lambda}{2} = \pi$$

Because r_1 is also out of phase by π with the incident beam then both it and r_2 are in phase with each other and combine to give a large reflectance value. This process of constructive interference of reflected rays is repeated through the multi-layer stack thereby creating a very high reflectance value.

In real all-dielectric interference filters there is always some absorption of light by the quarter-wave stacks. As a result the peak transmission ($I_{t\,max}$) at the desired wavelength λ, is typically 60% to 70% of the incident irradiance I_i at that wavelength. Multiple Fabry-Perot cavities in a single filter improve the bandshaping of the filters transmission. For all-dielectric filters with N cavities, each having a high index spacer layer and an even number of high index layers, x, in each quarter-wave reflector stack, it can be shown that the fractional halfwidth of the transmitted wavelength λ is given by [40]

$$\left(\frac{\Delta\lambda}{\lambda}\right) = \frac{4n_H n_L^{2x}}{N\pi n_H^{2x+1}} \cdot \frac{(n_H - n_L)}{(n_H - n_L + \frac{n_L}{N})} \qquad \text{..... Eqn 3.11}$$

A transmission schematic of the two cavity, filter component of the 1665nm filter is shown in Fig 3.10a. The large transmission sideband occurs because the quarter-wave stack reflectance R decreases very quickly for wavelengths on either side of the Fabry-Perot sharp transmission wavelength of 1665nm. In order to prevent the ultra violet and visible radiation transmitting through the filter, *blocking* is required. The substrate on which the filters high and low index layers are grown is silicon which has anti-reflection coatings on each surface. The transmission of the substrate is shown schematically in Fig 3.10b. A quarter-wave stack is used to block light by reflection from 1100nm to 1550nm. This is fabricated from Zinc Sulphide (ZnS) which has a high refractive index of approximately 2.3 at 1.5μm and Cryolite (Na_3AlF_6) which has a refractive index of <1.35 at 1.5μm. The blocker transmission is shown in Fig 3.10c. The finished filter has a transmission equal to the product of the transmissions for the blocker, substrate and the filter as is shown in Fig 3.10d. The 1665nm filter transmission peak is 61% and the average "out of band" blocking

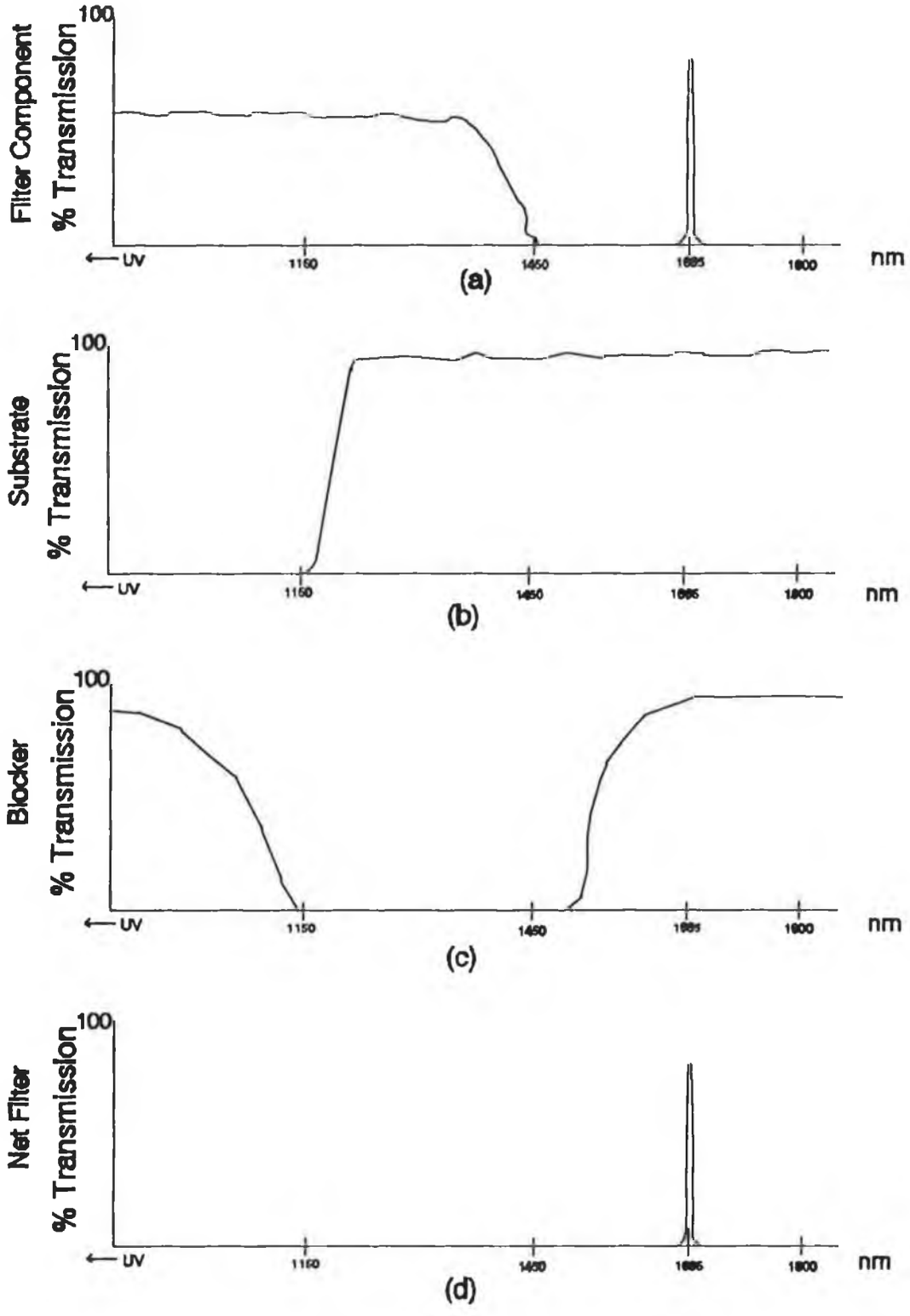

Fig 3.10 Transmission of Filter Components

from the UV to 1800nm is <1 x 10^{-4}. This means that the average percentage of transmitted light over the UV to 1800nm range, not including the transmission pass band at 1665nm, is less than 0.01% of the incident light over the same range.

3.3.6 Gas Cell Optics

The gas cell is 70cm in length and made from aluminium. Windows of 1mm thick silica glass are fitted on either end to seal the cell. A lens with focal length 60mm is then fitted at one end to collimate light from port 3 of the fibre optic coupler. At the other end a retroreflector, manufactured by Melles Griot Ltd, Cambridge, U.K, is fitted to reflect the incident signal directly back through the cell thereby doubling the absorption path length. The retroreflector consists of three flat gold-plated mirrors assembled at 90° to each other to form a cube corner. A schematic of its operation is shown in Fig 3.11.

As can be seen ray the reflected ray A′ travels along a path parallel to the incident ray A. The gold-plating on the mirror surfaces gives a reflectance value of ~99%. The retroreflector has a beam parallelism of 5 arc seconds (i.e. the reflected beam A′ deviates from parallelism to the incident ray A by 5 seconds of a degree). The ratio of retroreflected power coupled into port 3 to the incident power into the gas cell for 100%N_2 is approximately 0.13.

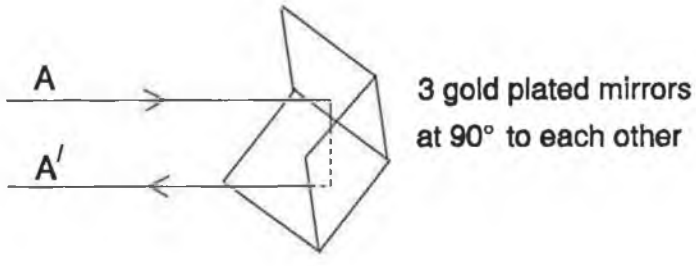

Fig 3.11 Operation of Retroreflector

3.4 Electronic Components

This section describes the electronic components in the gas sensing system and outlines the electronic circuitry required for each component. Detector/pre-amplifier noise is analyzed in detail and its influence on detected signals is evaluated. The data collection and processing techniques are also described. A diagram of the

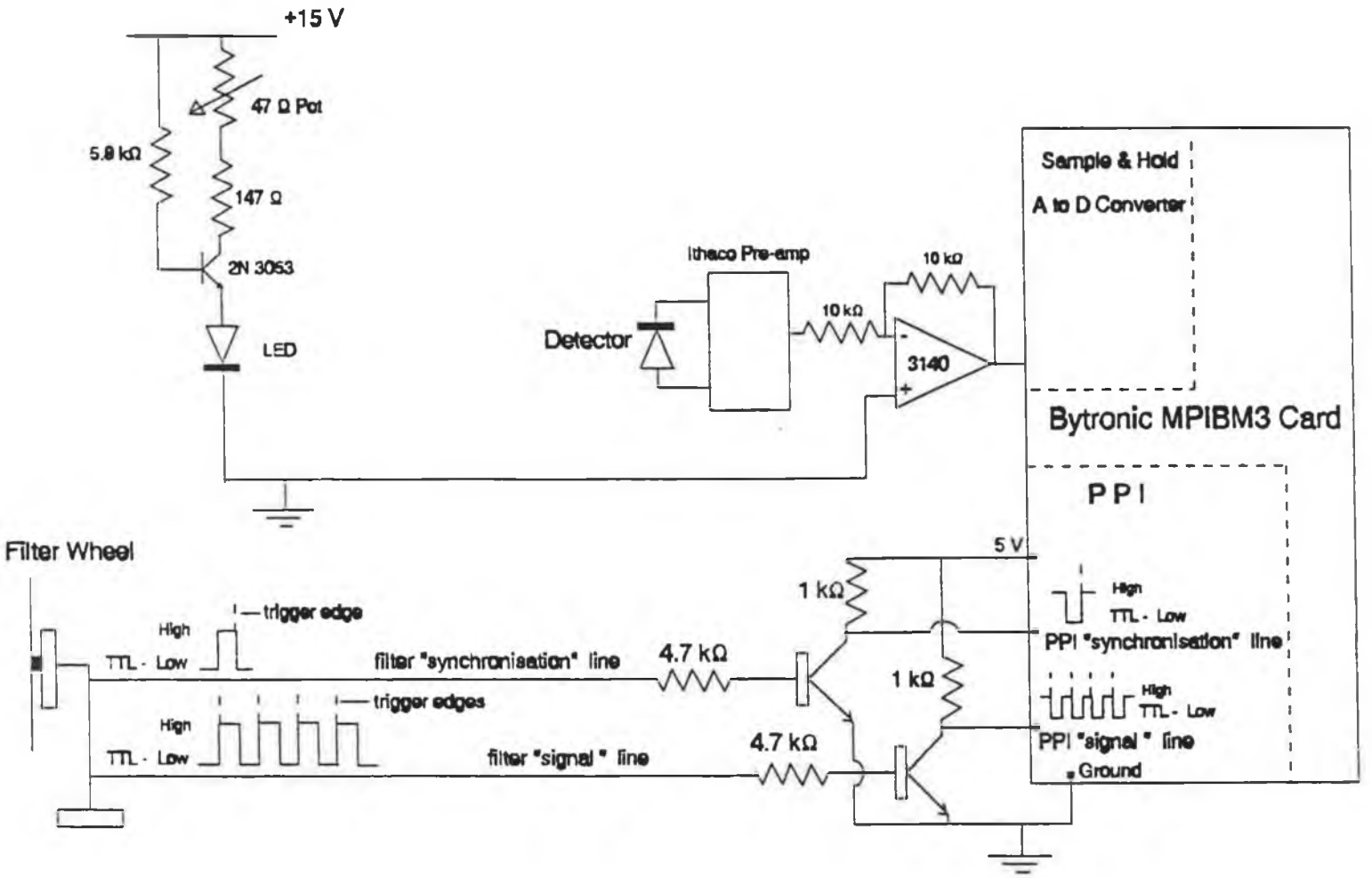

Fig 3.12 System Electronics Diagram

electronic circuitry is shown in Fig 3.12.

3.4.1 Led Circuitry

The LED driving electronics is shown in Fig 3.12. The 15V supply voltage rail also drives the 3140 operational amplifier in the detector circuit. The base current in the 2N3053 transistor is a few milliamps. The 47Ω potentiometer in the collector circuit allows the LED drive current to be varied up to a maximum of 100mA.

3.4.2 Detector & Pre-amplifier

An Epitaxx ETX 300T planar PiN photodiode is used in the system. It is pigtailed to a 20cm length of 100μm/140μm multimode fibre. It has a responsivity of 0.85 A/W over a 50 nm spectral region centered about 1.63μm with an active diameter of 300μm (area= $7x10^{-8}m^2$). The pigtail is fusion spliced to the single-mode fibre of a collimating GRIN lens. The detector spectral response is shown in Fig 3.13.

The photodiode is operated in the *photovoltaic* mode whereby there is no external biasing of the device. A linear output current response to incident irradiation is only obtained for low incident light levels (as is the case with this system) and when the detector is followed by a low load impedance R_L in the detection circuit. Therefore the device is connected across the virtual-earth inputs of a transimpedance (i.e. current to voltage) Ithaco Instruments Model 1642 pre-amplifier. This is a low noise device with a gain factor of up to 10^9 V/A. A schematic diagram of the circuit used is shown in Fig 3.14. The current I flowing through the feedback gain resistor R_F is directly proportional to the light intensity falling on the detector. The output from the pre-amplifier is $V_{out}= -IR_F$.

3.4.2.1 PIN Photodiodes

PIN photodiodes have an intrinsic layer of high resistivity sandwiched between the p-type and n-type layers, which increases the effective depletion layer. As the electron-hole pairs generated in the depletion layer have a much shorter transit time than those generated in the p-type or n-type regions, a faster device response is achieved than with an ordinary photodiode. Fig 3.15 shows the typical construction

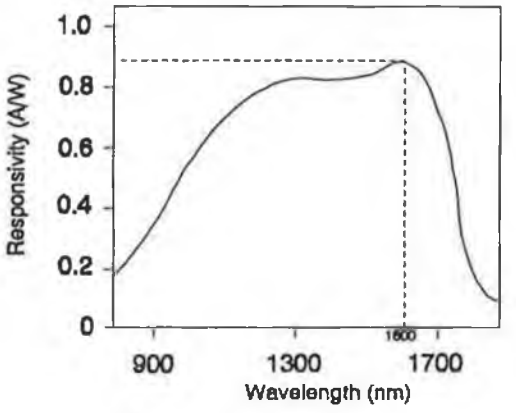

Fig 3.13 Detector Responsivity

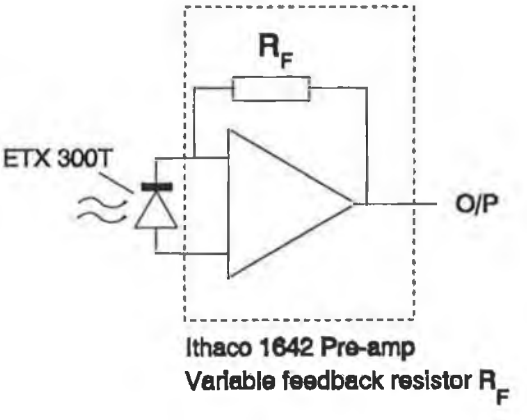

Fig 3.14 Detector and Pre-amplifier Circuit

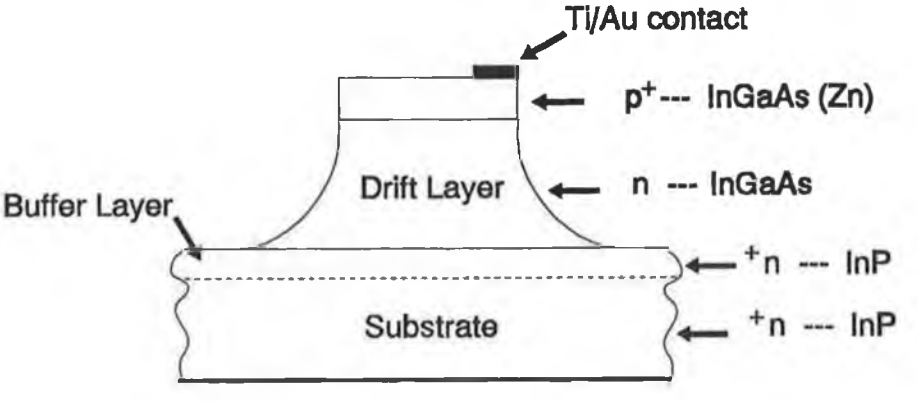

Fig 3.15 Cross-section through InGaAs Photodiode

of an InGaAs PIN photodiode [38].

3.4.2.2 Noise

Detector noise puts a limit on the minimum optical signal detectable by the system. There are two main types of photodetector noise. One is *shot noise* which is inherent in photodetectors and the other is *thermal noise* which arises in pre-amplifiers. Shot noise, also called optical or quantum noise, arises from the random distribution of the arrival of incident photons to the detector. As a result there is a random release of charges in the photodetector giving rise to a noise current. Thermal noise arises from random motion of electrons in a resistor. When photodiodes are operated in the photovoltaic mode as in this system thermal noise only arises from the feedback resistor in the pre-amplifier following the detector.

Shot Noise

The mean square shot noise current is given by [37],

$$\langle i_{sh}^2 \rangle = 2q \cdot \Delta f (I_{ph} + I_d) \quad (in\ Amps^2) \qquad \text{..... Eqn 3.12}$$

where, q is the electronic charge 1.6×10^{-19}C

I_{ph} is the photocurrent (A)

I_d is the dark current (A)

Δf is the effective noise bandwidth of the system (Hz)

This effective noise bandwidth is given by [41],

$$\Delta f = \frac{1}{4 R_F C_p}$$

where, R_F is the amplifier feedback resistance value (Ω)

C_p is the photodiode junction capacitance (F)

If no light falls on the detector then I_{ph}=0 and the shot noise arises only from the dark current.

Thermal Noise

Thermal noise current arises due to the feedback resistance R_F in the pre-amplifier. Its value is given by,

$$\langle i_{th}^2 \rangle = \left(\frac{4kT}{R_F}\right)\Delta f \quad (in\ Amps^2) \qquad \text{..... Eqn 3.13}$$

where k is the Boltzmann constant 1.38 x 10^{-23} J/K

T is the temperature of the electrons in the resistor R_F (K)

The total mean square noise current, *per unit bandwidth*, is equal to $\langle i_{th}^2 \rangle \div \Delta f$ added to $\langle i_{th}^2 \rangle \div \Delta f$ (Units in A^2/Hz). If the mean square value of the signal current (i.e. photocurrent only) is $\langle I_{ph}^2 \rangle$ then the signal to noise ratio at the amplifier output is,

$$SNR = \frac{\langle I_{ph}^2 \rangle}{2q(I_{ph}+I_d) + \frac{4kT}{R_F}} \qquad \text{..... Eqn 3.14}$$

where the SNR is given per unit bandwidth (Hz^{-1}) [41,42].

Noise Equivalent Power

This is defined as the radiant flux on the detector which produces an output signal equal in magnitude to that produced by the noise signal. This means that SNR=1 and therefore,

$$\langle I_{ph} \rangle = \sqrt{2q(I_{ph}+I_d) + \frac{4kT}{R_F}} \qquad (in\ A/Hz^{1/2})$$

The NEP is then calculated for the system (i.e. detector and pre-amplifier) using the responsivity value S_λ (in A/W) for the detector at a specific wavelength where,

$$NEP = \frac{\langle I_{ph} \rangle}{S_\lambda} = \frac{\sqrt{2q(I_{ph}+I_d) + \frac{4kT}{R_F}}}{S_\lambda} \quad \text{..... Eqn 3.15}$$

The NEP is given in watts per unit bandwidth ($W/Hz^{1/2}$).

The output from the Ithaco pre-amplifier at gain 10^8 for no detector signal (i.e. no photocurrent) is 3mV peak to peak or mean square voltage 2.25mV. This corresponds to a total mean square noise current $\langle i^2_{total} \rangle$ of 22.5pA (arising from the dark and the thermal noise currents over the pre-amplifier bandwidth). For unit noise bandwidth, $\langle i^2_{total} \rangle$ is divided by the systems effective noise bandwidth Δf. This was taken as the bandwidth of the pre-amplifier which was measured to be 15.3 KHz at gain 10^8 V/A. The square root of this value is $\langle i_{total} \rangle$ and dividing it by the responsivity S_λ yields the NEP for the detection system.

$$NEP = \frac{\langle i_{total} \rangle}{S_\lambda} = \frac{3.83\times10^{-6}}{0.85_{\lambda=1.66\mu m}} = 45\times10^{-9}\ W\ Hz^{1/2}$$

There was no noticeable change in output noise levels upon detection of infra-red signals (i.e. when the photocurrent $\neq 0$) from d.c. up to 80 Hz, this frequency being determined by the filter wheels rotation speed. Therefore, for operation at 80 Hz, the approximate value for the minimum detectable power by the system at a pre-amplifier gain of 10^8 V/A, a wavelength of 1.66μm, unit noise bandwidth, is 45×10^{-9} $W/Hz^{1/2}$. Using a typical signal of 1V with a 3mV noise signal at a 10^8 gain setting, the signal to noise ratio is approximately 300 to 1. Therefore, the electronic noise contribution to detected signals is very small.

3.4.3 Filter Wheel

A modified Scitec Instruments optical chopper system is used to synchronously detect both the two interference filter signals. The filters are fitted diagonally opposite each other on a custom made filter wheel as shown in Fig 3.16. Four slots were cut out along the wheel periphery. The end points of two of these slots are radially aligned to the centres of the interference filters. The end points of the other slots are radially aligned to the remaining opaque areas on the wheel. These

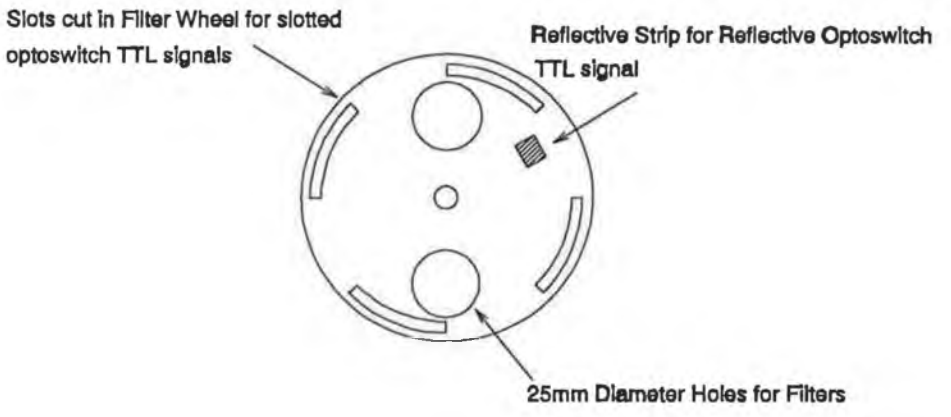

Fig 3.16 Filter Wheel

areas serve in the detection of background light which is then subtracted from the filter signals. As the detector response falls off quickly below 900nm, the background signal is generally zero. The optical chopper slotted opto-switch outputs a TTL pulse train. TTL low is output when a slot passes the opto-switch and vice versa. The rising edge (i.e. low to high) on a pulse corresponds to either a filter or an opaque region which is in position for signal detection.

A reflective opto-switch is used to synchronise the correct sequential detection of the four signals for every rotation of the wheel. A small reflective strip was affixed to the wheel. The opto-switch output is TTL high. When the strip passes in front of it the output goes low. This falling edge provides the synchronisation pulse as can be seen in Fig 3.17.

3.4.4 Data Detection

A Bytronic MPIBM3 multi-function interface card is used both for the detection of control line pulses from the filter wheel opto-switches and for the analogue to digital conversion of the filter signals from the detector/pre-amplifier assembly.

The interface card has an ADS574 12 bit, 0 to 10 volts analogue to digital conversion chip which contains an internal sample and hold unit. The maximum time for a 12 bit conversion (including the acquisition time) is 25μs. Therefore no problems with detection speed arise as only 80 data signals are measured every

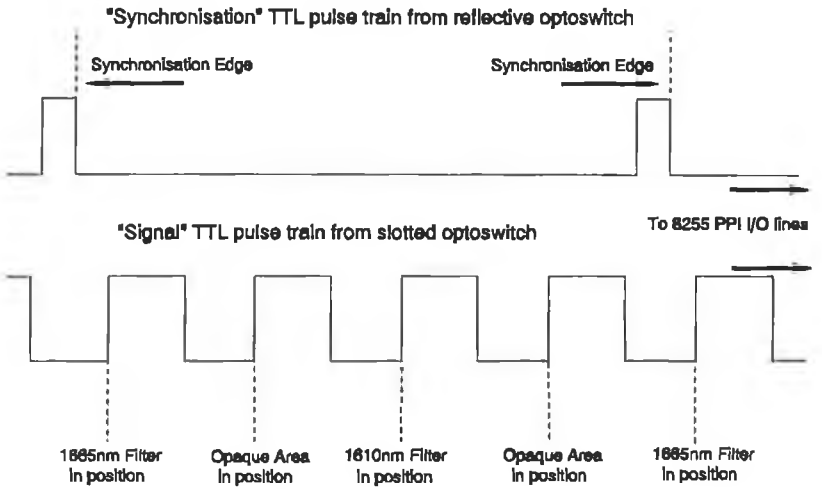

Fig 3.17 Electronic Timing Diagram

second by the system. The board also has an 8255 Programmable Peripheral Interface (PPI). This has 24 digital lines which can be programmed to be input or output ports. For the system, two of these are programmed as input lines and are connected to the control lines from the filter wheel via transistor buffering circuitry. This intermediate circuitry, shown in Fig 3.12, ensures that both the PPI lines see only TTL high or low signals such that their state is not ambiguous.

Analogue to digital conversion of a signal is initiated by software when the PPI "signal" line changes from a high to a low state (i.e. TTL high to TTL low). The PPI "synchronisation" line for correct sequential signal detection, changes from a low to a high state when the reflective strip on the filter passes the opto-switch. The software controlling data acquisition and processing was written in Turbo C.

The data acquisition sequence for one set of the four signals is as follows:

i) When the reflective strip passes the opto-switch on the rotating filter wheel, a pulse (TTL low to high) is obtained on the PPI "synchronisation" control line.

ii) A pulse (TTL high to low) is then obtained on the PPI "signal" control line from the slotted opto-switch on the rotating filter, indicating that the 1665nm "on" absorption filter is in position between the fiberised GRIN lenses and therefore in position for detection.

iii) The sample and hold unit is activated and followed by analogue to digital

conversion of the signal. The resultant 12 bit binary number is read by the computer and stored in an array. The software waits for the PPI "signal" control line to go high again.

iv) As the filter wheel rotates step ii) is repeated, indicating that an opaque part of the wheel is in position for background light detection. Step iii) takes place.

v) Step iv) is repeated for the 1610nm "off" absorption filter and again for the second background signal.

3.4.5 Data Processing

A flowchart of the program Sense1 is shown in Fig 3.18. For each main loop reading R (where R=1 for 100%N_2 and 0% CH_4, R=2 for 1% CH_4 etc.), the data acquisition process outlined in section 3.4.4, is repeated 200 times to get a more accurate indication of the correct signal values.

The true "on" and "off" absorption values, $I_{\lambda on}$ and $I_{\lambda off}$ respectively, are calculated for each set of four signals of the 200 scans, by subtracting the background signals from the filter signals. An average value for $(I_{\lambda off}/I_{\lambda on})$ is then obtained for all but the zero concentration reading, R=1. In this case both the average $(I_{0\lambda on}/I_{0\lambda off})$ and the average $(I_{0\lambda off}/I_{0\lambda on})$ are evaluated. The latter is evaluated for the purpose of standard error determination.

From section 3.2 on the Beer-Lambert Law, the quantity which must be obtained by the software for each concentration value c, is

$$\ln\left(\frac{I_{0\,\lambda on}}{I_{0\,\lambda off}} \cdot \frac{I_{\lambda off}}{I_{\lambda on}}\right)$$

The standard errors on $(I_{0\lambda on}/I_{0\lambda off})$ and $(I_{0\lambda off}/I_{0\lambda on})$, and $(I_{\lambda off}/I_{\lambda on})$ are calculated by the software as follows:

Firstly, the standard deviation s, is calculated on $(I_{0\lambda on}/I_{0\lambda off})$, $(I_{0\lambda off}/I_{0\lambda on})$ and on $(I_{\lambda off}/I_{\lambda on})$ where,

$$s = \sqrt{\left[\frac{\sum x^2}{N} - (\bar{x})^2\right]} \qquad \text{..... Eqn 3.16}$$

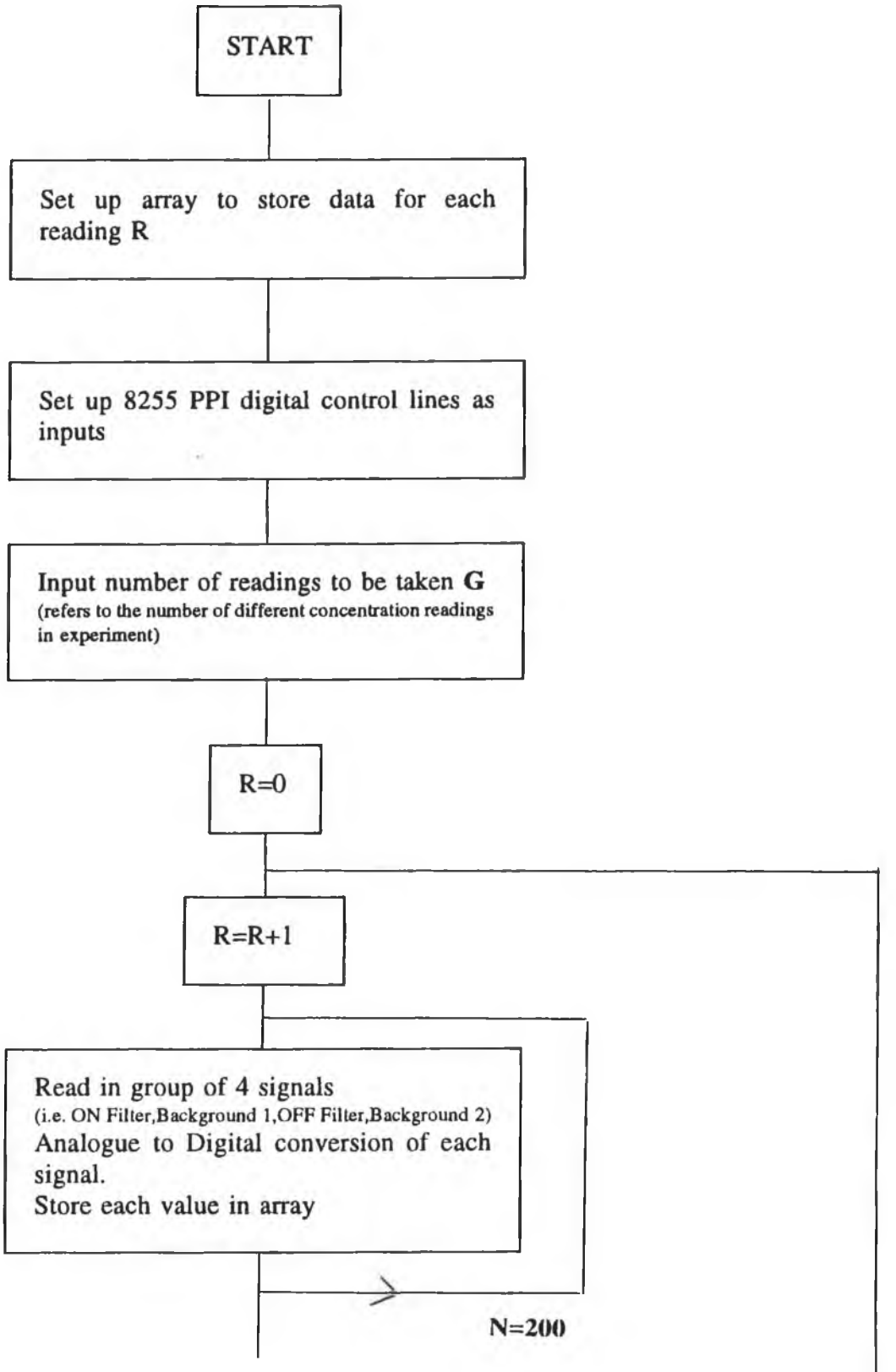

Fig 3.18 Flowchart for Sense1

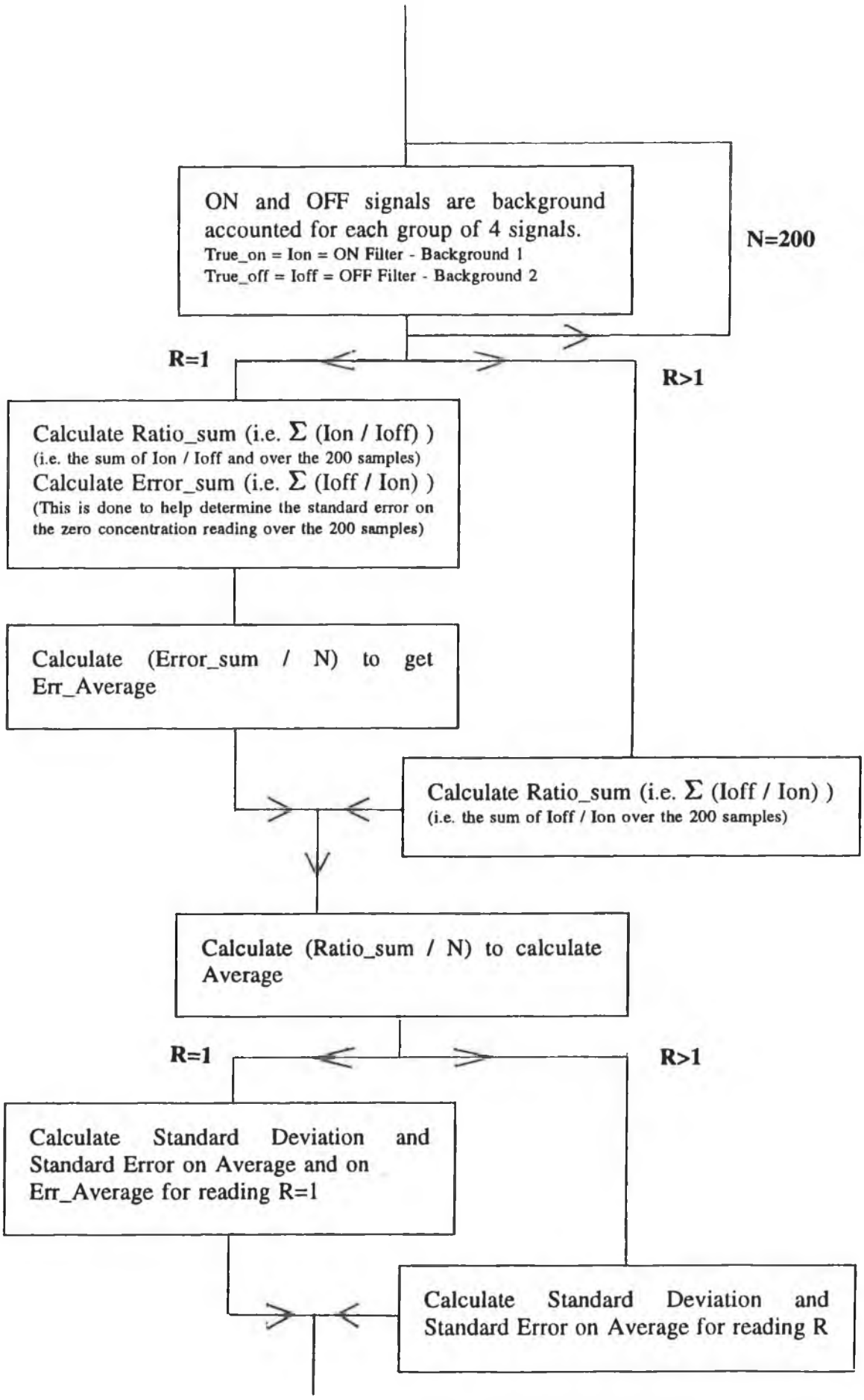

Fig 3.18 (continued) Flowchart for Sense1

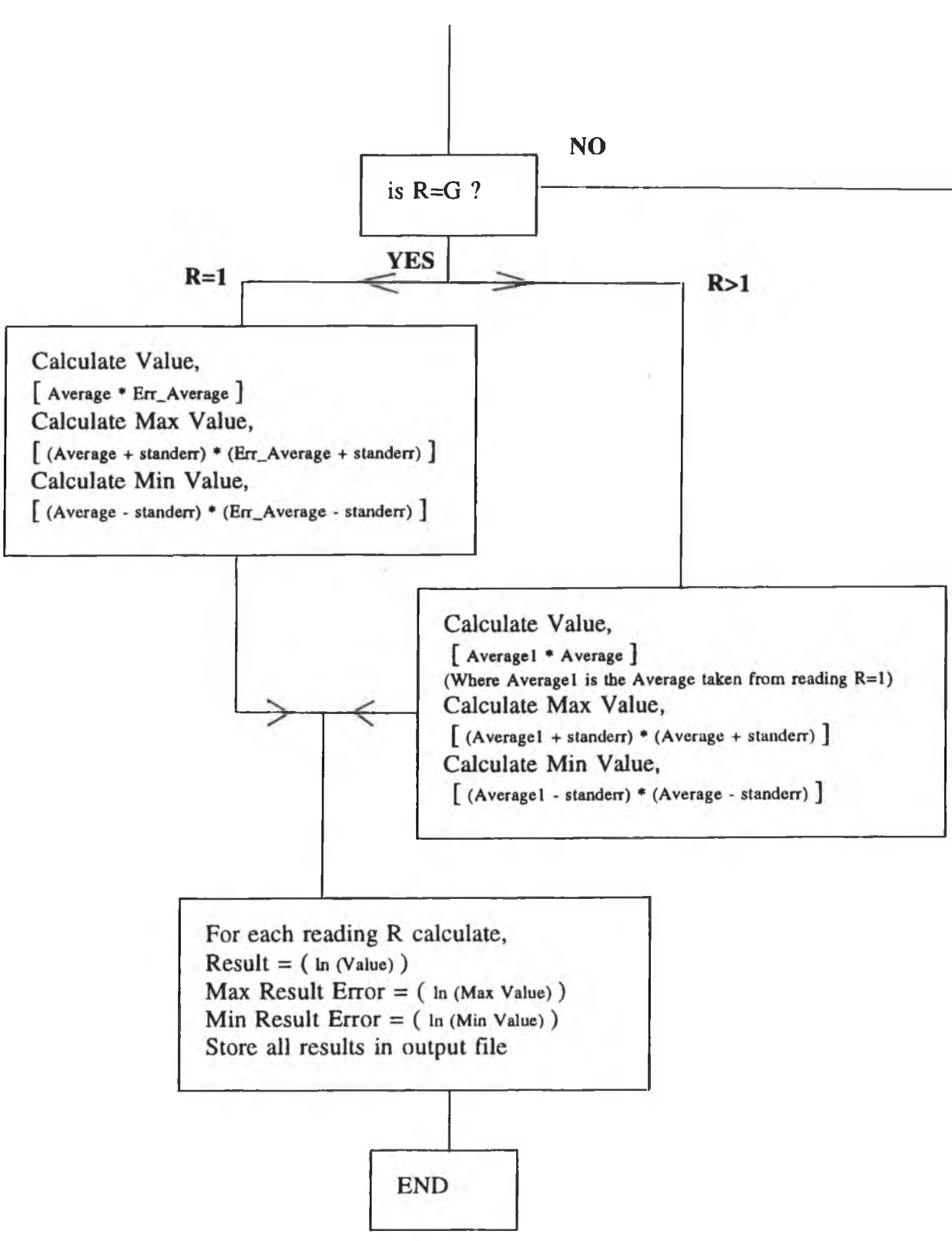

Fig 3.18 (continued) Flowchart for Sense1

x is the measurand ($I_{0\lambda on}/I_{0\lambda off}$), ($I_{0\lambda off}/I_{0\lambda on}$) or ($I_{\lambda off}/I_{\lambda on}$) depending on the loop reading R. N is the number of samples, in this case 200, used to calculate the average value of x, and $\bar{x}$ is the average value of the measurand.

The standard error, S.E, for x is then calculated from,

$$S.E = \frac{s}{\sqrt{N}} \qquad \text{..... Eqn 3.17}$$

$\ln\left(\frac{I_{0\,\lambda on}}{I_{0\,\lambda off}} \cdot \frac{I_{\lambda off}}{I_{\lambda on}}\right)$ is then evaluated for each reading R and maximum and minimum values also determined using the standard errors.

3.5 Conclusion

A fibre optic remote methane sensing system for methane was designed and constructed. Methane in the gas cell absorbs infra-red light according to the Beer-Lambert Law. The optical and electronic components of the system were characterised. The minimum power detectable by the system at 1.66μm, for unit noise bandwidth and an amplifier gain of 10^6 was evaluated to be $45 \times 10^{-9} W/Hz^{1/2}$ and a typical signal to noise ratio for the system is 300 to 1. Software was written to acquire and process data and to calculate standard errors on each reading.

Chapter 4

System Optimization

4.1 Introduction

In this chapter the design changes made to optimize the fibre optic gas sensing system presented in Chapter 3 are outlined. The need for these changes, their implementation and the resulting benefits to the systems overall performance are discussed.

The system was initially designed to employ multimode fibre and to use a multimode variant of the LED source described in section 3.3.1. This device offered high coupled power into multimode fibre, but a detailed characterisation revealed that it did not provide adequate performance for the system requirements. Consequently the system design was changed to that in Chapter 3, with the use of the single mode fibre pigtailed device. This resulted in a severe decrease in the system power levels and subsequent experimental work with the sensor revealed poor sensitivity and resolution at low concentrations. A more comprehensive discussion on both of the LED sources follows in section 4.2.

High resolution absorption spectra of methane were obtained on an FTIR to identify the optimum "on" resonance filter in order to increase the system sensitivity. After studying the spectra a new "on" resonance filter with a peak transmittance at 1.666μm and bandwidth of 2nm was purchased. Subsequent work with this filter showed a factor of six improvement in system sensitivity over that achieved with the 1665nm filter. The experimental work concerning the new filter is outlined in section 4.3.1.

Other improvements in the overall system design were, firstly, the optimization of the coupled retroreflected power into port 3 of the fibre optic coupler and, secondly, the control of the LED's temperature and power output. These improvements, achieved by altering the gas cell collimating optics and adding a thermoelectric cooler to the LED, are outlined in section 4.3.2 and section 4.3.3, respectively.

4.2 LED Sources

One of the key features in the initial design of this system was the use of a

novel edge-emitting, super-luminescent LED (ELED) (model LD3207) which is manufactured by GEC Marconi Materials Technology Ltd., Caswell, U.K.. Super-luminescent devices have a super linear increase in output power with elevated drive currents. The device has only been commercially available since 1992.

4.2.1 Multimode LED Variants

Initially two multimode variants of the LED were purchased. Each consists of the basic LED structure as detailed in section 3.3.1, which is then connected to a small length of multimode fibre pigtailed to the emitting area of the LED. The LED/fibre assembly is packaged with an FC/PC type fibre optic adapter for direct connection to multimode fibre. A connectorised approach into multimode fibres was chosen to avoid bulky alignment optics and to maximise system throughput. Both LEDs offered approximately 500μW of coupled power into 50/125 multimode fibre, at a drive current of 150mA. A detailed characterisation of both devices was undertaken. Spectral outputs were obtained using a SPEX 1704, 1m focal length, Czerny Turner spectrometer, with a liquid nitrogen cooled germanium detector.

The spectral outputs from both devices in the absence of optical fibres, are shown in Figs 4.1a and 4.1b. They exhibit the standard spontaneous emission characteristics associated with LEDs, both peaking at 1625nm with a bandwidth of approximately 60nm. The LED drive current was 100mA in each case.

The LEDs were then connected in turn to a five metre long, 50/125μm, multimode fibre. The spectral profiles from the fibre end were determined in each case and are shown in Figs 4.2a and 4.2b. As can be seen, the smooth LED spectral structure obtained in the absence of fibre has been replaced by irregular peaks and troughs over the emission spectral range. Spectra at lower drive currents were then obtained. Figs 4.3a and 4.3b are spectra taken for each device at 80mA. Although the structures in both cases are similar to those obtained at 100mA, the relative intensity difference between peaks is not constant. One explanation for the observed spectral features is the existence of "modal noise" in the fibre. Modal noise is characteristic of multimode fibre transmission and is due to intermodal interference of light along the fibre length. This interference becomes more significant, the higher the degree of coherence of the light source. As a result, a time-varying speckle pattern exists

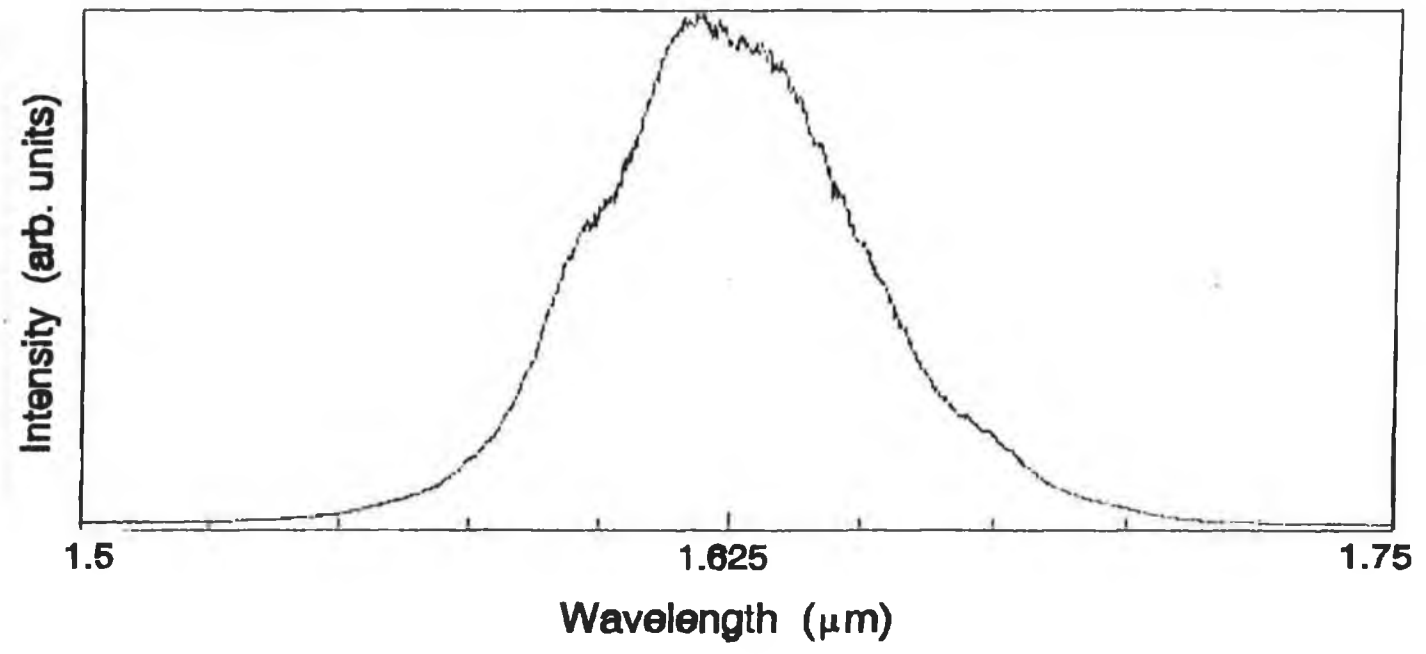

(a)

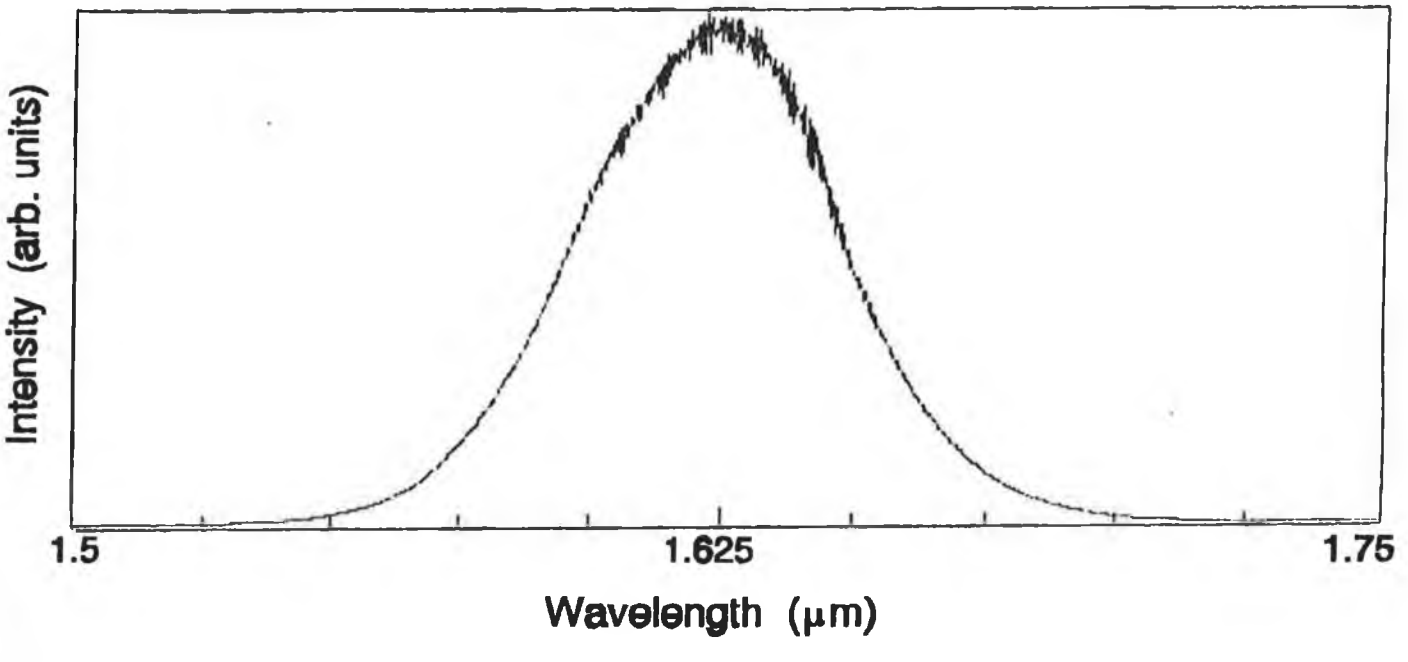

(b)

Fig 4.1 Spectra of Multimode LEDs (No Fibre)

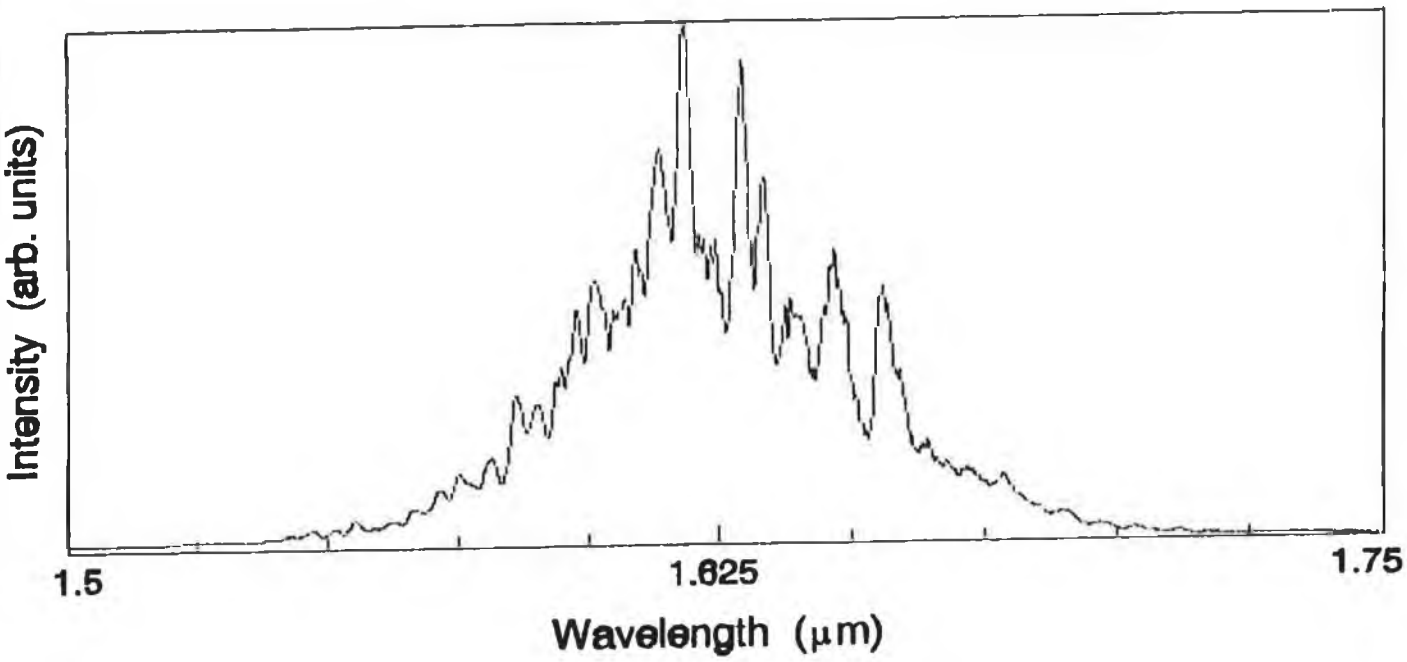

(a)

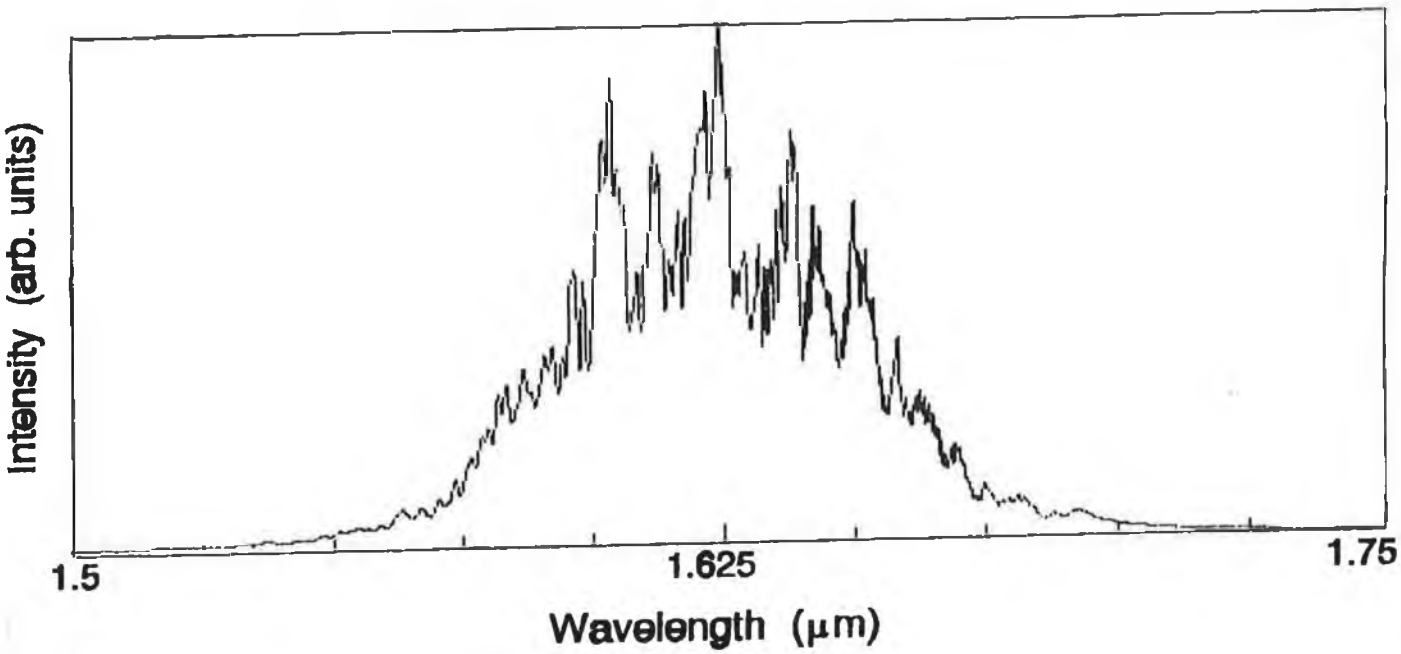

(b)

Fig 4.2 Spectra of Multimode LEDs with Multimode Fibre

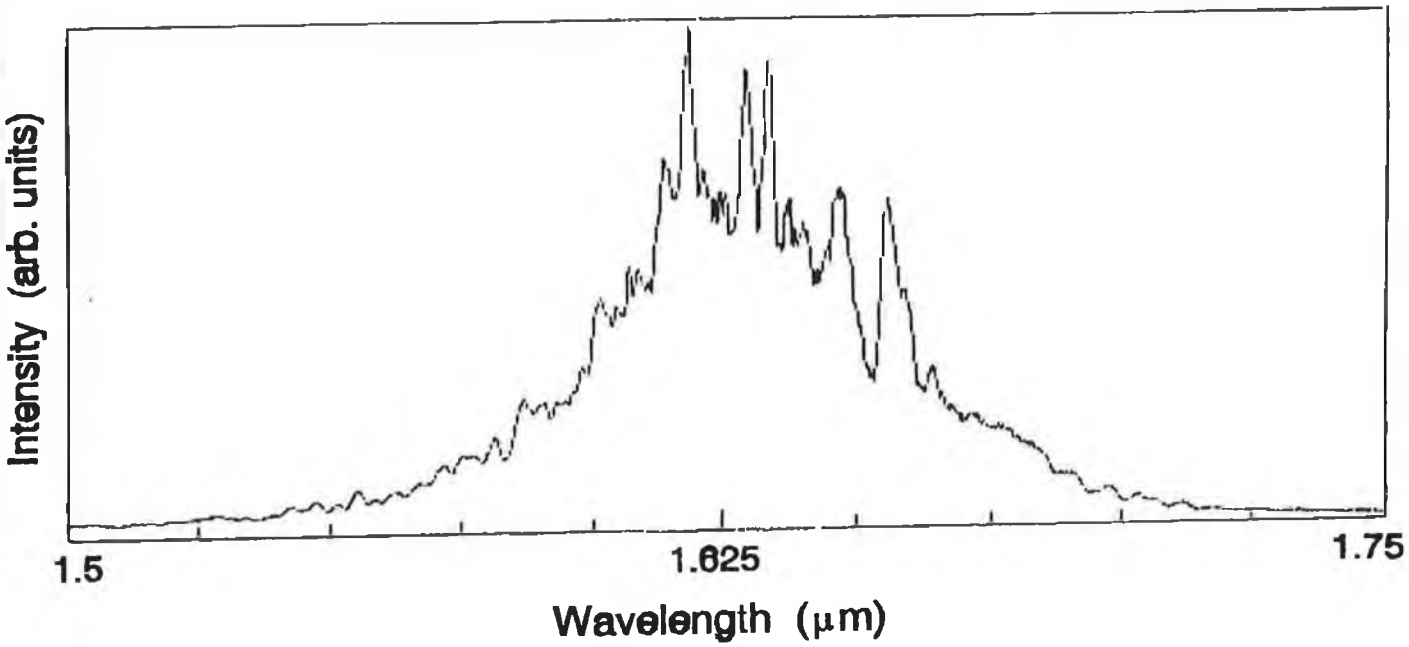

(a)

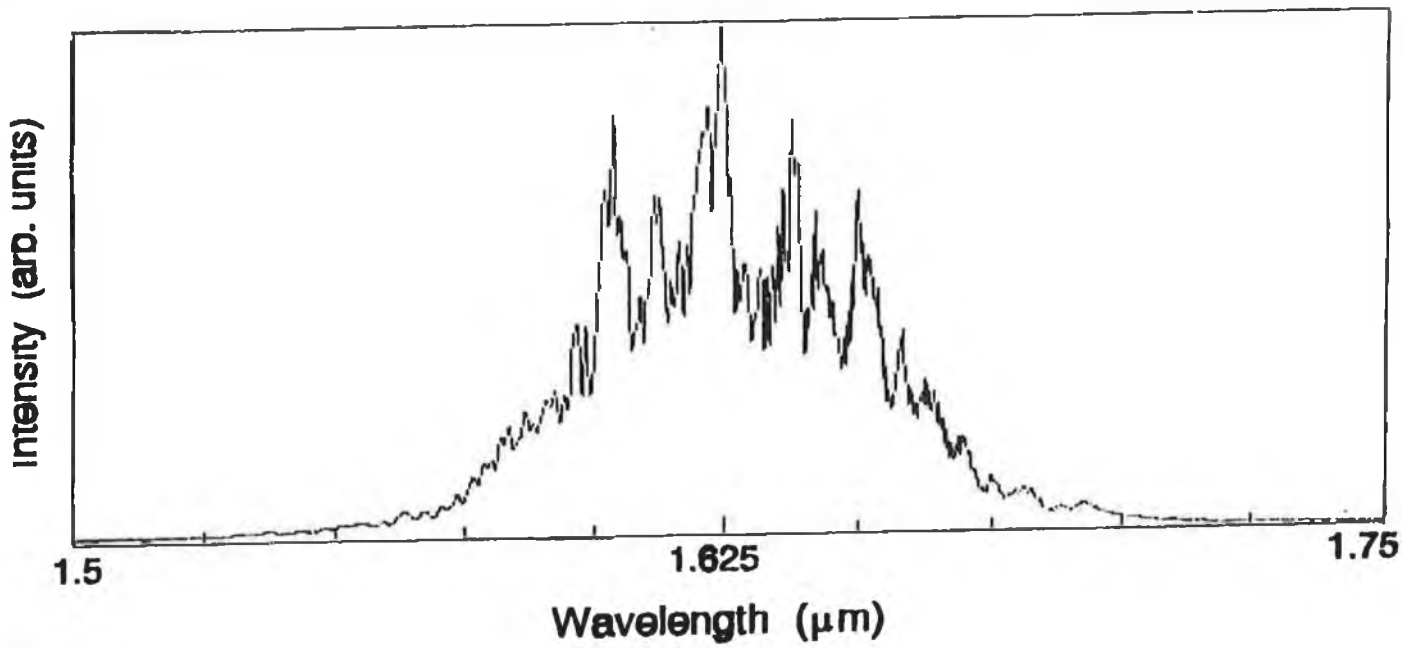

(b)

Fig 4.3 Spectra of Multimode LEDs with Multimode Fibre at 80mA

across the end face of the fibre. If there is a separation between two fibres, A and B, the power launched into fibre B will vary as the speckle pattern at the end face of fibre A varies. This effect, shown in Fig 4.4 [43], is particularly relevant to the configuration of the system presented in this work, as the short section of fibre within the packaged LED and the mechanically connected 5m long transmission fibre, represent fibres A and B in Fig 4.4, respectively.

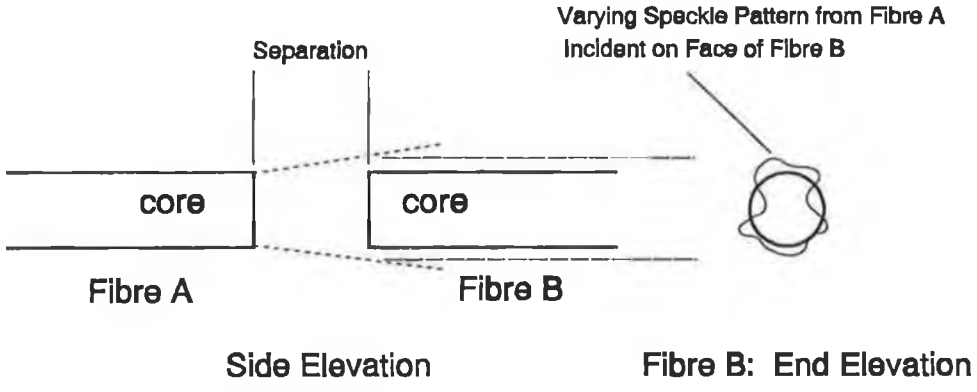

Fig 4.4 Modal Noise produced by varying Speckle pattern

The LEDs were then connected in turn to 9/125μm single mode fibre. As there is only one mode in single mode fibre, modal noise cannot occur. The spectral profiles from the fibre end were obtained in each case. The spectra, shown in Figs 4.5a and 4.5b, are quite dissimilar. Fig 4.5a shows an LED type output with a periodic intensity fluctuation over the output spectral range at wavelengths greater than the peak wavelength, while the structure in Fig 4.5b, although showing similar weaker features, has a secondary peak. The structure in Fig 4.5a suggests a Fabry-Perot interference type effect occurring at the interface between the segment of multimode fibre within the LED and the single mode fibre. This effect could be due to an air gap between both fibres. This possibility is reinforced by the spectrum shown in Fig 4.6, which was taken when the fibre was partially unscrewed from the FC fibre adapter of the LED. This spectrum also exhibits the periodic variation in intensity as in Fig 4.5a, but this time it occurs over the full spectral emission of the LED. This in turn strengthens the argument that modal noise is occurring as a result of a

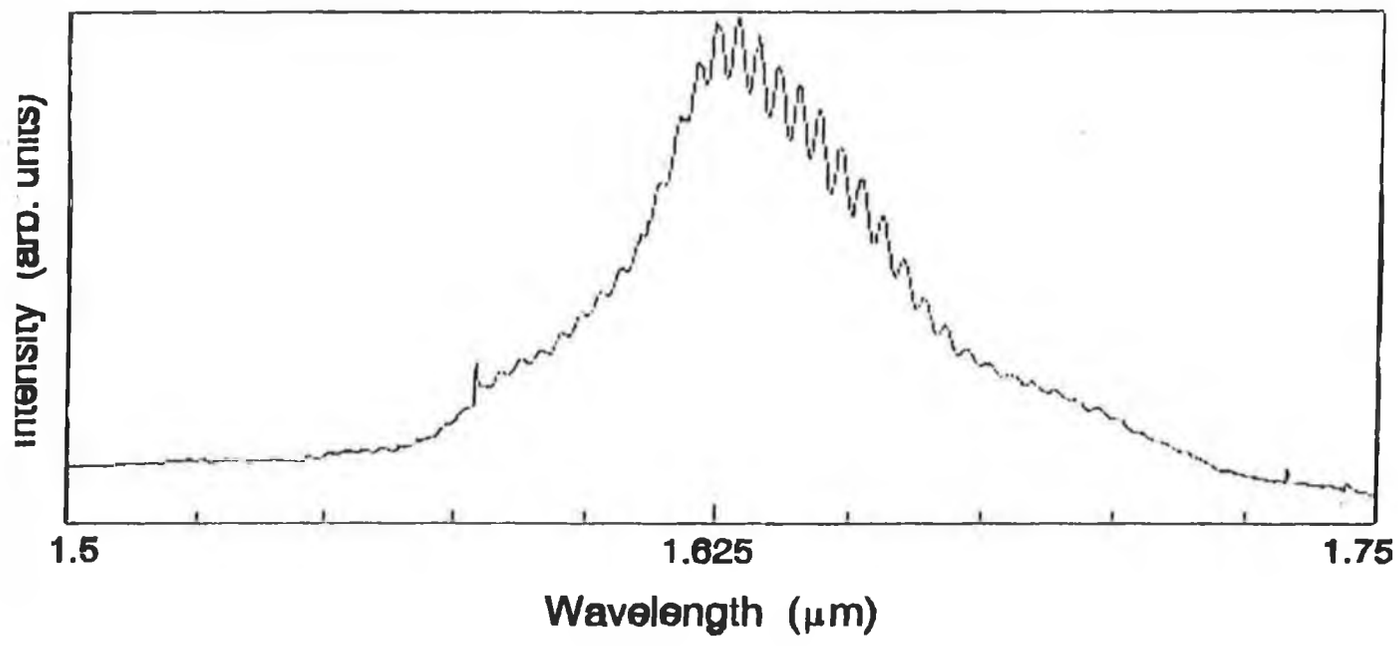

(a)

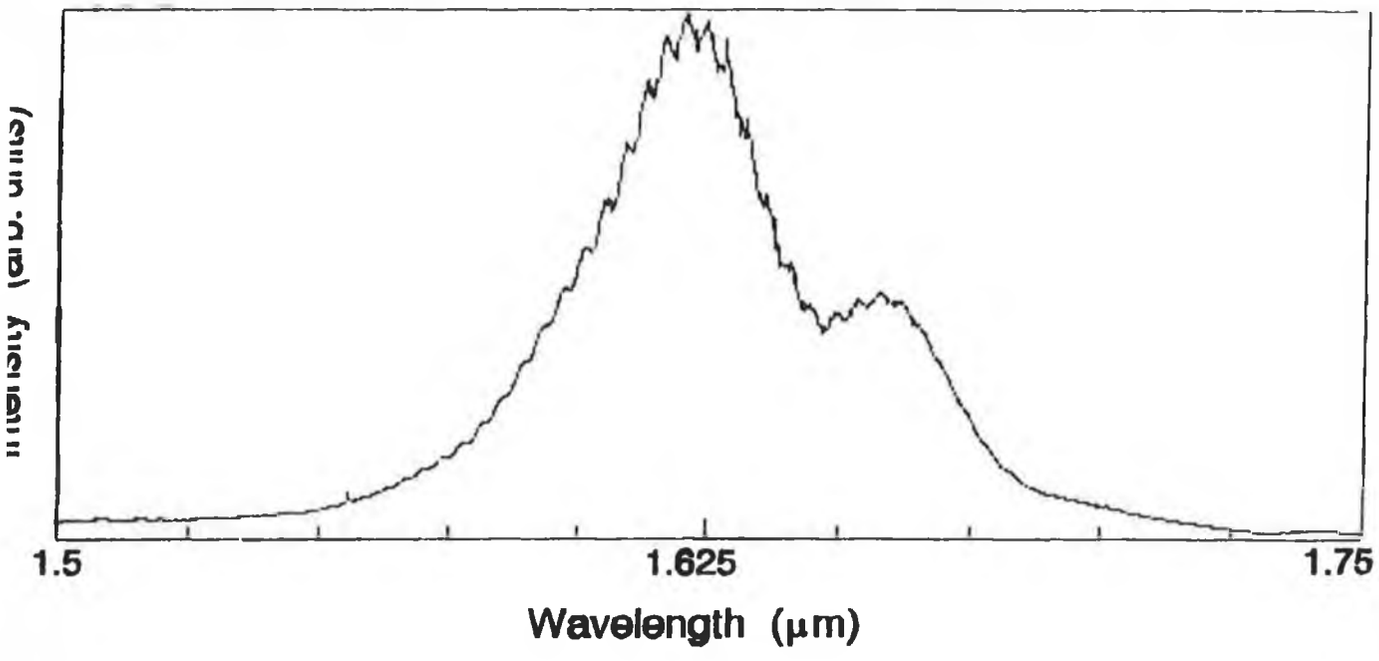

(b)

Fig 4.5 Spectra of Multimode LEDs with Single mode Fibre

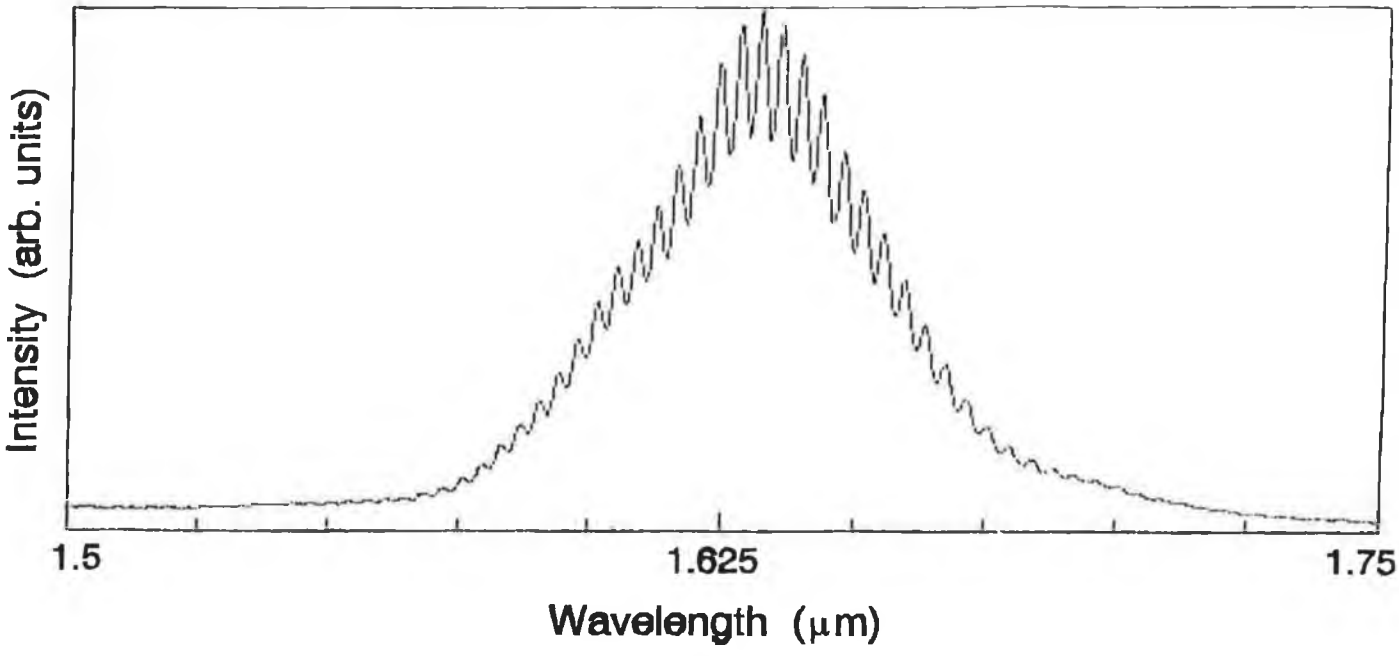

Fig 4.6 Spectrum of Multimode LED partially screwed to Single mode Fibre

separation between both fibres as discussed previously.

The analysis of the LEDs performance outlined in the preceding paragraphs suggests that both modal noise and a Fabry-Perot interference type effect occur when the LEDs are connected to multimode fibre. The devices were returned to the manufacturers with a report on their performance. They confirmed the results with experimental work of their own and suggested that the spectral outputs from the multimode fibre were due to modal noise effects. Consequently, both devices were unsuitable as sources for the system in the form acquired.

4.2.2 Single mode LED Source

Clearly a new source design was required in order to overcome the spectral effects outlined above. Although a pigtailed multimode device would not suffer from the Fabry-Perot interference type effect, it would be susceptible to the modal noise effect. Therefore, the use of multimode fibre in the system was abandoned and a single mode pigtailed variant of the LD3207 LED was purchased. Although this resulted in a severe decrease in coupled source power, the device still couples more power into single mode fibre than any other device of its type currently available,

(50μW at 100mA drive current) [44]. The spectral output of this LED, at a driving current of 100mA is shown in Fig 3.2.

The LED operates in super-luminescent mode (i.e. a super linear increase in output power with increasing driving current) at driving currents above 100mA. This is shown in Fig 4.7 where the power output of the fibre optic coupler used in the system is plotted against the LED drive current. Furthermore, less power is coupled into the single mode fibre as the temperature increases as shown in Fig 4.8. The power was measured using a model 33XLC power meter manufactured by 3M Photodyne, California, U.S.A.. The meter uses a germanium detector which was calibrated at 1.63μm (the peak emission of the LED).

A bench top monochromator system was developed to determine the spectral characteristics of the LED. A 10cm "Minichrom" monochromator, manufactured by Optometrics Ltd., Leeds, U.K., was obtained. The monochromator is small in size (approximately 100 x 60 x 50 mm), has a spectral range between 1μm and 4μm, and has a resolution of between 5nm and 10nm depending on the entrance and exit slit widths. The slits used were 300μm wide yielding a resolution of approximately 5nm. The grating is blazed at 2μm and the interval wavelength step achieved by the stepper motor is 1.5nm. Analogue and digital electronics were designed and constructed for the stepper motor as shown in Fig 4.9. Software was written in Turbo C to control the stepper motor movement, and to collect and store data for each 1.5nm interval step. A flowchart of the software programme, called Mono1, is shown in Fig 4.10.

Fig 4.11 shows spectra recorded with the monochromator system for a range of LED drive currents. These spectra show the onset of lasing action in the active region of the LED above a driving current of 100mA (i.e. where super-luminescence occurs). The increase in power at the two wavelengths of interest, namely 1610nm and 1666nm, is minimal at these elevated driving currents. Consequently, 100mA was chosen as the optimum drive current for the device in this sensing system.

4.3 Optimization of system components

Three further changes were made to the system in order to improve its performance. The most important of these was the replacement of the 1665nm "on"

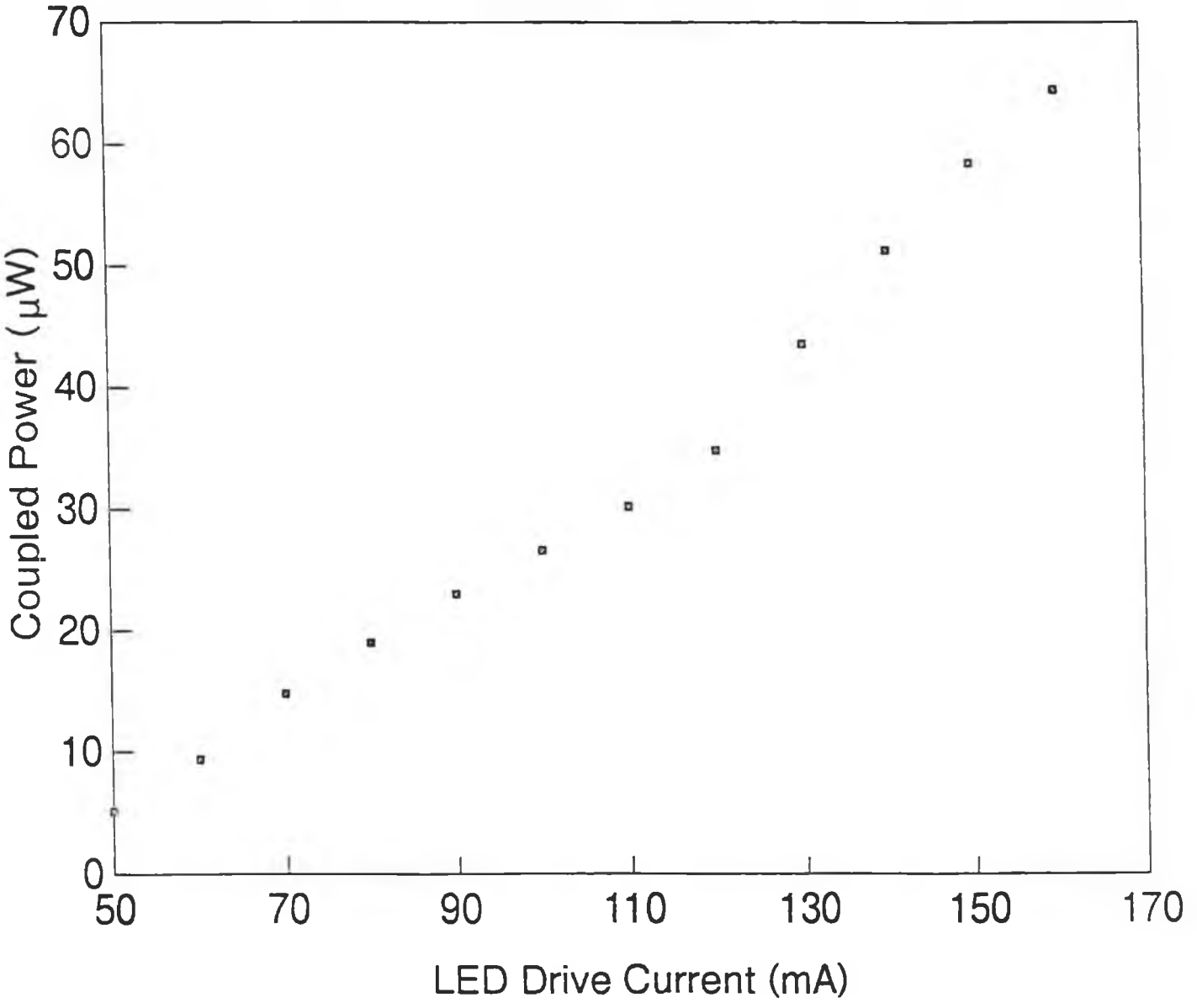

Fig 4.7 LED Super-luminescent Mode

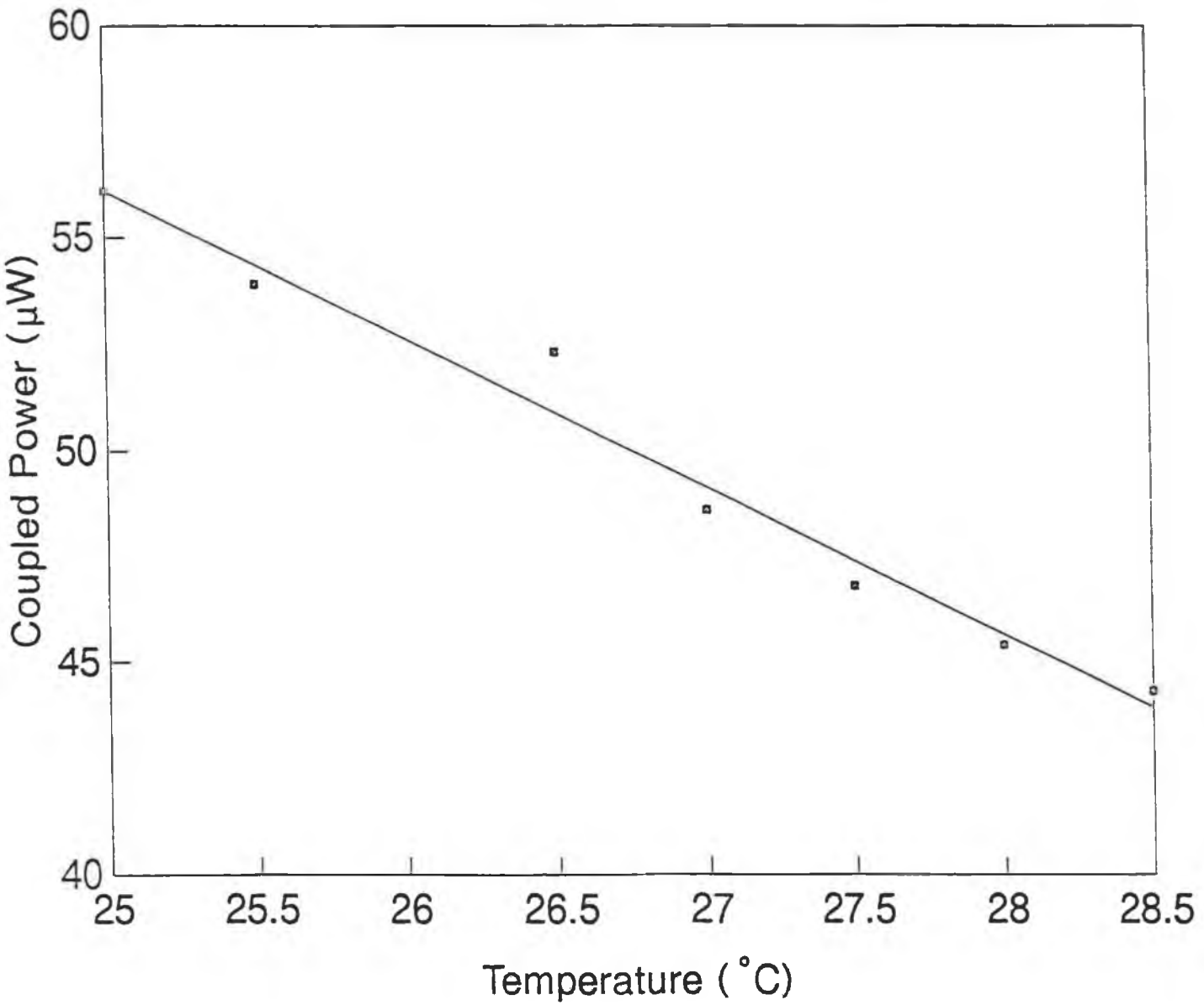

Fig 4.8 Coupled Power versus Temperature

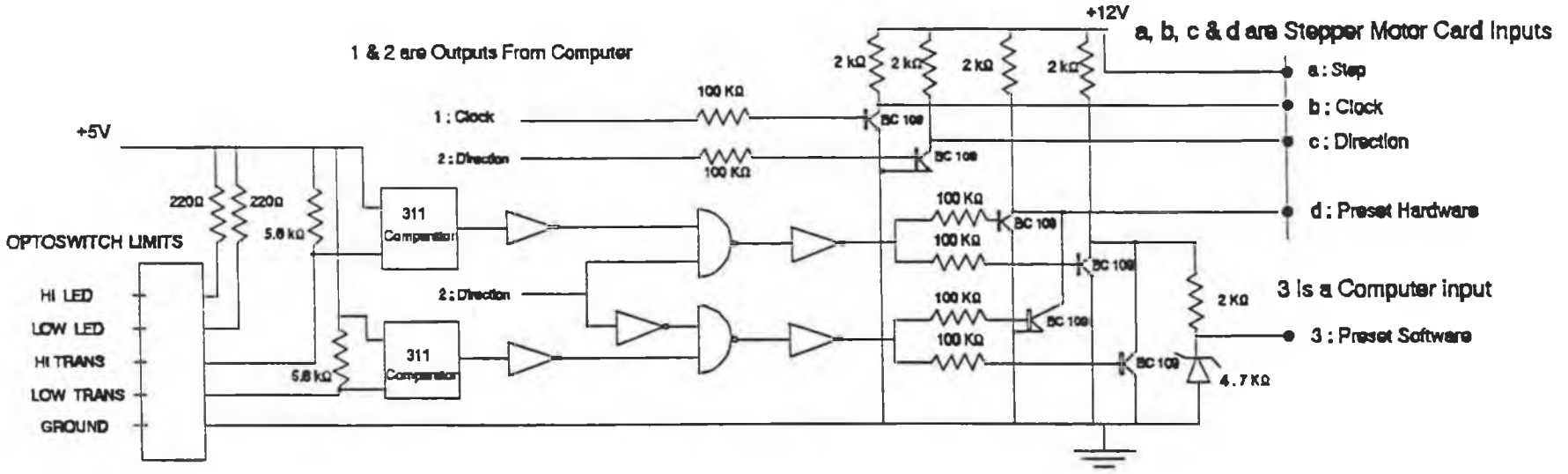

Fig 4.9 Stepper Motor/Monochromator Electronics

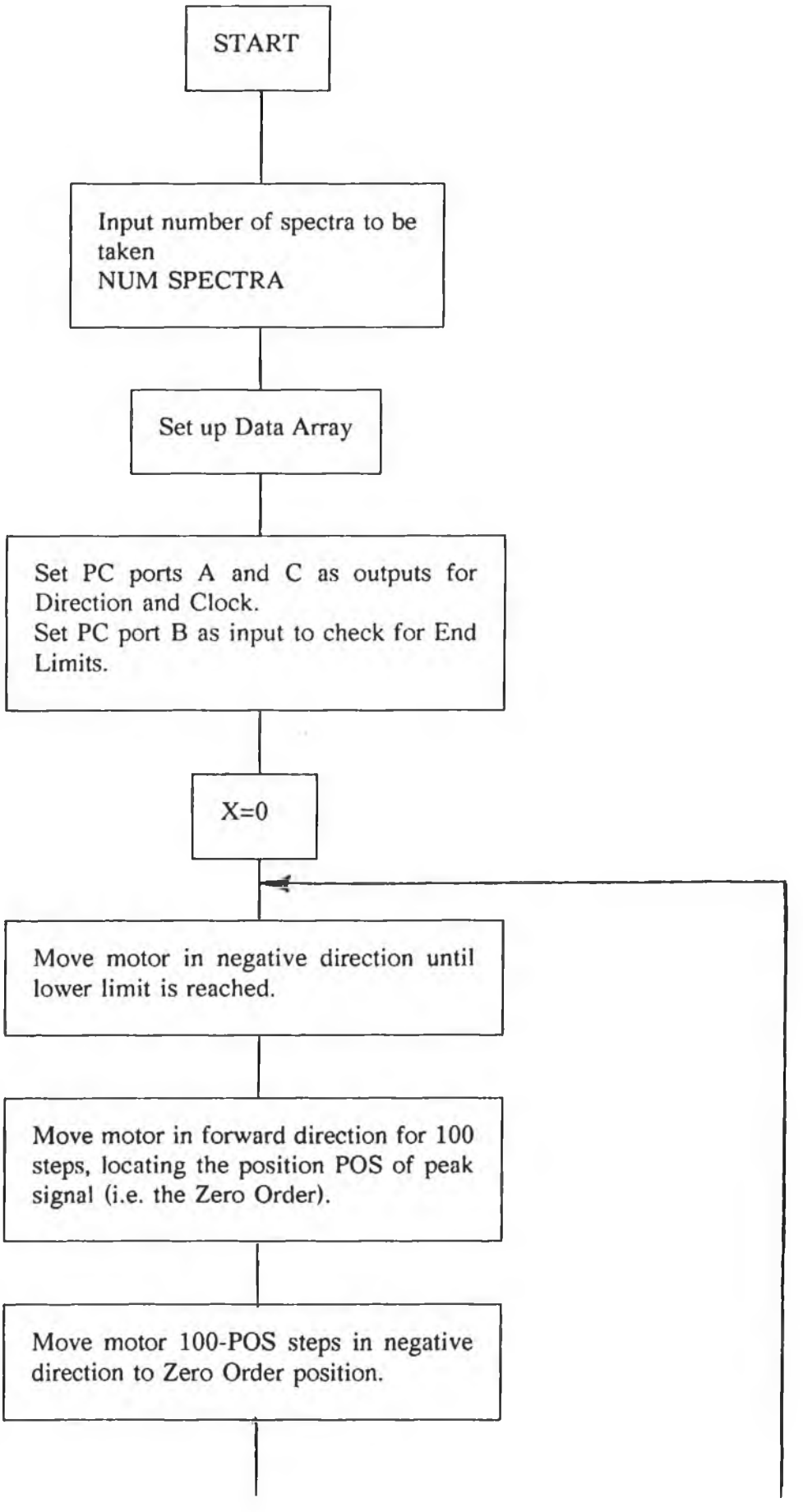

Fig 4.10 Flowchart for Mono1

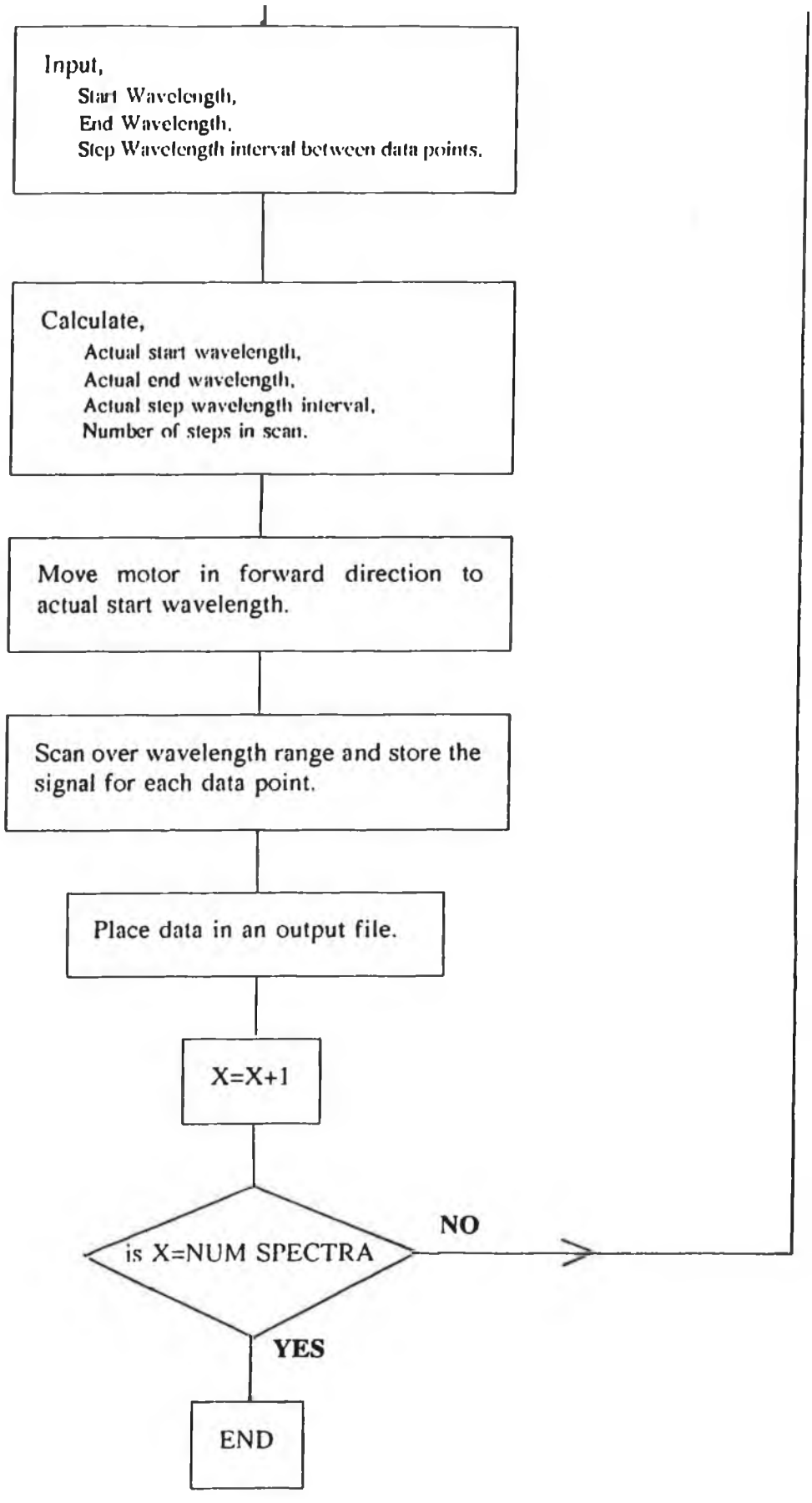

Fig 4.10 (cont'd) Flowchart for Mono1

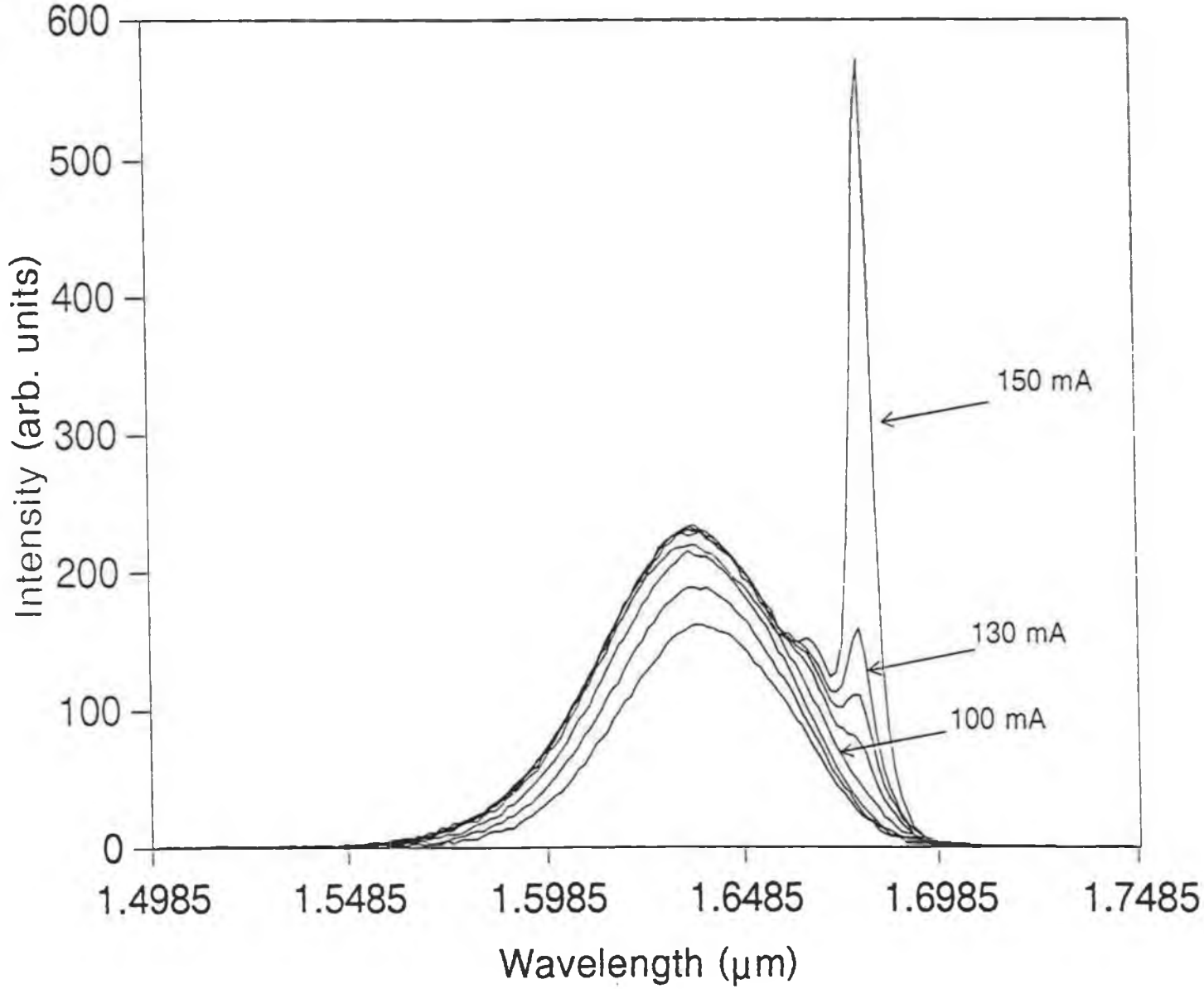

Fig 4.11 LED Spectra for Various Drive Currents

resonance interference filter with one having a peak transmission at 1666nm. Secondly, the 60mm focal length collimating lens was replaced by a microscope objective of numerical aperture 0.25 and thirdly, circuitry to thermoelectrically cool the LED was constructed and added to the system.

4.3.1 1666nm Interference Filter

The most important components in determining the overall sensitivity of the system are the LED source and the "on" absorption interference filter. The LED determines the power in the system, while the spectral characteristics of the "on" resonance interference filter determine the measured relative degree of absorption . As the single mode LED source couples only 50μW of power into the system, a factor of ten less than that offered by the multimode variants, the choice of the interference filter was critical to optimize system sensitivity.

The filter used in the initial system design had a peak transmission of 61% at 1665nm (coinciding closely with the reported Q-branch peak absorption wavelength of 1665.4nm [13]) and a bandwidth of 2nm. However, experimental work revealed a reduction of only 4% in the signal transmitted through the filter when a concentration of 5% methane was introduced to the gas cell. As 5% is the lower explosion limit of methane and therefore effectively the upper range limit required on the sensor calibration curve, this small signal reduction signified poor system sensitivity.

In order to determine the optimum filter transmission characteristics, a high resolution absorption spectrum of methane in the 1.66μm spectral region was recorded using a Bomem DA8 Fourier Transform infra-red spectrometer (FTIR), with a liquid nitrogen cooled Indium Antimonide (InSb) detector. The gas cell path length was 10cm and the gas concentration was 100% methane. The resolution of the spectrum, which is shown in Fig 4.12, is $0.1cm^{-1}$. The spectrum indicates that the absorption peak in the Q-branch is at 1665.6nm but more importantly that the Q-branch absorption is asymmetric about this peak. The Q-branch exists between 1664.5nm and 1669nm approximately. Therefore, the original "on" absorption interference filter, with a peak transmission at 1665nm and a bandwidth of 2nm only partly transmits light at the peak absorption wavelength and also transmits non-

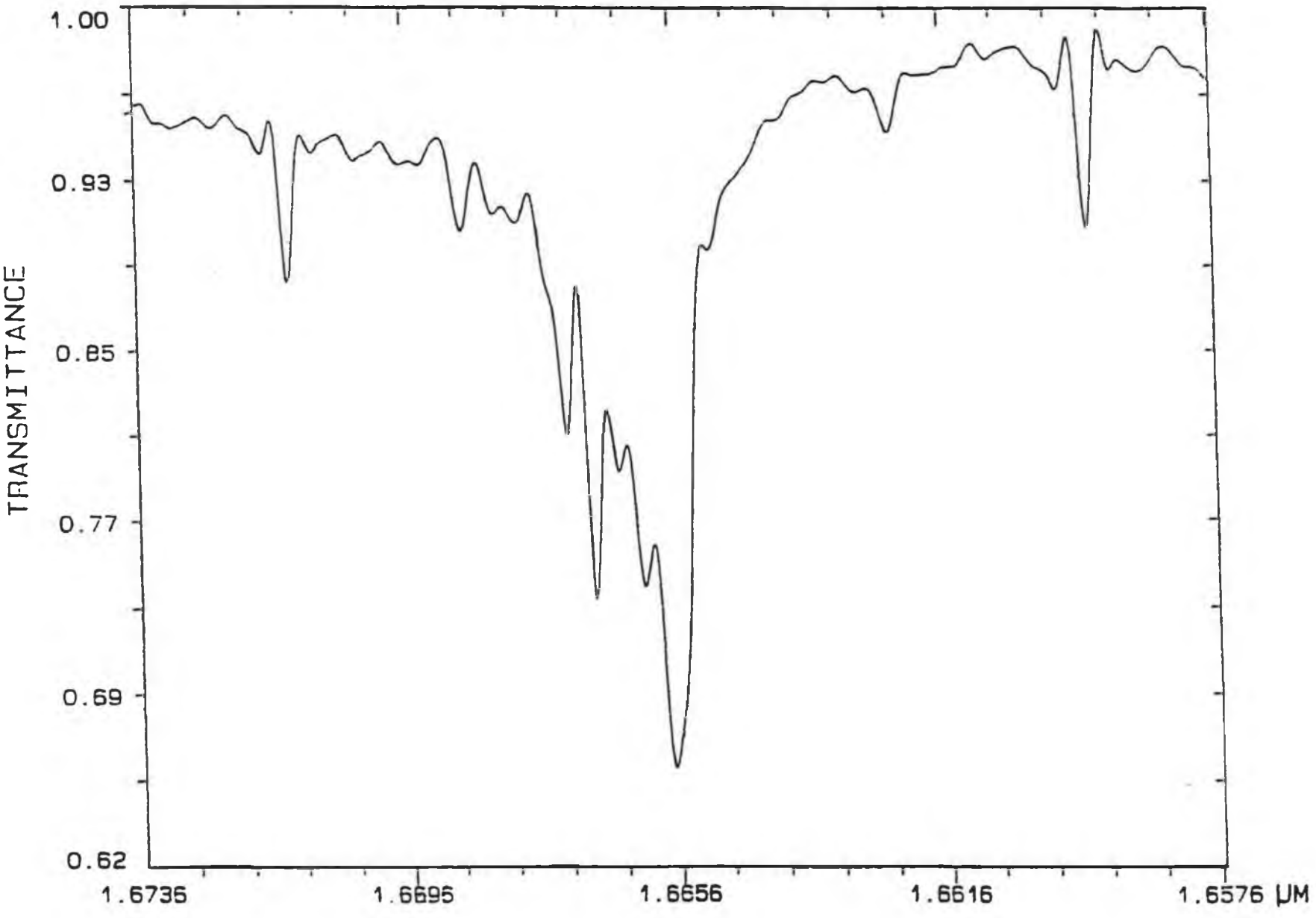

Fig 4.12 Spectrum of $2\nu_3$ Overtone of Methane (Resolution = 0.1cm^{-1})

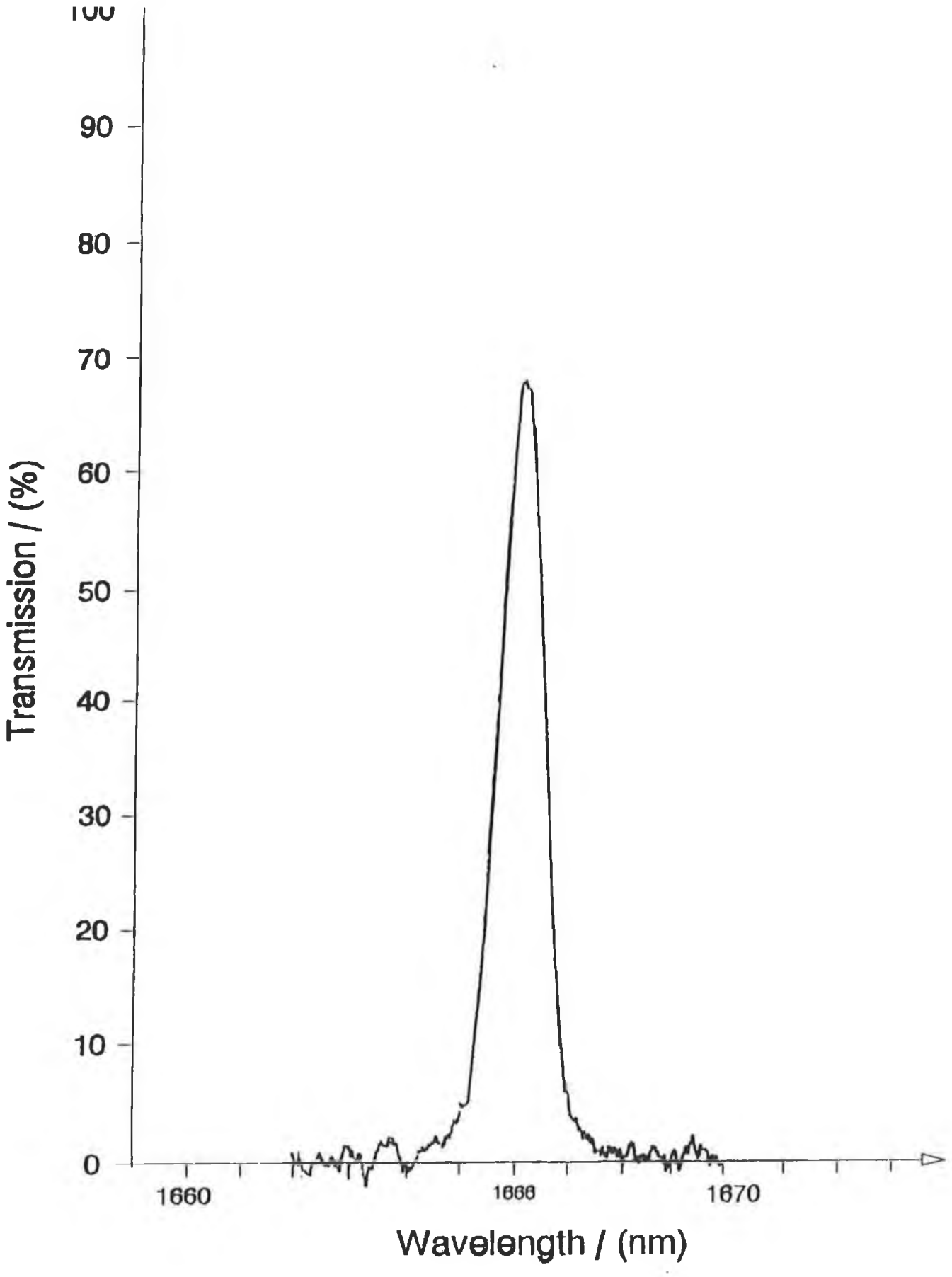

Fig 4.13 1666nm Interference Filter Tranmission

absorbing light in the 1664nm region. Both of these effects severely limit the system sensitivity.

After further examination of the spectrum, a filter with a peak transmission of 67% at 1666nm and a bandwidth of 2nm, was purchased. This filter, whose transmission characteristic is shown in Fig 4.13, transmits at the central region of the Q-branch. It therefore transmits more light at absorbing wavelengths and much less light at non-absorbing wavelengths than does the 1665nm filter, thereby enhancing the sensitivity greatly.

Although the signal transmitted by the 1666nm filter in the absence of methane in the gas cell is slightly less than that transmitted by the 1665nm filter, a reduction of 26% in this signal was observed when 5% methane was introduced to the gas cell. This is in contrast to the 4% reduction observed when using the 1665nm filter and indicates a 6.6 times increase in system sensitivity.

4.3.2 Optimization of Retroreflected Power Coupling

To optimize the system signal to noise ratio and therefore other important system parameters such as limit of detection, resolution etc., it was necessary to optimize the total power reaching the detector. Consequently, the retroreflected power coupled into port 3 (see Fig 4.15) of the fibre optic coupler had to be maximised. The 60mm focal length lens was replaced with a high quality Nikon microscope objective lens of numerical aperture 0.25 which increased the coupled percentage of power from 13% to 17% of the incident light into the gas cell.

4.3.3 Thermoelectric Cooling of LED

It was necessary to control the temperature of the LED to ensure a stable power coupling to the single mode fibre pigtail. A chart of the device temperature and corresponding device thermistor resistance was supplied with the device. A thermoelectric cooling circuit with feedback control was designed and constructed to stabilize the LED temperature. The circuit is shown in Fig 4.14.

R_t is set to 47kΩ which equals the resistance of the LED thermistor at a device temperature of 15°C. The resistor bridge is out of balance when the LED temperature is greater than 15°C (i.e. when the thermistor resistance is less than

47kΩ). As a result of this, the output at A is greater than zero and the thermoelectric cooler draws current thereby cooling the device. The feedback control line ensures that the circuit has a fast response to temperature change. An equilibrium thermoelectric current is reached when the circuit stabilises. For a room temperature of 22°C and a device temperature of 15°C, this current is approximately 0.5A.

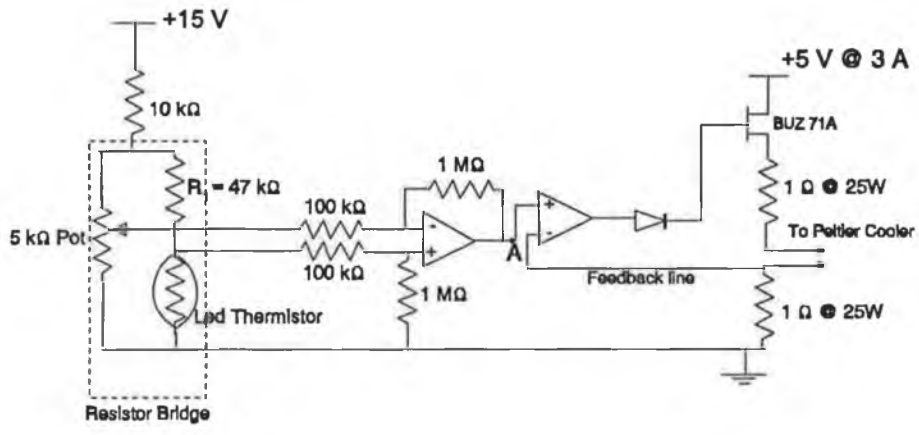

Fig 4.14 LED Thermoelectric Cooling Circuit

4.4 Conclusion

A detailed spectral characterization of two multimode fibre variants of the LD3207 LED source revealed modal noise and Fabry-Perot interference type effects when multimode fibre was connected to the devices. Consequently, a pigtailed single mode variant of the LED was purchased. This resulted in a severe reduction in system power (50μW at a driving current of 100mA).

Experimental work with the 1665nm "on" resonance filter revealed poor system sensitivity at gas concentrations below 5%. A new filter with a peak transmission of 67% at 1666nm and a bandwidth of 2nm was purchased. Experimental work with this filter showed a factor of 6.6 improvement in system sensitivity.

The coupled retroreflected power into port 3 of the coupler was increased to 17% of the incident light into the gas cell. This was achieved with a microscope objective of numerical aperture 0.25.

A thermoelectric cooling circuit with feedback control was constructed for the LED to stabilise the power coupled into the single mode fibre pigtail.

A diagram of the final experimental system is shown in Fig 4.15.

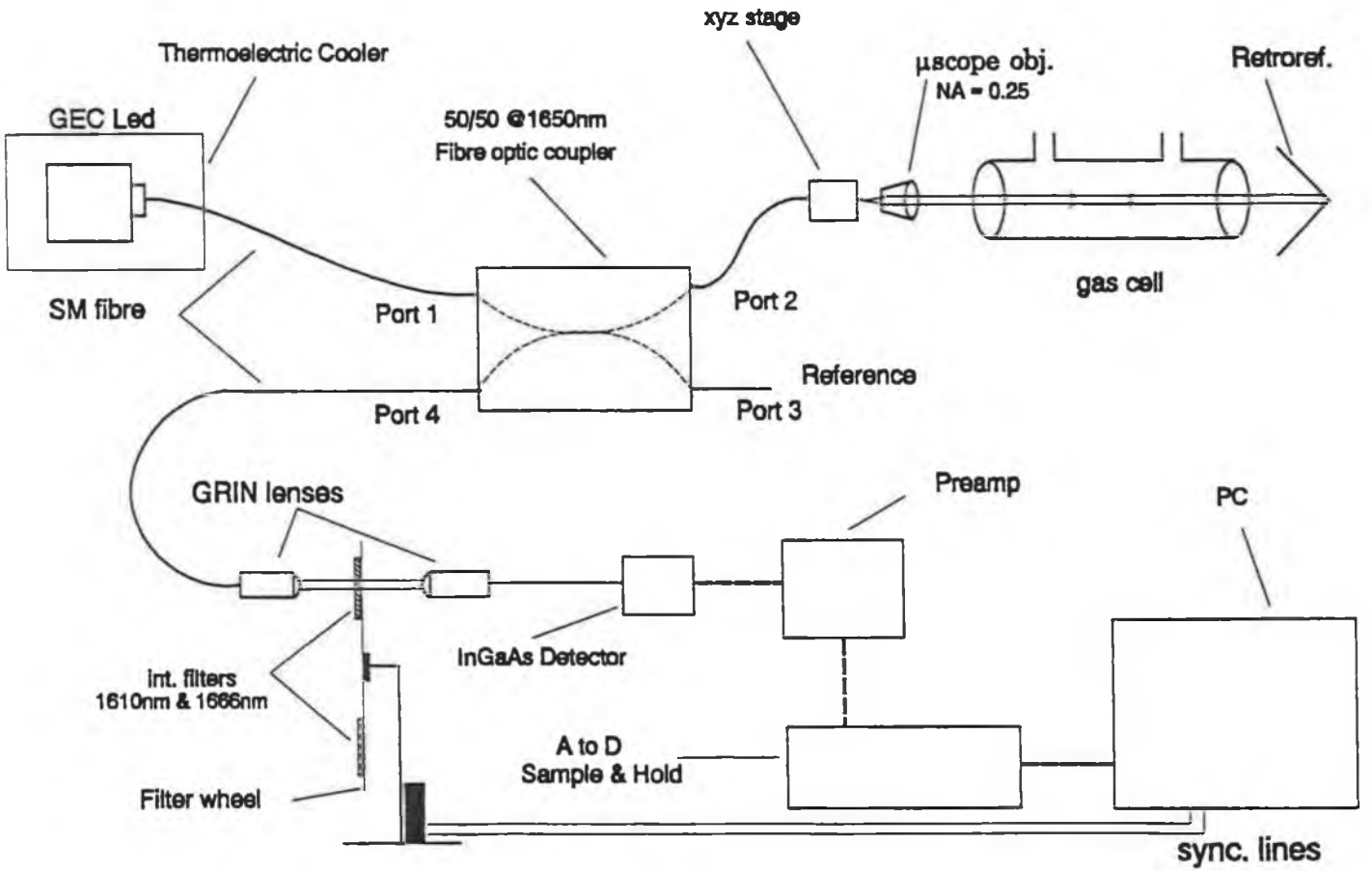

Fig 4.15 Dedicated Experimental System

Chapter 5

System Performance and Analysis

5.1 Introduction

The fibre optic methane gas sensing system described in chapters 3 and 4 was constructed and its performance evaluated. This chapter outlines the experimental method used to obtain a calibration curve for the sensor. The system performance is then characterised in terms of its range, sensitivity, repeatability, limit of detection, resolution, reproducibility and response time. The temperature dependence of the sensor is addressed and the overall system performance is reviewed.

5.2 Experimental Procedure

The determination of an unknown concentration of methane gas by this sensor is achieved using a calibration curve. The curve is generated by plotting the value of the absorption related function $\ln\left(\frac{I_{0\,\lambda on}}{I_{0\,\lambda off}} \cdot \frac{I_{\lambda off}}{I_{\lambda on}}\right)$ against known gas concentrations c, as described in section 3.2. The plot is taken for a fixed set of system parameters which include the LED driving current, LED temperature and ambient temperature.

A URS-100 mass flow controller (MFC) blending system, manufactured by Unit Instruments Ltd., Dublin, is used to produce concentrations from 0% to 5% by volume methane in nitrogen. The smallest concentration change possible with this system, keeping the total gas flow constant at 1 litre per minute, is 0.5% methane.

The programme Sense1 (see Fig 3.18) initially acquires and processes 200 values for the "on" and "off" absorption wavelengths for a zero concentration of methane in nitrogen, thereby yielding a mean $I_{0\,\lambda on}/I_{0\,\lambda off}$ value. This value, which is a constant, is used in the determination of $\ln\left(\frac{I_{0\,\lambda on}}{I_{0\,\lambda off}} \cdot \frac{I_{\lambda off}}{I_{\lambda on}}\right)$ for all methane gas concentrations from 0% to 5%. $I_{\lambda off}/I_{\lambda on}$ is calculated in each case by again acquiring and processing 200 "on" and "off" absorption values.

The software programme also calculates the standard errors on the absorption related function for each concentration as described in section 3.4.5.

The system calibration curve for an LED drive current of 100mA, an LED

ln ($I_{0\lambda on}.I_{\lambda off}$ / $I_{0\lambda off}.I_{\lambda on}$) / (ARU)
0.3
0.25
0.2
0.15
0.1
0.05
0
0
1

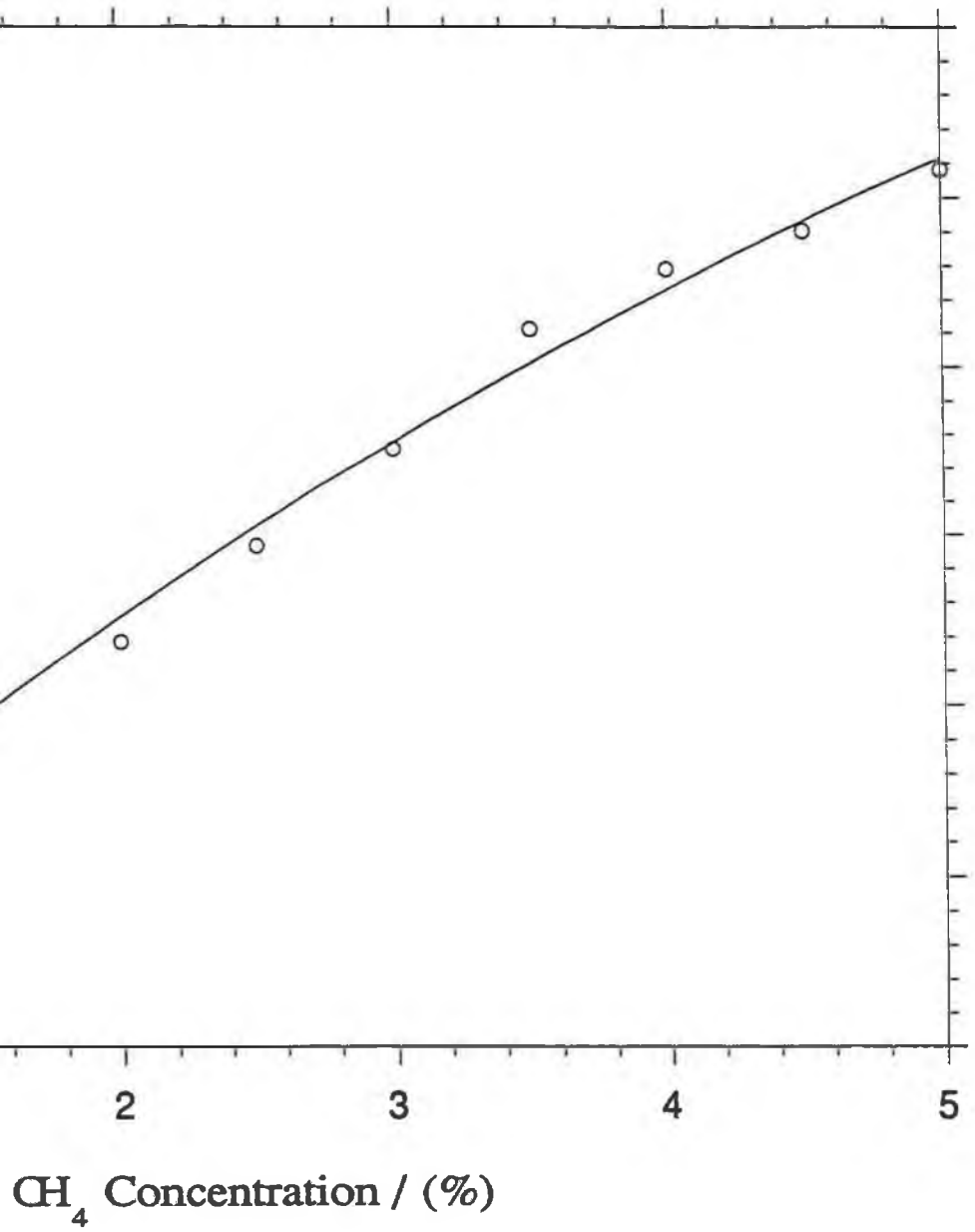

Fig 5.1 System Calibration Curve

temperature of 15°C and a fixed room temperature of 21°C is shown in Fig 5.1. The x axis is in units of concentration percentage, while the y axis is in units now termed "absorption related units" or ARU. The error bars are small and fall well within each data point circle shown on the plot. The temperature of the interference filters is assumed to be the same as ambient temperature and the temperature stability of the filters' transmission characteristics is a critical factor with respect to the system repeatability as will be shown in section 5.4. The calibration curve data and associated standard errors are shown in Table 5.1.

CH_4 concentration (%)	$\ln (I_{0\,\lambda on} \cdot I_{\lambda off} / I_{0\,\lambda off} \cdot I_{\lambda on})$ (ARU)	Standard Error (ARU)
0	0	.00054
0.5	0.04138	.00057
1.0	0.07341	.00057
1.5	0.09537	.00057
2.0	0.11894	.00075
2.5	0.14692	.00067
3.0	0.17595	.00063
3.5	0.21148	.00061
4.0	0.22938	.00063
4.5	0.24045	.00064
5.0	0.25836	.00067

Table 5.1 Calibration Curve Data

A second order polynomial curve fit to the data was performed using the Kaleidagraph graph plotting package for the Apple Macintosh II. The curve fit coefficients are as follows

$$Y = M_0+M_1x+M_2x^2$$

$$M_0 = 0.003$$

$$M_1 = 0.068$$

$$M_2 = -0.0033$$

and the correlation coefficient is 0.997.

The calibration curve is non linear and so the Beer-Lambert law does not hold entirely. This is most probably due to the fact that the Beer-Lambert law holds only for monochromatic radiation. The Q-branch absorption region at 1.666μm consists of many partially overlapping absorption lines which individually contribute to the overall absorption at the Q-branch. The spectral bandwidth of the "on" absorption interference filter (1666nm) is 2nm and is therefore much greater than that of any of these absorption lines. Consequently, the filter transmits some light that is not absorbed but is detected and so forms part of the $I_{\lambda on}$ value in the absorption related function. As a result of this the value of the function does not change linearly with increasing CH_4 concentration.

Fig 5.2 shows a near real time measurement of the methane concentration in the gas cell for an LED driving current of 100mA at 15°C with a room temperature of 22.5°C. To obtain this, the program Sense 1 was altered to store 1000 data points. Each data point was determined by firstly collecting 20 values for the "on" and "off" absorption signals and then calculating an average $I_{\lambda off}/I_{\lambda on}$ together with the initial $I_{0\,\lambda on}/I_{0\,\lambda off}$ for 100% nitrogen as before. The graph depicts the non linear response observed in the calibration curve of Fig 5.1. It is also evident that there is an inherent hysteresis between the incremental and decremental changes in concentration. The source of this hysteresis has not been identified with certainty but it may be due to "backlash" hysteresis in the two manually operated dials of the mass flow controller system. However, all calibration curves presented in this work are based on data taken by incrementing the methane concentration.

The calibration curve (Fig 5.1) gives a much more accurate representation of data than that of the real time measurement, as averaging occurs over 200 values for each concentration as opposed to only 20 values for the real time plot (Fig 5.2).

5.3 Sensor Characterisation

Range : The range of the sensor is defined as that range of measurand values (i.e. concentration of methane gas) over which the sensor gives an unambiguous output signal. The sensor can detect unambiguously concentrations up to 100% of methane in nitrogen. However, the upper gas concentration detection requirement of

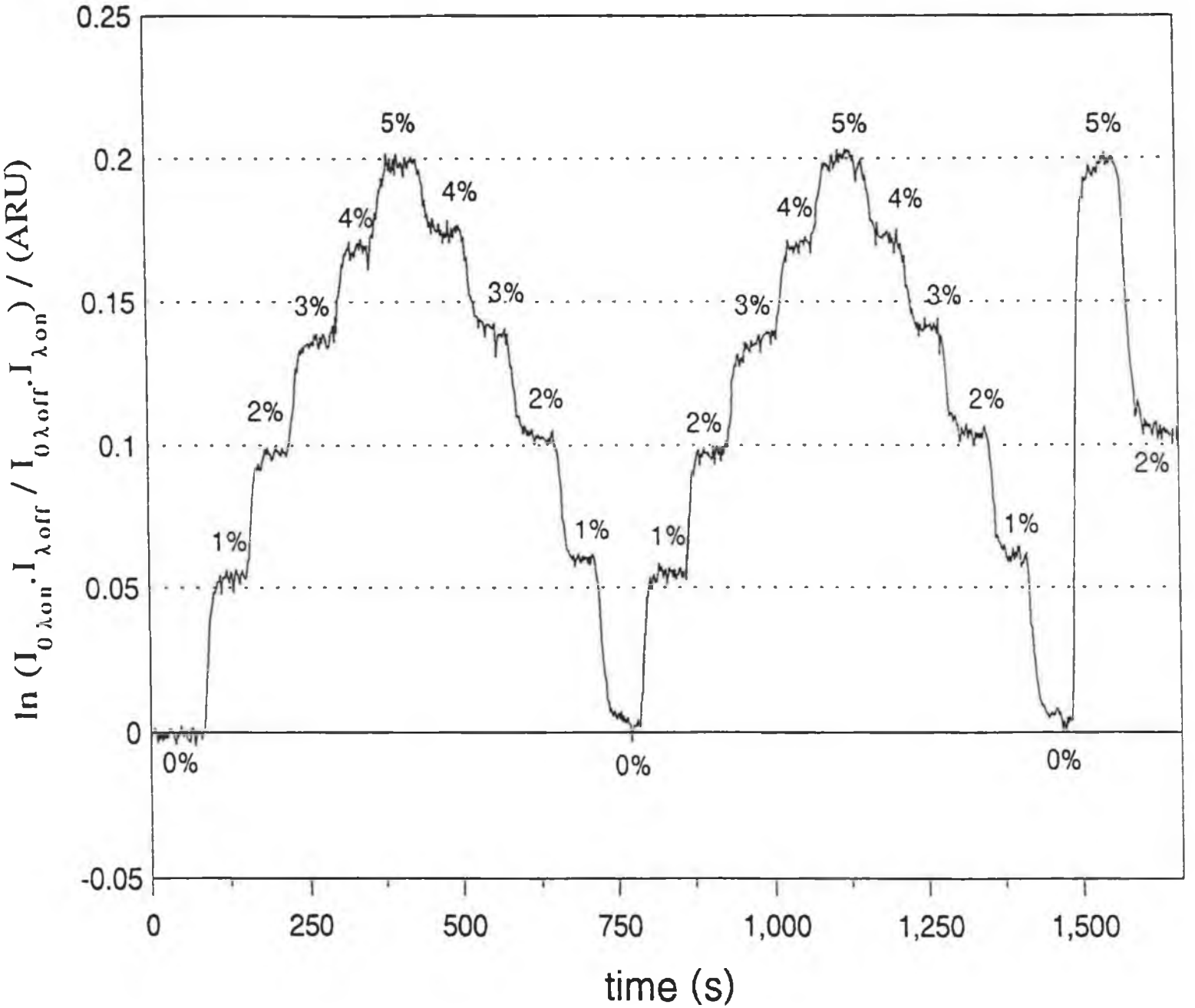

Fig 5.2 Near Real-Time Measurement of Methane

this sensor is 5% methane in nitrogen. From the calibration curve in Fig 5.1 it can be seen that the sensor output signal is unambiguous for all concentrations up to 5% and so the range is from 0% to 5% CH_4 in N_2.

Sensitivity : The sensor sensitivity is a measure of the incremental change in signal output for a given change in the measurand. For a system with a linear response, the sensitivity is equal to the slope of the plot. The primary objective of this sensor is to accurately detect 25% of the lower explosion limit (LEL) of methane in nitrogen (i.e. 1.25% by volume). The sensor exhibits a near linear response in the 0.5% to 2% CH_4 concentration region which includes the 25% LEL point. The sensitivity over this region is approximately 0.06 ARU/%. The sensitivity decreases to approximately 0.018 ARU/% in the 5% region.

Resolution : The resolution is defined as the ability of a sensor to distinguish between closely adjacent values of the measurand. It can be calculated as 2 standard errors from the indicated value. Taking the worst case standard error in the 0.5% to 2% near linear region to be 0.00075 ARU, and the sensor sensitivity to be 0.06 ARU/%, then the resolution is 0.025%.

Limit of Detection : The limit of detection is defined as the gas concentration which gives a signal equal to the zero concentration signal plus three standard errors of the zero concentration. From Fig 5.1 and Table 5.1, the zero concentration reading (i.e. the y axis intercept M_0) is 0.003 ARU and the standard error is 0.00054 ARU. Assuming a sensitivity of 0.06 ARU/% at the lower concentration range, then the value for the limit of detection is 0.077%.

Repeatability : Repeatability is a measure of the agreement between a number of consecutive readings of a chosen value of the measurand. Therefore, the standard error calculated on the 200 readings taken for each concentration measurement is a measure of the repeatability error. The confidence interval is a range within which one may reasonably assume that the true value of a quantity being measured will be found. The 95% confidence interval is given by

$$\mu = \bar{x} \pm t(s.e.)$$

where μ is the true value, $\bar{x}$ is the average value, and t is a constant obtained from statistical tables and is equal to 1.96 for a 95% confidence interval. Using the

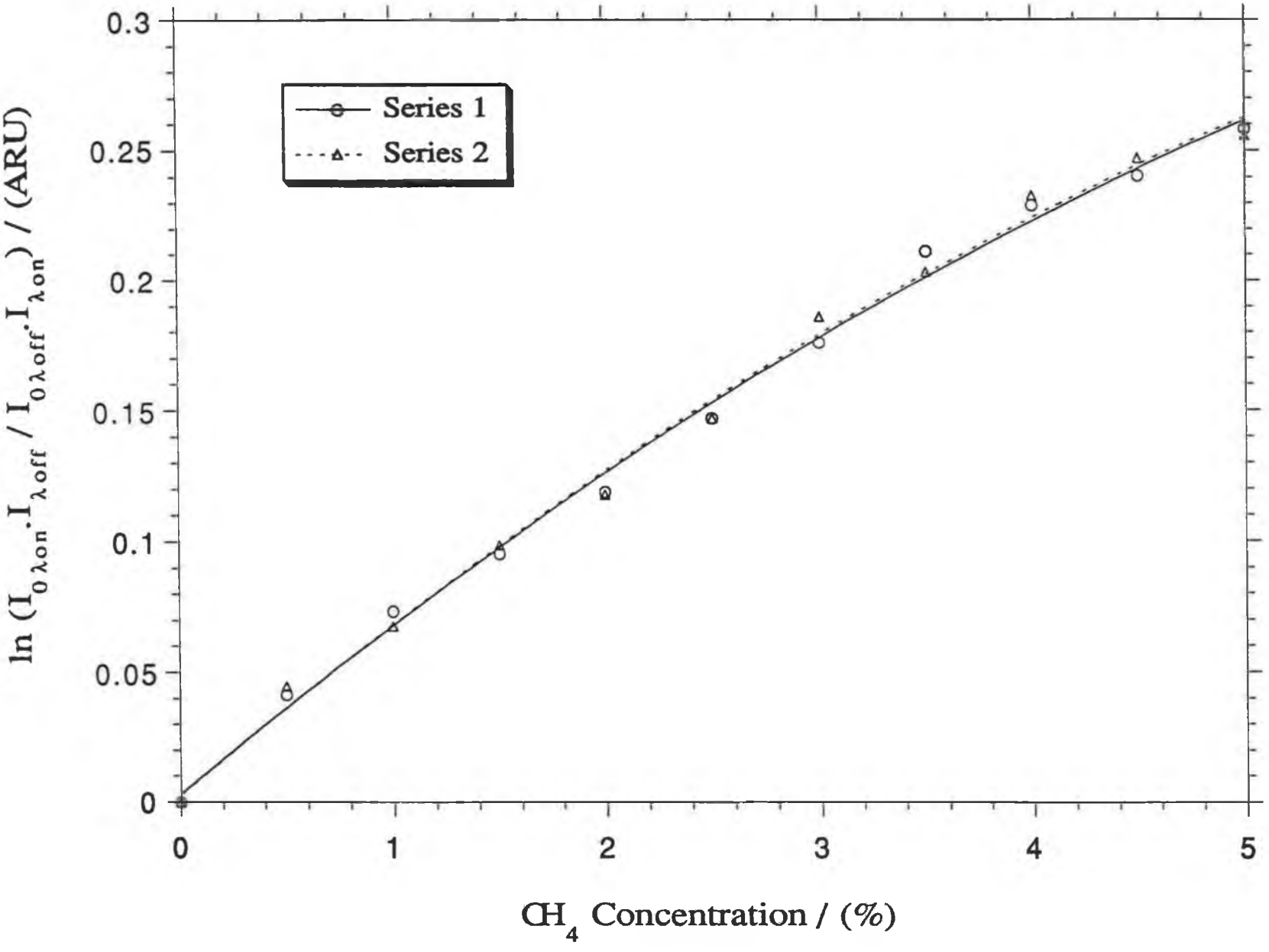

Fig 5.3 System Calibration Curves

standard error values for each concentration measurement shown in Table 5.1 and multiplying each of these values by 1.96, it can be seen that the random uncertainty varies from ±2.69% of the average signal at 0.5% methane concentration, to ±0.5% of the average signal at 5% methane concentration.

Reproducibility : Reproducibility is a measure of the agreement between measurements of a particular value of the measurand which are taken on different occasions. The set of data shown in Table 5.2 were taken with the experimental conditions unchanged from those of the data in Table 5.1.

Fig 5.3 shows a plot of this data (Series 2) overlaid on the plot from Fig 5.1 (Series 1). The second order polynomial curve fit coefficients to the data are

Concentration (%)	$\ln (I_{0\,\lambda on}.I_{\lambda off} / I_{0\,\lambda off}.I_{\lambda on})$ (ARU)	Standard Error (ARU)
0	0	0.00054
0.5	0.04454	0.00057
1.0	0.06763	0.00057
1.5	0.09850	0.00056
2.0	0.11775	0.00058
2.5	0.14686	0.00058
3.0	0.18590	0.00059
3.5	0.20348	0.00060
4.0	0.23296	0.00073
4.5	0.24706	0.00064
5.0	0.25589	0.00065

Table 5.2 Calibration Curve Data (Series 2)

$$Y = M_0+M_1x+M_2x^2$$

Series 1	Series 2
$M_0 = 0.003$	$M_0 = 0.0026$
$M_1 = 0.068$	$M_1 = 0.069$
$M_2 = -0.0033$	$M_2 = -0.0034$

and the correlation coefficient is 0.997 in each case.

As can be seen from Fig 5.3 the calibration curves overlap exactly at the lower concentration values while there is a slight displacement between both curves at higher concentrations. Therefore the system reproducibility is good for a specific set of parameters, namely room temperature, LED temperature and drive current.

Response Time : The response time can be defined as the time interval from the instant a step change occurs in the measurand to the instant when the change in the indicated value passes and remains above 90% of the eventual steady state value. The response time of this sensor is dependent both on the rotation speed of the filter wheel, as this limits the speed of the data collection, and the user specified number of averages for each concentration measurement. For a specified 200 averages, 800 values (i.e. 200 values for each filter and each background reading) must be collected as explained in section 3.4.5. This takes approximately 10 seconds. The processing of this data takes approximately another 2 seconds. If a step change in the measurand occurs while one set of 800 values is being collected then the new signal is evaluated with the next set of values. Therefore the worst-case response time of the sensor is 24 seconds for a collection speed of 80 signals per second.

5.4 Temperature Dependence

As mentioned in section 5.3, the reproducibility of the sensor is good, but is strictly dependent on the system parameters remaining unchanged. These parameters principally include the LED temperature and drive current, both of which ensure a stable power coupling between the LED and the pigtailed single mode fibre.

However, the most important parameter is the ambient temperature which governs the temperature of the interference filters. Because the bandwidths of the interference filters are so narrow, 5nm for the 1610nm filter and 2nm for the 1666nm filter, the peak spectral transmission of each is greatly influenced by small

temperature variations. The peak transmission shifts to longer wavelengths with increased temperature. This factor is important even in the absence of any absorbing gas in the cell as shown in Fig 5.4. Here, a flow of 100% nitrogen through the gas cell was maintained. The altered Sense 1 programme, as described in section 5.1 for near real time measurement, was used to chart the variation in ARU values over a range of room temperatures. The temperature was measured on a digital thermometer accurate to 0.1°C. As can be seen in Fig 5.4, the initial room temperature is 20.1°C. This decreases to 20°C and then rises to 20.5°C before dropping again to 20.1°C. The variation in signal over the 0.4°C temperature change is significant when compared to the ARU values in Fig 5.3. Assuming that the thermoelectric cooling unit maintains the LED at a fixed temperature and that no other optical or electronic system parameters (e.g. refractive index changes in the fibres) can change significantly with slight temperature variations, it is reasonable to assume that even small variations in the interference filter temperature adversely affect the ARU measurement when methane gas concentrations are introduced. This leads to both inaccurate calibration curves and incorrect determination of unknown samples. This strong dependence upon ambient temperature stability is the paramount problem with this system. It can be investigated in more detail as outlined in chapter 6.

5.5 Conclusion

A characterisation of the system performance of the fibre optic gas sensor described in chapters 3 and 4 was undertaken. The calibration curve obtained for the sensor is non linear. This deviation from the Beer-Lambert law can be accounted for by the fact that the bandwidth of the "on" resonance filter at 1666nm is greater than that of any of the individual absorption lines in the Q-branch of the $2\nu_3$ overtone band of methane.

The sensor has a sensitivity of 0.06 ARU/% in the 0.5% to 2% CH_4 concentration region, a resolution of 0.025% CH_4 and a limit of detection of 0.077% CH_4. The systems repeatability is good with a largest random error of ±2.69% of the average signal at 0.5% CH_4 concentration. The reproducibility of the system is also good.

The system operation is critically dependent on the stability of the temperature of the interference filters.

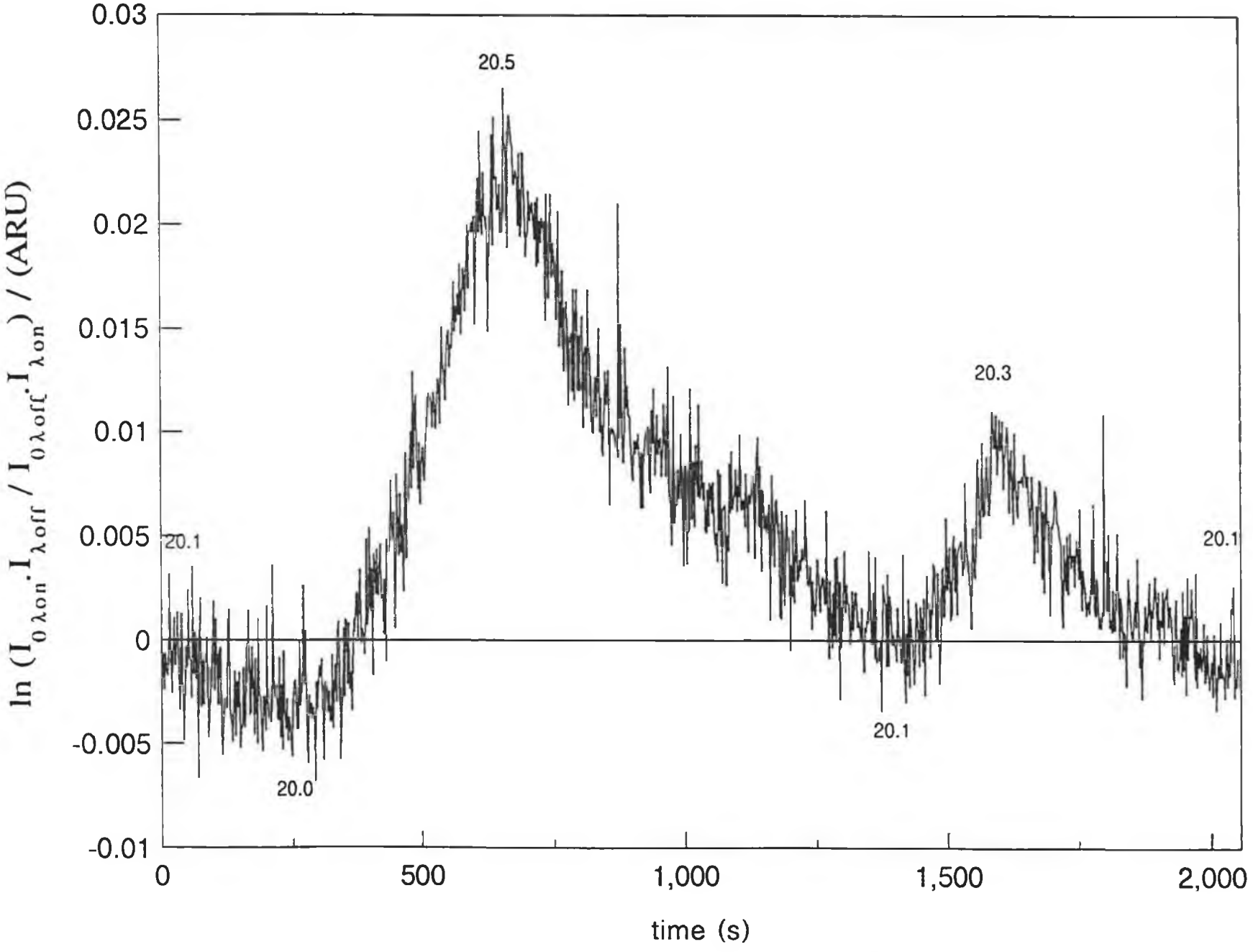

Fig 5.4 System Dependence on Temperature

Chapter 6
Conclusions / Future Developments

A fibre optic remote methane sensing system, addressing both the cost and performance criteria required of sensors by industry, was designed and constructed. The system is based on the absorption of infra red light by methane in the 1.66μm spectral region and employs a novel LED source designed specifically for methane sensing, together with ruggedised standard telecommunication components. Initially, the system was designed for multimode fibre but the LED source proved to be unsuitable due to modal noise effects in multimode fibre. Consequently, the system design was reconfigured to employ an LED source pigtailed to single mode fibre. At a drive current of 100mA, this LED couples approximately 50μW of power in the 1.66μm spectral region into single mode fibre. This is greater than that achieved by any other similar devices commercially available.

The other most important system components were the optical interference filters, specifically the "on" absorption filter as it is important in determining the system sensitivity. Initially, a filter with a peak transmission at 1665nm (i.e. the Q-branch absorption peak of the $2\nu_3$ overtone of methane) was employed, but poor system sensitivity was achieved. After analysing spectra taken with a high resolution fourier transform infra red spectrometer, a filter with a peak transmission of 1666nm and a bandwidth of 2nm was purchased. This improved system sensitivity by a factor of six. A thermoelectric cooling circuit for the LED was also designed and implemented to ensure temperature stability and therefore power stability.

The sensor has a resolution of 0.025% CH_4 with a limit of detection of 0.077% CH_4. This value is 18 times smaller than the required system value of 1.25% CH_4 (i.e. 25% Lower Explosive Limit) as defined by industry. The system has good repeatability having a largest random error of ±2.69% at a concentration of 0.5% CH_4.

The system suffers from two significant disadvantages. These are the temperature dependence of the optical interference filters and the use of moving parts, specifically the rotating filter wheel. Because the "on" absorption filter transmission is so narrow, any variation in ambient temperature by more than 0.1°C

is going to affect its transmission significantly and as a result affect the system performance. Therefore, the high sensitivity achieved with the system because of the narrow bandwidth of the filter is countered by the filter temperature dependence. The possibility of acquiring a similar filter which is less temperature dependent was investigated. TecOptics Ltd., Onchan, Isle of Man, manufacture such filters and were contacted. However, the quoted cost of these filters was much too great (~ £2000). Another alternative is that the filters could be temperature controlled if isolated in a controlled environment.

The second problem of moving parts in the system is important as industry prefers not to have such design features in sensing systems. One alternative is to use a Y shaped coupler with the optical filters attached to the fibre ends and then employ a two detector sensing scheme. The principal problem with this is the difficulty in achieving and maintaining perfectly matched detectors.

Finally, a possible development of this system is the multiplexing of a number of remote gas cells to a single detection system using directional couplers. This approach would lend itself to multipoint measuring in mines and landfill-sites.

References

1. MacCraith, B.D., Ruddy, V., Potter, C., McGilp J.F., and O'Kelly, B., "Electronics Letters", Vol. 27, pp 1247-1248, (1991).
2. Baldini, F., "Proceedings SPIE", Vol. 1368, pp 184-190, (1991).
3. Chan, K., Ito, H., and Inaba, H., "Applied Physics Letters", Vol 43, pp634-636, (1983).
4. O'Keeffe, G., MacCraith, B.D., McDonagh, C., O'Kelly, B., and McGilp, J.F., "Sensors VI: Technology Systems and Applications", pp 75-78, IOP Publishing Ltd., (1993).
5. Alarie, J.P., Sepaniak, M.J., and Vo-Dinh, T., "Analytica Chimica Acta", Vol. 229, p169, (1990).
6. Freeman, J.E., Childers, G.A., Steele, A.W., and Hieftje, G.M., "Analytica Chimica Acta", Vol. 177, p121, (1985).
7. McCabe, S., and MacCraith, B.D., "Electronics Letters", Vol. 29, pp 1719-1720, (1993).
8. Shariari, M.R., Zhou, Q., and Sigel, G.H., "Optics Letters", Vol. 13, No.5, pp 407-409, (1988).
9. Stuart, A.D., and Samson, P.J., "Proceedings 13th Australian Conference on Optical Fibre Technology", p117, (1988).
10. European Standard, EN 50055, "Electrical Apparatus for the Detection and Measurement of Combustible Gases", (1991).
11. Muhammad, F.A., and Stewart, G., "Electronics Letters", Vol. 28, pp 1205-1206, (1993).
12. Alarcon, M.C., Ito, H., and Inaba, H., "Applied Physics B", Vol. 43, pp 79-83, (1987).
13. Chan, K., Ito, H., and Inaba, H., "Journal of Lightwave Technology", Vol Lt-5, pp 1706-1711, (1987).
14. Mohabati, A., and King, T.A., "Proceedings SPIE", Vol. 1011, (Fibre Optic Sensors III), pp 183-189, (1988).
15. Zientkiewicz, J.K., "Proceedings SPIE", Vol 992, (Fibre Optic Reliability: Benign and Adverse Environments II), pp 182-187, (1988).
16. Hordvik, A., Berg, A., and Thingbø, D., "Proceedings 9th European Conference

on Optical Communication", pp 317-320, (1983).

17. Chan, K., Ito, H., and Inaba, H., "Applied Optics", Vol. 23, pp 3415-3420, (1984).
18. Stueflotten, S., Christensen, T., Iversen, S., Hellvik, J.O., Almas, K., Wien, T., and Graav, A., "Proceedings SPIE", Vol. 514, pp 87-90, (1984).
19. Zientkiewicz, J.K., "Proceedings SPIE", Vol. 1085, (Optical Fibres and Their Applications V), pp 495-496, (1989).
20. Dubaniewicz, T.H., and Chilton, J.E., "Report on Investigations 9407", United States Dept. of the Interior, Bureau of Mines, (1991).
21. Dakin, J.P., Croydon, W.F., and Hedges, N.K., "Proceedings SPIE", Vol. 949, (Fibre Optics '88), p200, (1988).
22. Dakin, J.P., and Edwards, H.E., "Optical Engineering", Vol. 31, pp 1616-1620, (1992).
23. Goody, R., "Journal of the Optical Society of America", Vol. 58, p900, (1968).
24. Samson, P.J., and Stuart, A.D., "Proceedings 13th Australian Conference on Optical Fibre Technology", pp 113-116, (1988).
25. Willett, M., British Coal, U.K., Private Communication.
26. Norris, J.O.W., "Analyst", Vol. 114, p1365, (1989).
27. Wolfbeis, O.S., Boisde, G.E., and Gauglitz, G., in "Sensors, A Comprehensive Survey", Vol.2, Part 1, Chapter 12, eds. Gopel, W., Hesse, J., and Zemel, J.N., VCH, (1991).
28. Bransden, B.H., Joachain, C.J., "Physics of Atoms and Molecules", Longman, (1983).
29. Wheatley, P.J., "The Determination of Molecular Structure", Dover Publications, (1981).
30. Crossley, S.D., and Norris, J.O.W., "OSCA: Review of Principles and Devices for Absorption-Based Optical Gas Sensing", OSCA Contract 95, (1992).
31. Brand, J.C.D., Speakman, J.C., Tyler, J.K., "Molecular Structure: The Physical Approach", Second Edition, Edward Arnold, (1975).
32. Richards, W.G., Scott, P.R., "Structure and Spectra of Molecules", Wiley, (1985).
33. Steinfeld, J.I., "Molecules and Radiation: An Introduction to Modern Molecular

Spectroscopy", MIT Press, (1978).

34. Beiser, A., "Perspectives of Modern Physics", McGraw-Hill, (1969).
35. Commercial Information, GEC Marconi, Caswell, U.K. (1992).
36. Neumann, E.G., "Single-Mode Optics: Fundamentals", Springer, (1988).
37. Ungar, S., "Fibre Optics: Theory and Applications", Wiley, (1990).
38. Baker, D.G., "Monomode Fibre-Optic Design", Van Nostrand Reinhold Company, (1987).
39. Hecht, E., "Optics", 2nd Edition, Addison Wesley, (1987).
40. MacLeod, H.A., "Thin Film Optical Filters", 2nd Edition, Hilger, (1985).
41. Ross, D.A., "Optoelectronic Devices and Optical Imaging Techniques", MacMillan, (1979).
42. Kingston, R.H., "Detection of Optical and Infrared Radiation", Springer-Verlag, (1978).
43. Van Etten, W., and Van Der Plaats, J., "Fundamentals of Optical Fiber Communications", Prentice Hall, (1991).
44. Burgess, J., "Laser Focus World", p15, October, (1991).